8-2016

Ultracold quantum scattering in the presence of synthetic spin-orbit coupling

Su-Ju Wang
Purdue University

Recommended Citation

Wang, Su-Ju, "Ultracold quantum scattering in the presence of synthetic spin-orbit coupling" (2016). *Open Access Dissertations*. 886.
https://docs.lib.purdue.edu/open_access_dissertations/886

Graduate School Form
30 Updated 12/26/2015

PURDUE UNIVERSITY
GRADUATE SCHOOL
Thesis/Dissertation Acceptance

This is to certify that the thesis/dissertation prepared

By Su-Ju Wang

Entitled
ULTRACOLD QUANTUM SCATTERING IN THE PRESENCE OF SYNTHETIC SPIN-ORBIT COUPLING

For the degree of Doctor of Philosophy

Is approved by the final examining committee:

Chris H. Greene Chair	
Yong P. Chen	
Francis Robicheaux	
Erica Carlson	

To the best of my knowledge and as understood by the student in the Thesis/Dissertation Agreement, Publication Delay, and Certification Disclaimer (Graduate School Form 32), this thesis/dissertation adheres to the provisions of Purdue University's "Policy of Integrity in Research" and the use of copyright material.

Approved by Major Professor(s): Chris H. Greene

Approved by: John P. Finley July 18, 2017

Head of the Departmental Graduate Program Date

ULTRACOLD QUANTUM SCATTERING IN THE PRESENCE OF SYNTHETIC SPIN-ORBIT COUPLING

A Dissertation

Submitted to the Faculty

of

Purdue University

by

Su-Ju Wang

In Partial Fulfillment of the

Requirements for the Degree

of

Doctor of Philosophy

August 2016

Purdue University

West Lafayette, Indiana

To my family

ACKNOWLEDGMENTS

First of all, I would like to thank my thesis advisor, Dr. Chris H. Greene, for his continuous support and guidance over the course of my Ph.D. studies. His broad knowledge in the field of the atomic, molecular and optical (AMO) physics has allowed me to build a solid foundation for my research. He has given me the opportunity to explore a variety of new topics in AMO physics. I express my deep gratitude for his help in overcoming many significant challenges during my research and while finishing my thesis.

Besides my advisor, I want to give my sincere gratitude to my thesis committee members, Dr. Yong P. Chen, Dr. Francis Robicheaux, and Dr. Erica Carlson. I have been very fortunate to have the chance to collaborate with Prof. Chen's experimental team at Purdue. I have always learned to grasp clear physical pictures with Prof. Chen's good intuition in physics. As a member of the large theoretical AMO physics group at Purdue, I have attended the bi-weekly lunch meetings with Prof. Robicheaux, whose in-detail explanations of a variety of physical problems have taught me a lot. I also took the 590 course with Prof. Carlson in the early stage of my Ph.D. studies. Her passionate way of illustrating physics has always been a guide for me.

My sincere gratitude also goes to Dr. Gabriele F. Giuliani. I was very fortunate to work with him for a year. His enthusiasm for physics and life has always been and continues to be inspiring to me.

I also want to thank the postdoctoral scholars and visiting scholars in Prof. Greene's group and Prof. Robicheaux's group: Dr. Panagiotis Giannakeas, Dr. Jesús Pérez-Ríos, Dr. Rachel Wooten, Dr. Kevin Daily, Dr. Baochun Yang, and Dr. Hua-Chieh Shao. They have always provided me insightful assistances to my research topics and cheerful discussions outside of academia. I thank the visiting scholar, Dr. Huili Han, for her help in the three-body project.

I thank my colleagues and collaborators from the experimental side. Dr. Abraham Olson has been a great collaborator and an experimentalist. His critical and independent thinking have made my first project with him successful. The other members of Prof. Chen's team: Dr. Robert Niffenegger, Chuan-Hsun Li, and David Blasing, have also been very helpful to various research projects. Their diligence and dedication to every detail of their experiments have impressed me.

I thank my colleagues from the theoretical sides: Dr. Chen Zhang, Yijue Ding, Matt Eiles, Bin Yan, Changchun Zhong, Tyler Sutherland, and Xiao Wang. I have learned a lot from numerous discussions with them. They have made my graduate experience in the office more colorful.

I thank my family for supporting me spiritually throughout my graduate life. They have been very supportive and always encouraged me to pursue my dreams since I was a kid.

Finally, I want to thank Dr. Qi Feng for his personal support and time for endless discussions on various topics from a very different perspective. Also, I thank King Triton for his warm company while I was writing my thesis.

TABLE OF CONTENTS

LIST OF TABLES

LIST OF FIGURES

Figure Page

ABBREVIATIONS

SOC	spin-orbit coupling
RDSOC	Rashba-Dresselhaus spin-orbit coupling
BEC	Bose-Einstein condensate
DFG	degenerate Fermi gas
CIR	confinement-induced resonance
AMO	atomic, molecular, and optics
NIST	National Institute of Standards and Technology
TG	Tonks-Girardeau
s-TG	super Tonks-Girardeau
SM	single minimum
DM	double minimum
c.o.m.	center of mass
1D	one dimension
3D	three dimensions
LZ	Landau-Zener
ZB	Zitterbewegung
EIT	Electromagnetically induced transparency
STIRAP	Stimulated Raman adiabatic passage

ABSTRACT

Su-Ju Wang Ph.D., Purdue University, August 2016. Ultracold Quantum Scattering in the Presence of Synthetic Spin-Orbit Coupling. Major Professor: Chris H. Greene.

Two-body scattering constitutes one of the most fundamental processes in various physical systems ranging from ultracold dilute quantum gases to energetic quark-gluon plasmas. In this dissertation, we study the low-energy atomic collision physics in the presence of synthetic gauge fields, which are generated by atom-light interaction. One category of synthetic gauge fields is the artificial spin-orbit coupling. We discuss three different aspects in scattering theory: ultracold collision, scattering resonance, and bound state formation from a few-body perspective when the atomic spin states are coupled with their center-of-mass motion. The understanding of the spin-orbit effects on the modification of the scattering processes not only builds the foundation of collision physics in the presence of non-abelian gauge fields but also paves the way towards unraveling the few-body correlations in many-body systems.

1. INTRODUCTION

The purpose of the introductory chapter is to give the readers a basic understanding towards the two topics: (1) synthetic gauge fields in neutral atoms, and (2) quantum scattering theory, especially in the low-temperature limit. In Sec. 1.1, we explain different methods which physicists have managed to make a neutral atom to behave like in an external electromagnetic field with a focus on the realization of synthetic gauge fields via atom-light interactions. In Sec. 1.2, we discuss the fundamental aspects of collision theory. Important concepts in cold collisions, such as partial waves and scattering length, will be introduced. These two ideas are essential to understand the work in the dissertation. An outline at the end of the chapter is provided as a preview of the thesis.

1.1 Overview of synthetic gauge fields for neutral atoms

Since the first observation of Bose-Einstein condensates and degenerate Fermi gases [1][2][3], ultracold atomic systems have emerged as a new class of highly controllable systems that can serve as quantum simulators [4] of traditional condensed-matter systems. The flexibility of cold atomic systems is reflected in several aspects. First of all, the atomic gases can be bosonic, fermionic or mixtures of both. This extends our interests beyond the traditional solid state systems, which are always fermionic. Secondly, the environment of ultracold gases is variable and can be created by adding laser light to the system. Strong confinements create effective low-dimensional systems, where new phases could occur [5][6]. For another instance, one set (three sets) of two counter-propagating laser fields of same wavelengths are used to create 1D (3D) optical lattices to simulate crystalline systems. Thirdly, interatomic interactions are tunable by Feshbach resonances [7]. The inverse scattering length ($1/a_s$)

can be tuned from negative infinity to zero and then to positive infinity, causing the famous BCS-BEC crossover in degenerate Fermi gases [8]. Thanks to the tunability of interatomic interaction, it also allows us to study the strongly correlated systems with dilute quantum gases. The properties of unitary quantum gases have been a popular topic in recent years, where the only length scale that matters is the interparticle distance (or density) when the scattering length diverges.

Since an atom is charge neutral, its center of mass motion cannot be coupled to external electromagnetic fields. Therefore, the development of a way to create synthetic gauge fields in neutral cold-atom systems has become an important research direction. The capability of realizing synthetic gauge potentials in neutral atomic systems will open many new avenues to quantum simulations involving gauge fields, e.g. the quantum Hall effect and its families. Another important example would be topological insulators [9][10], which need a special kind of synthetic gauge potential: spin-orbit coupling. Being able to simulate these quantum systems not only allows us to study many fundamental and important questions in many-body physics from a different approach but also helps us to study questions that are inaccessible in solid state systems.

So far, there have been several ideas being proposed to realize synthetic gauge fields in cold gases. One way is through rotating atomic gases [11]. The Coriolis force in the rotating frame on the neutral atoms behaves exactly the same way as the Lorentz force on a charged particle in an external magnetic field. Assuming the rotation is along z axis, the effective magnetic field will point along the z axis with the strength proportional to the rotation frequency, Ω. Vortices generated as a response to the magnetic field have been observed experimentally [12][13]. However, this method experiences some disadvantages. For instance, the extra centrifugal force from the rotation will create an anti-trapping potential and compensate the confining potential in the transverse direction (i.e. the x and y direction). This imposes an upper limit to the rotation rate: $\Omega \leq \omega_x = \omega_y$, and to the strength of the effective magnetic field.

This, for instance, will inhibit systems from entering the more intriguing fractional quantum Hall regime.

Another way to create synthetic gauge fields is through atom-light interaction. This method is not constrained by the transversally isotropic trapping condition mentioned above. By forcing atoms to move in a properly designed laser field, the center of mass motion of the atoms will mimic the motion of charged particles in a magnetic field. The idea of using the light-atom interaction to create artificial magnetism is based on the understanding that the magnetism can be interpreted as the Aharonov-Bohm phase acquired by the particle when it travels around a closed contour. The phase the particle obtains after traveling around the closed loop is proportional to the magnetic flux that the loop has encircled. Therefore, to create an artificial magnetic field, we need a method in which a neutral particle can achieve a geometric phase after it moves around a closed contour. One classic example of geometric phases is Berry's phase. When a magnetic dipole moment in the presence of an external magnetic field moves slowly enough to follow the adiabatic eigenstate of the local field, the extra phase the dipole acquires after it completes a closed contour is the Berry's phase, which solely depends only on the geometry. Adapting this idea to neutral matter, adiabatically following the eigenstate of light-atom interaction, or the dressed state, will create a geometric phase, which contributes to the orbital magnetism we are looking for. In Subsection 1.1.1, we will review a two-level toy model [14] to demonstrate the above idea. In the Subsection 1.1.2, we extend our discussions to a multi-level system, where the adiabatic following of a dark state is used to create synthetic gauge fields. The challenges with this dressed state approach are heating and atom loss caused by spontaneous emission.

It is worth pointing out that the idea of adiabatic following of dressed states can also be used to generate non-Abelian gauge potentials when there are multiple *degenerate* internal states of atoms. The generations of Rashba spin-orbit coupling and the non-Abelian Aharonov-Bohm effect are possible in such non-Abelian gauge potentials. More discussions about synthetic spin-orbit coupling will be provided in later chapters.

One last method is through *pure* magnetic field scheme. This method is mainly proposed to generate 2D or 3D synthetic spin-orbit coupling for cold atoms [15] [16]. It avoids the heating problem in the above laser-dressed scheme. The idea of using inhomogeneous magnetic pulses to generate higher-dimensional SOCs lies in the heart of quantum mechanics. When we are solving quantum dynamics in a system's Hamiltonian involving two non-commuting operators, the propagator in general cannot be split directly into the product of propagators of those two operators. However, to lowest approximation, it is numerically allowed to do so. For instance, in the simplest simple harmonic oscillator case, $H = p_x^2/2m + m\omega^2 x^2/2$, the propagator is approximated as

$$e^{-iH\frac{\delta t}{\hbar}} \sim e^{-i\frac{p_x^2}{2m}\frac{\delta t}{\hbar}} e^{-i\frac{m\omega^2 x^2}{2}\frac{\delta t}{\hbar}}. \tag{1.1}$$

The commutator term is neglected after application of the Baker-Campbell-Hausdorff formula to the original propagator. The inverse process is proposed to create an effective dynamics with a Hamiltonian involving at least two non-commuting operators. In the following, we will take the Rashba spin-orbit coupling as an example, in which $[p_x\sigma_x, p_y\sigma_y] \neq 0$. The time evolution operator for a single cycle is given by

$$\begin{aligned}
&U(T,0)\\
&= \big[U_y(\delta t')e^{-i\frac{\hbar^2\vec{k}^2}{2m}\frac{\delta t}{\hbar}}U_y^\dagger(\delta t')\big] \times \big[U_x(\delta t')e^{-i\frac{\hbar^2\vec{k}^2}{2m}\frac{\delta t}{\hbar}}U_x^\dagger(\delta t')\big] \qquad (1.2)\\
&= \exp\big\{-i\frac{\hbar^2}{2m}\big[k_x^2 + (k_y + k_{\rm SO}F_y)^2\big]\frac{\delta t}{\hbar}\big\}\exp\big\{-i\frac{\hbar^2}{2m}\big[k_y^2 + (k_x + k_{\rm SO}F_x)^2\big]\frac{\delta t}{\hbar}\big\} \qquad (1.3)\\
&\simeq \exp\bigg\{-i\big[\frac{\hbar^2}{2m}(k_x^2 + k_y^2) + \frac{\hbar^2 k_{\rm SO}}{2m}(k_xF_x + k_yF_y) + \frac{\hbar^2 k_{\rm SO}^2}{4m}(F_x^2 + F_y^2)\big]2\frac{\delta t}{\hbar}\bigg\}\exp[O(\delta t^2)], \qquad (1.4)
\end{aligned}$$

where $F_{x,y,z}$ are the Pauli matrices for a spin-F particle, $\delta t'$ is the magnetic impulse duration and $U_\epsilon(\delta t') = \exp[-iE'_\epsilon \epsilon F_\epsilon \delta t'/\hbar]$ for $\epsilon = x, y$. E'_ϵ is proportional to the magnetic field gradient, B'_ϵ. From Eq. (1.2) to Eq. (1.3), we have assumed $E'_x = E'_y = E'$, $\hbar k_{\rm SO} = E'\delta t'$ and $T = 2\delta t$. The magnetic field gradient needs to be large enough to ensure the validity of the negligible pulse duration. The effective Rashba spin-orbit coupled Hamiltonian is realized by enforcing the error term, $O(\delta t^2)$, to be much smaller than 1. With this method, an arbitrary combination of Rashba and Dresselhaus spin-orbit coupled Hamiltonian can be created.

So far, our discussions have limited to the generation of gauge fields for atoms in the continuum. There are also lots of efforts put on creating gauge fields for atoms in optical-lattice systems, where interesting physics, such as the Hofstadter spectrum, could be emulated. Quantum mechanically speaking, the effect of a magnetic field on the motion of a charged particle is to imprint a Peierls phase onto the particle's wave function when the particle hopes between different lattice sites. The total phase accumulated after the particle moves a closed loop is proportional to the magnetic flux passing through the area enclosed by the loop. Therefore, to resemble the magnetic field, we need to come up with a method to create complex hopping amplitudes, $J = |J|e^{i\theta}$, where θ is the Peierls phase. Using a time-periodic driving of the lattice potential has resulted in a effective time-average Hamiltonian with non-trivial gauge potentials [17]. Another group has added a radio-frequency field together with the Raman field to reach a similar goal [18]. Two years later, the first research team has proposed to drive the lattice in a spin-dependent way such that synthetic spin-orbit coupling could be emulated in a time-binding lattice [19]. A spin-orbit coupled BEC in a translational lattice has been experimentally verified [20].

1.1.1 Two-level systems: adiabatic following of a dressed state

Assume we have a two-level atom with ground and excited states $|g\rangle$ and $|e\rangle$ in a light field. The general Hamiltonian of the atom in a laser field can be written as

$$H = (\frac{\vec{P}^2}{2M} + V)\hat{I} + U, \tag{1.5}$$

where M is the atomic mass, the momentum operator $\vec{P} = -i\hbar\nabla$, $\hat{I}$ is the 2×2 unit matrix in the internal 2D Hilbert space, and the potential V is independent of any internal degree of freedom of the atoms. U is the interaction Hamiltonian between the atom and the light field, which can be expressed in the basis set, $\{|g\rangle, |e\rangle\}$, as

$$U = \frac{\hbar\Omega}{2}\begin{pmatrix} \cos\theta & e^{-i\phi}\sin\theta \\ e^{i\phi}\sin\theta & -\cos\theta \end{pmatrix}, \tag{1.6}$$

where Ω is the generalized Rabi frequency, ϕ is the phase angle, and θ is the mixing angle. For a two-level atom in a monochromatic laser field, the physical meaning of ϕ is simply the phase of the laser field. As for the mixing angle, it contains two pieces of information: $\Omega\sin\theta$ is the strength of the atom-light coupling and $\Omega\cos\theta$ is the detuning. The derivation of the atom-field interaction Hamiltonian U is provided in Appendix A and the angles ϕ and θ are expressed in a physically transparent form there. Diagonalizing the matrix U, we find that the eigenstates of the atom-light interaction Hamiltonian are

$$|\chi_1\rangle = \begin{pmatrix} \cos\frac{\theta}{2} \\ e^{i\phi}\sin\frac{\theta}{2} \end{pmatrix} \tag{1.7}$$

$$|\chi_2\rangle = \begin{pmatrix} -e^{-i\phi}\sin\frac{\theta}{2} \\ \cos\frac{\theta}{2} \end{pmatrix}, \tag{1.8}$$

with the corresponding eigenenergies $\hbar\Omega/2$ and $-\hbar\Omega/2$. These two eigenstates are called *dressed states.* Note that these two dressed states form a complete set in a two dimensional Hilbert space, so we can use $|\chi_1\rangle$ and $|\chi_2\rangle$ to expand the full state vector $|\Psi(\vec{r},t)\rangle$ of the total Hamiltonian, that is,

$$|\Psi(\vec{r},t)\rangle = \sum_{j=1,2}\psi_j(\vec{r},t)|\chi_j(\vec{r})\rangle. \tag{1.9}$$

Next, we will show that the effective Hamiltonian of the center of mass of an atom is identical to that of a charged particle in a magnetic field when the internal state of the atom follows adiabatically one of its dressed states. Thus, a neutral object moving in a properly designed laser field behaves similarly to a charged particle in a magnetic field.

Suppose the atom is initially in one of the dressed states, say $|\chi_1\rangle$. If the atom does not change its motion significantly, then the internal state of the atom will remain proportional to the initial internal dressed state, $|\chi_1\rangle$. This is possible if the absorption or emission of a photon by an atom involves only a small momentum change, $\Delta k \sim k_R$, where k_R is the recoil momentum. To apply the adiabatic approximation, we require the recoil energy to be much less than the energy difference of the two levels.

Due to the adiabatic assumption we make above, the atomic population in the other internal state, $|\chi_2\rangle$ is almost zero. Next we will derive the equation of motion for $\psi_1(\vec{r},t)$ by assuming that $\psi_2(\vec{r},t) = 0$. Plugging Eq. (1.9) into the time-dependent Schrödinger Equation, $i\hbar\frac{\partial}{\partial t}|\Psi(\vec{r},t)\rangle = H|\Psi(\vec{r},t)\rangle$, we get

$$\begin{aligned}
i\hbar\frac{\partial}{\partial t}|\Psi(\vec{r},t)\rangle =&(\frac{\vec{P}^2}{2M} + V + U)|\Psi(\vec{r},t)\rangle \\
=&\frac{\vec{P}}{2M}\cdot\sum_{l=1,2}\big[(\vec{P}\psi_l)|\chi_l\rangle + \psi_l(\vec{P}|\chi_l\rangle)\big] + V|\Psi(\vec{r},t)\rangle + \frac{\hbar\Omega}{2}\sum_{j=1,2}\psi_j|\chi_j\rangle \\
=&\frac{\vec{P}}{2M}\cdot\sum_{j,l=1,2}\big[(\delta_{j,l}\vec{P} - \vec{A}_{jl})\psi_l\big]|\chi_j\rangle + V|\Psi(\vec{r},t)\rangle + \frac{\hbar\Omega}{2}\sum_{j=1,2}\psi_j|\chi_j\rangle \\
=&\sum_{j,l=1,2}\delta_{j,l}\Big(\frac{P^2}{2M}\psi_l\Big)|\chi_j\rangle - \sum_{j,l,m=1,2}\delta_{j,l}\vec{A}_{mj}\cdot\Big(\frac{\vec{P}}{2M}\psi_l\Big)|\chi_m\rangle \\
&-\frac{1}{2M}\sum_{j,l=1,2}\big[(\vec{P}\cdot\vec{A}_{jl})\psi_l\big]|\chi_j\rangle + \frac{1}{2M}\sum_{j,l,m=1,2}\big[\vec{A}_{mj}\cdot(\vec{A}_{jl}\psi_l)\big]|\chi_m\rangle \\
&+V|\Psi(\vec{r},t)\rangle + \frac{\hbar\Omega}{2}\sum_{j=1,2}\psi_j|\chi_j\rangle, \qquad (1.10)
\end{aligned}$$

where $\vec{A}_{jl} \equiv i\hbar\langle\chi_j|\nabla\chi_l\rangle$. Notice that from the second equality to the third one, we have inserted an identity operator, $\hat{I} = \sum_j |\chi_j\rangle\langle\chi_j|$. Letting ψ_2=0, Eq.(1.10) is simplified to be

$$\begin{aligned}
&i\hbar\dot{\psi}_1|\chi_1\rangle \\
&= \Big\{\big[\frac{P^2}{2M} - \vec{A}_{11}\cdot\vec{P} - \vec{P}\cdot\vec{A}_{11} + \vec{A}_{11}^2\big]\psi_1\Big\}|\chi_1\rangle + \frac{\vec{A}_{12}\cdot\vec{A}_{21}}{2M}\psi_1|\chi_1\rangle + \Big(V + \frac{\hbar\Omega}{2}\Big)\psi_1|\chi_1\rangle.
\end{aligned}$$

(1.11)

Projecting Eq.(1.11) onto the internal state $|\chi_1\rangle$, we get

$$\begin{aligned} i\hbar\frac{\partial}{\partial t}\psi_1(\vec{r},t) &= \frac{(\vec{P}-\vec{A}_{11})^2}{2M}\psi_1 + \frac{\vec{A}_{21}\cdot\vec{A}_{12}}{2M}\psi_1 + V\psi_1 + \frac{\hbar\Omega}{2}\psi_1 && (1.12)\\ &= \left[\frac{(\vec{P}-\vec{A}_{11})^2}{2M} + V + \frac{\hbar\Omega}{2} + \frac{\vec{A}_{21}\cdot\vec{A}_{12}}{2M}\right]\psi_1 && (1.13)\\ &\equiv \left[\frac{(\vec{P}-\vec{A})^2}{2M} + V + \frac{\hbar\Omega}{2} + W\right]\psi_1, && (1.14)\end{aligned}$$

where

$$\vec{A} \equiv \vec{A}_{11} = i\hbar\langle\chi_1|\nabla\chi_1\rangle = \hbar/2(\cos\theta - 1)\nabla\phi \quad (1.15)$$

$$W \equiv \vec{A}_{12}\cdot\vec{A}_{21}/2M = \hbar^2/2M|\langle\chi_2|\nabla\chi_1\rangle|^2 = \hbar^2/8M[(\nabla\theta)^2 + \sin^2\theta(\nabla\phi)^2]. \quad (1.16)$$

Potentials $\vec{A}$ and W are independent of the coupling strength Ω and dependent on the position the particle follows, so they can be characterized as geometric potentials. These two geometric potentials appear on the effective center-of-mass equation of motion after the adiabatic elimination of the other dressed state. Eq.(1.14) bears a striking resemblance to the equation of motion for a charged particle in an external field. The geometric potential $\vec{A}$ behaves as the vector gauge potential, and the potential W is the scalar gauge potential after we set the effective charge to be 1.

If the curl of the vector potential is nonzero, then it is impossible to gauge away $\vec{A}$ by a simple gauge transformation. The artificial magnetic field in the atomic system is then

$$\vec{B} = \nabla\times\vec{A} = \frac{\hbar}{2}\nabla(\cos\theta)\times\nabla\phi. \quad (1.17)$$

A nonzero magnetic field exists when $\nabla(\cos\theta)\times\nabla\phi \neq 0$, which implies the phase angle of the light field and the mixing angle should both be space-dependent and their gradients should not align along the same direction. The spatial dependence of the phase angle comes naturally. For example, for light propagating in the x direction, $\phi = kx$, so $\nabla\phi = k\hat{x}$. As for a nonzero value for $\nabla\cos\theta$, two different configurations can achieve that. The first one is uses a spatial dependance of the coupling strength of the atom-laser interaction. The other possibility is to have a spatially-dependent detuning. The main concern with this single laser method is the lifetime of the excited state. Only atoms with a long radiative lifetime can be adapted to this configuration, for example, the alkaline-earth species are good candidates. For those atoms, the life time of the excited state could be in the order of seconds.

1.1.2 Multiple-level systems: dark state scheme

To apply the light-dressed approach to a large class of atoms, like the widely used alkali atoms, schemes involving more than one laser beam to couple the multiple atomic levels are proposed. Making use of quasi-degeneracy of the energy levels, dressed states, which are purely linear combinations of the ground states, $|g_i\rangle$, is desirable since the short lifetime problem of excited states for some species of atoms are cleverly avoided. These special dressed states are called *dark* states. They have plenty of applications such as electromagnetically induced transparency (EIT) and stimulated Raman adiabatic passage (STIRAP). Preparing atoms in such a dressed state and adiabatically following it will generate artificial gauge potentials on the atoms. We will illustrate one example of making use of the dark state through a tripod scheme to generate an artificial magnetic field in the following.

Consider a Λ-type atom with two almost degenerate ground states ($|g_1\rangle$ and $|g_2\rangle$) and one excited state ($|e\rangle$). Applying two lasers to couple the ground state to exited state transition, ($|g_1\rangle$ to $|e\rangle$ and $|g_2\rangle$ to $|e\rangle$), the Hamiltonian describing the system can be written as

$$U = \frac{\hbar}{2}\begin{pmatrix} -2\delta & \kappa_1^* & 0 \\ \kappa_1 & 0 & \kappa_2 \\ 0 & \kappa_2^* & 2\delta \end{pmatrix}, \tag{1.18}$$

where κ_1 and κ_2 are the Rabi frequencies and δ is the detuning of the laser frequency with respect to the ground-excited transition. For simplicity, the two lasers here are tuned symmetric with respect to the average of the $g_1 - e$ and $g_2 - e$ transition frequencies, see Fig. 1.1. Assuming that the two-photon transition is resonant with the

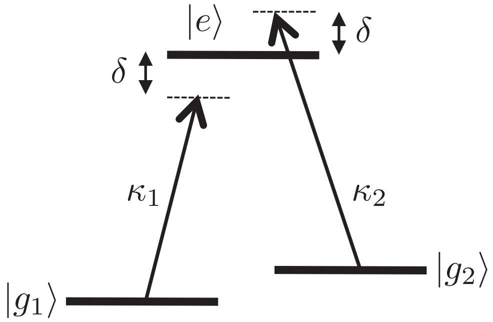

Figure 1.1.: Λ-type atoms. This figure is taken from Ref. [14].

transition between two ground states, that is, $2\delta = 0$. Diagonalizing the Hamiltonian in Eq. (1.18), we get the three dressed states:

$$|D\rangle = \frac{1}{\sqrt{|\kappa_1|^2 + |\kappa_2|^2}}(\kappa_2|g_1\rangle - \kappa_1|g_2\rangle) \tag{1.19}$$

$$|\pm\rangle = \frac{1}{\sqrt{2}}\left(\frac{1}{\sqrt{|\kappa_1|^2 + |\kappa_2|^2}}(\kappa_1^*|g_1\rangle + \kappa_2^*|g_2\rangle) \pm |e\rangle\right) \equiv \frac{1}{\sqrt{2}}(|B\rangle \pm |e\rangle), \tag{1.20}$$

where the dark state, $|D\rangle$, is decoupled from the excited state as opposed to the bright state, $|B\rangle$. Notice that $\langle B|D\rangle = \langle D|B\rangle = 0$. The dressed state energies for $|D\rangle$ and $|\pm\rangle$ are 0 and $\pm\frac{\hbar}{2}\sqrt{|\kappa_1|^2 + |\kappa_2|^2}$ respectively.

Following a similar procedure as in subsection 1.1.1, we expand the state vector in terms of the complete set formed by the three dressed states,

$$|\Psi(\vec{r})\rangle = \sum_{X=D,\pm} \psi_X(\vec{r})|X(\vec{r})\rangle, \tag{1.21}$$

and assume that the atom moves adiabatically so that it keeps staying in the dark state, therefore, we can approximate the state vector with $|\Psi(\vec{r})\rangle \approx \psi_D(\vec{r})|D(\vec{r})\rangle$. After projecting out the dark state, we get the effective equation of motion for the center of mass of the Λ-type atom,

$$i\hbar\frac{\partial\psi_D(\vec{r},t)}{\partial t} = \left[\frac{(\vec{P} - \vec{A})^2}{2M} + V(\vec{r}) + W(\vec{r})\right]\psi_D(\vec{r},t), \tag{1.22}$$

where the effective vector potential $\vec{A} = i\hbar\langle D|\nabla D\rangle$ and the effective scalar potential $W = \frac{\hbar^2}{2M}|\langle B|\nabla D\rangle|^2$. This result is very similar to the one we get in the two-level atom case if we relate the dressed state $|D\rangle$ ($|B\rangle$) to $|\chi_1\rangle$ ($|\chi_2\rangle$). Comparing the vector potential and scalar potential for tripod scheme with the two-level scheme in Eq.(1.15) and Eq. (1.16), we see that the phase angle, ϕ, now is replaced by the phase difference of the Raman lasers $\phi_1 - \phi_2$ and the mixing angle θ now is related to the ratio of the two Raman couplings by $\tan(\frac{\theta}{2}) = -|\kappa_1|/|\kappa_2| \equiv -\sqrt{\zeta}$. Accordingly, we can derive the formula for the effective magnetic field,

$$\vec{B} = \nabla \times \vec{A} = \hbar \frac{\nabla\phi \times \nabla\zeta}{(1+\zeta)^2}. \tag{1.23}$$

Similar to the two-level case, to have a non-zero magnetic field, an inhomogeneous phase angle and mixing angle are required and the gradients of them cannot be parallel to each other. This can be implemented with the usage of lasers carrying orbital angular-momentum [21]. This can be made possible by preparing the laser beams in Laguerre-Gauss modes. Another configuration being proposed to realize an artificial magnetic field is through two counter-propagating laser beams with shifted center [22]. The first realization of synthetic gauge fields at NIST with the dressed atom approach is also based on the adiabatic idea we have discussed so far (although they are not using a dark state). We will discuss it more in later chapters. Please refer to chapter 2 for details.

1.2 Overview of scattering theory

Many branches of physics reply on scattering theory to explain scattering experiments that convey important information about the projectile, the target and the force between them. It shapes our understanding to the physical world. For instance, in atomic physics, the famous Rutherford's experiment has led to the discovery of nucleus by scattering an alpha particle off a gold foil. In particle physics, the collision experiments of a photon with a neutron have taught us that a neutron has an internal structure and composes of three quarks with fractional charges ($0e = \frac{2}{3}e - \frac{1}{3}e - \frac{1}{3}e$). Scattering theory is such an extensive subject that a complete review would be very involved. However, it is helpful at least to have a categorical understanding of it.

Depending on the incident particles' speed, there are relativistic and non-relativistic scattering theories. From the number of possible final configurations, there are single-channel and multi-channel scattering theories. Another devision of scattering theory is whether it is time-dependent or time-independent. Although there are a lot of varieties in collision theory, the essential features are similar. Basically we want to answer how the interaction between the projectile and the target changes the initial freely-propagating state to another asymptotically free final state. The operator connecting the initial state to the final state is defined as the scattering operator, S.

$$|\Psi_{\text{out}}\rangle = \hat{S}|\Psi_{\text{in}}\rangle, \tag{1.24}$$

where the scattering operator, S, contains all the information of experimental relevance. One important goal in scattering calculations is then directed to find the S matrix.

In subsection 1.2.1, we illustrate the one-body scattering formalism can still be applied in two-body scattering when we move to the center-of-mass frame when the system is *separable*. In subsection 1.2.2, we discuss the scattering theory for a finite-range local potential and then focus on spherically-symmetric potentials in subsection 1.2.3. The idea of partial waves and scattering phase shifts will be explained. In subsection 1.2.4, we consider the ultracold scattering, in which the experimental breakthroughs in the atom cooling and trapping have revived the interests. The most important concept, the scattering length, in ultracold collisions will be elaborated.

1.2.1 The two-body problem

In quantum mechanics, we have learned many counterintuitive physical phenomena about one-particle scattering off different types of static potentials. In two-body scattering, the degree of freedom in the system increases to six in three spatial dimensions. Rather than working in the two separate particle coordinates, physicists use instead the center-of-mass coordinates and the relative coordinates to describe the two-body scattering.

$$\hat{H}_{\mathrm{2b}} = \hat{H}_1 + \hat{H}_2 = \frac{\vec{p}_1^{\,2}}{2m_1} + \frac{\vec{p}_2^{\,2}}{2m_2} + V(\vec{r}_1 - \vec{r}_2) \tag{1.25}$$

$$= H_{\mathrm{com}} + H_{\mathrm{rel}} = \frac{\vec{P}^2}{2M} + \frac{\vec{p}^{\,2}}{2\mu} + V(\vec{r}), \tag{1.26}$$

where $M = m_1 + m_2$, $\mu = \frac{m_1 m_2}{m_1+m_2}$, $\vec{P} = \vec{p}_1 + \vec{p}_2$, $\vec{R} = \frac{m_1\vec{r}_1 + m_2\vec{r}_2}{m_1+m_2}$, $\vec{p} = \frac{m_2\vec{p}_1 - m_1\vec{p}_2}{m_1+m_2}$, and $\vec{r} = \vec{r}_1 - \vec{r}_2$. Notice that the new operators satisfy the usual commutation relations.

$$[\vec{R}_j, \vec{P}_k] = i\hbar\delta_{j,k} \text{ for } j,k = x,y,z \tag{1.27}$$

$$[\vec{r}_j, \vec{p}_k] = i\hbar\delta_{j,k} \text{ for } j,k = x,y,z \tag{1.28}$$

$$[\vec{R}_j, \vec{p}_k] = 0 \text{ for } j,k = x,y,z \tag{1.29}$$

$$[\vec{r}_j, \vec{P}_k] = 0 \text{ for } j,k = x,y,z \tag{1.30}$$

The advantage of adopting this new set of coordinates is based on the following argument. The Newton's third law tells us that two massive particles exert equal and opposite forces on each other. Since the two particles interact and respond to each other, the two-body interaction should depend only on their relative coordinate, see Eq. (1.25). This tells us that the center-of-mass motion is a simple free-particle motion. Therefore, in the two-body problem, what we are solving is the relative motion, and thus only involves three spatial degrees of freedom instead of six.

However, in some cases, the center-of-mass motion cannot be decoupled from the relative motion due to the existence of some special single-particle potentials on each particle. In those cases, we can only solve the problem with the full degree of freedom. For instance, as the reader will see in the later chapter, when the spin-orbit coupling exists in the two-body system, the center-of-mass motion is in general coupled to the relative motion unless we consider the case of a zero center-of-mass momentum. For another instance, for two trapped particles, if the trapping frequencies of these two particles are different, then the center-of-mass motion is coupled to the relative one. We often call these cases *nonseparable*.

1.2.2 The scattering amplitude and the cross sections

Considering a *separable* two-body collision in 3D, the problem we are solving is reduced to a *relative* particle with mass μ in an external potential $V(\vec{r})$. The Schrödinger equation governing the motion of the relative particle is expressed as

$$\left(\frac{\vec{p}^2}{2\mu} + V(\vec{r})\right)\psi(\vec{r}) = E\psi(\vec{r}), \tag{1.31}$$

where $V(\vec{r})$ is assumed to be a finite-range local potential, meaning the potential operator is diagonal in the position representation

$$\langle\, \vec{r}\,'|\hat{V}|\, r\,\rangle = V(\vec{r})\delta(\vec{r} - \vec{r}\,'). \tag{1.32}$$

A scattering solution satisfying Eq. (1.31) can be expressed as a superposition state of the incoming plane wave and the outgoing spherical wave at $|\vec{r}| \to \infty$. The large distance limit allows us to ignore the finite distribution of the short-range potential at the detector. Thus,

$$\begin{aligned} \psi = \psi_{\text{inc}} + \psi_{\text{sc}} &= e^{i\vec{k}\cdot\vec{r}} + f(\vec{k}, \vec{k}')\frac{e^{ikr}}{r} \text{ at } |\vec{r}| \to \infty && (1.33) \\ &= e^{i\vec{k}\cdot\vec{r}} + f(k, \hat{n}, \hat{n}')\frac{e^{ikr}}{r} \text{ at } |\vec{r}| \to \infty. && (1.34) \end{aligned}$$

The first term describes the incoming plane wave with a fixed momentum $\vec{k}$ pointing along the direction, $\hat{n} \equiv \hat{k}/|\vec{k}|$. The convention is in the z direction. The vector $\hat{k}'$ represents the propagating vector of for waves arriving at the observation point, $\vec{r}$, so the direction of $\vec{k}'$ is defined as $\hat{n}' \equiv \vec{r}/|\vec{r}|$. Since we are dealing with a single-channel elastic scattering, $\vec{k}$ and $\vec{k}'$ differ only in the direction (from $\hat{n}$ to $\hat{n}'$) with an equal magnitude $|\vec{k}| = |\vec{k}'| \equiv k$. The second term represents an outgoing spherical wave with a coefficient $f(\vec{k}, \vec{k}')$, which is determined by the scattering potential, $V(r)$. The coefficient, f, is named as the *scattering amplitude*. If $f = 0$, it means the incoming wave passes through the potential as if there is no any obstacle at all. Effectively, there is no scattering at all. The scattering amplitude is one of the most important properties to characterize the scattering process, since it is directly related to the experimentally measurable quantities, *cross sections*.

$$\frac{d\sigma}{d\Omega} = |f(\vec{k}, \vec{k'})|^2 \tag{1.35}$$

$$\sigma = \int \frac{d\sigma}{d\Omega} d\Omega = \int |f(\vec{k}, \vec{k'})|^2 d\Omega \tag{1.36}$$

Eq. (1.35) stands for the differential cross section and Eq. (1.36) states the total cross section after integrating over the solid angle in Eq. (1.35). At subsection 1.2.3, we will see the close connection of the scattering amplitude, f, and the scattering operator, S.

What we have presented so far is the scattering theory for two *spinless* particles in a single-channel case. In general, particles can carry spins and can have multiple channels to be scattered from and to. Also, if the two scattered particles are identical, we need to carefully perform symmetrization or anti-symmetrization of the wave function. John Taylor's book on scattering theory [23] gives a very thorough analysis to all kinds of scattering problems. We refer readers to his book for further details.

1.2.3 Partial-wave expansion

In this subsection, we focus our discussions on the short-range spherically-symmetric interactions to gain more insights into the scattering amplitude. By spherical symmetric interactions, we mean the potential is invariant under any rotation in 3D, so $V(\vec{r}) = V(r)$ in Eq. (1.31). By short-range interaction, we mean the potential goes to zero as $r \to \infty$. It guarantees that the relative particle propagates freely at asymptotic regimes. The condition ensuring that is generally very complicated. For spherical potentials, the potential should satisfy the following three properties [23]:

(I) $V(r) = O(r^{-3-\epsilon})$ as $r \to \infty$ (with $\epsilon > 0$)

(II) $V(r) = O(r^{-2+\epsilon})$ as $r \to 0$ (with $\epsilon > 0$)

(III) $V(r)$ is continuous for $0 < r < \infty$.

The first two conditions require that the short-range potential to decay faster than $1/r^3$ at infinity and behave less singularly than $1/r^2$ as $r \to 0$. Thus, the first condition excludes the Coulomb interaction ($\sim 1/r$) and the dipole-dipole interaction ($\sim 1/r^3$). Some refer them as *long-range* interactions in this context.

Since the potential is spherically symmetric, the scattering outcome should depend only on the angle between the incident wave direction and the observation direction. Defining $\cos\theta = \hat{n}\cdot\hat{n}'$, the scattering amplitude is reduced to

$$f(k,\hat{n},\hat{n}') = f(k,\theta) \quad \text{for} \quad V(\vec{r}) = V(r). \tag{1.37}$$

One convenient convention is to assume the incident wave comes in the z direction, so the detector position is $\vec{r} = \{r,\theta,\phi\}$ in the familiar 3D spherical coordinate. The scattering amplitude can be found by first expanding the scattering solution in terms of the spherical harmonics, $Y_l^m(\theta,\phi)$. The angular momentum basis is perfect for the case here since the rotational invariance of the scattering potential assures the angular momentum conservation. Therefore, the expansion radial wave function, $u_{k,l,m}(r)$ does not couple to $u_{k,l',m'}$ when $l \neq l'$ and $m \neq m'$.

$$\psi_{\vec{k}}(\vec{r}) = \sum_{l=0}^{\infty}\sum_{m=-l}^{l} \frac{u_{k,l,m}(r)}{r} Y_l^m(\theta,\phi), \tag{1.38}$$

where ϕ is the azimuthal angle with respect to the z direction. Plugging in the expansion into Eq. (1.31), we simplify the problem from solving a 3D partial differential equation into a 1D radial differential equation.

$$\frac{-\hbar^2}{2\mu} u''_{k,l}(r) + \left(\frac{l(l+1)\hbar^2}{2\mu r^2} + V(r)\right) u_{k,l}(r) = E u_{k,l}(r) \tag{1.39}$$

where $E = \frac{\hbar^2 k^2}{2\mu}$. For a given l, the solutions are identical for all $m = -l, ..., l$, so we remove the label of m of the radial function by choosing $m = 0$ in Eq. (1.39). The term $\frac{l(l+1)\hbar^2}{2\mu r^2}$ is called the centrifugal potential, which is the source of shape resonances for $l \neq 0$.

The plane wave can be expanded as follows with angular momentum algebra.

$$e^{ikz} = e^{ikr\cos\theta} = \sum_{l=0}^{\infty} i^l (2l+1) j_l(kr) P_l(\cos\theta) \tag{1.40}$$

$$\xrightarrow[kr\to\infty]{} \frac{1}{2ik}\sum_{l=0}^{\infty}(2l+1)\left(\frac{e^{ikr}}{r} + (-1)^{l+1}\frac{e^{-ikr}}{r}\right) P_l(\cos\theta), \tag{1.41}$$

where $j_l(kr)$ are the spherical Bessel functions and $P_l(\cos\theta)$ are the Legendre polynomials. At very large distances, the plane wave can be viewed as a sum of a superposition of an incoming wave of $e^{-ikr}P_l(\cos\theta)/r$ and an outgoing wave, $e^{ikr}P_l(\cos\theta)/r$, in each angular momentum, l.

The key point of finding the scattering amplitude is to realize that the scattering solution at the infinite r should (i) reduce to the free particle wave function with *only* some extra phase shifts, $\delta_l(k)$, that is, the solution to Eq. (1.39) at $r \to \infty$ is

$$u_{k,l}(r) \underset{r\to\infty}{\longrightarrow} \sin(kr - l\pi/2 + \delta_l(k)), \tag{1.42}$$

and (ii) carry the same incident wave information as in Eq. (1.41), which are the boundary conditions we should satisfy. Therefore, we can show that the scattering solution can be written as

$$\psi_{\vec{k}}(r) \underset{kr\to\infty}{\longrightarrow} e^{ikz} + \sum_{l=0}^{\infty}(2l+1)\left(\frac{e^{2i\delta_l}-1}{2ik}P_l(\cos\theta)\right)\frac{e^{ikr}}{r}. \tag{1.43}$$

Thus, the scattering amplitude is

$$f(\theta) = \sum_{l=0}^{\infty}(2l+1)f_l(k)P_l(\cos\theta), \tag{1.44}$$

where

$$f_l(k) = \frac{S_l(k)-1}{2ik} \qquad \text{with } \ S_l(k) = e^{2i\delta_l}. \tag{1.45}$$

The notation S_l in Eq. (1.45) stands for the *partial wave S matrix element* and δ_l is the *scattering phase shift* for the partial wave of l. Accordingly, we can calculate the cross sections in each partial waves. The total cross sections are the sum of all partial wave cross sections since the orthogonality of the Legendre polynomials will cancel all interference terms between different angular momenta. Therefore,

$$\sigma = \sum_l \sigma_l \text{ with } \sigma_l = \frac{4\pi}{k^2}(2l+1)\sin^2\delta_l(k). \tag{1.46}$$

From the above equation, we see that there is an upper bound for each partial-wave cross section.

$$\sigma_l < \sigma_{l,\max} = \frac{4\pi}{k^2}(2l+1), \tag{1.47}$$

which is called the *unitary bound.* It is a direct result of the unitarity of the S matrix. The unitary limit is reached when $\delta_l = n\pi/2$ for odd n.

1.2.4 Low-energy scattering

The simplest way to understand ultracold scattering is to explore the solution of the Schrödinger equation in Eq. (1.39) at $E = 0$ and $l = 0$. For $r > r_0$, where r_0 is the range of the potential, the radial wave function satisfies

$$\frac{d^2u}{dr^2} = 0 \tag{1.48}$$

The answer to Eq. (1.48) is nothing but a straight line with

$$u(r) = A(r - a), \tag{1.49}$$

where A and a are constants. One way to interpret the solution is to imagine a free sinusoidal wave with an infinitely long wavelength. From Eq. (1.42), we know that

$$\lim_{k\to 0} \sin(kr + \delta_0) = \lim_{k\to 0} \sin\left[k\left(r + \frac{\delta_0}{k}\right)\right], \tag{1.50}$$

so it behaves the same as the solution up to some normalization constants in Eq. (1.49) when $k \to 0$. From Eq. (1.49) and Eq. (1.50), we derive

$$\frac{u'}{u} = k\cot\left[k\left(r + \frac{\delta_0}{k}\right)\right] = \frac{1}{r-a} \quad \text{for} \quad k \to 0 \tag{1.51}$$

Taking $r \to 0$, we reach the eqality,

$$\lim_{k\to 0} k\cot\delta_0 = -\frac{1}{a}, \tag{1.52}$$

where a is known as the *s-wave scattering length.* From the above identity, we can show that the s-wave cross section is

$$\sigma_0 = 4\pi|f_0|^2 = 4\pi\left|\frac{e^{2i\delta_0} - 1}{2ik}\right|^2 = 4\pi\left|\frac{e^{i\delta_0}\sin\delta_0}{k}\right|^2 = 4\pi\left|\frac{1}{k\cot\delta_0 - ik}\right|^2 \xrightarrow[k\to 0]{} 4\pi a^2, \tag{1.53}$$

where the factor 4π comes from the solid angle integration. So far, we have seen three different ways of understanding the meaning of s-wave *scattering length*:
(i) the intercept of the radial wave function with the r-axis,
(ii) a physical quantity, which is related to the phase shift by $\tan\delta_0 = -ka$,
(iii) the effective range of scattering occurs in a classical sense.
Later on, we will see that a also characterizes how strong the interaction in ultracold scattering in the pseudo-potential theory. Also, a scattering length can have energy dependence if we go to a higher order of accuracy. For our purpose, we don't discuss it here. For interested readers, we refer them to the *effective-range theory* [24].

For partial waves with nonzero value of l, the partial-wave phase shifts can be shown to be scaled as $\delta_l(k) \propto k^{2l+1}$ modulo π. Since

$$\sigma_{l\neq 0} = \frac{4\pi}{k^2}(2l+1)\sin^2\delta_l \propto k^{4l} \to 0 \quad \text{as} \quad k \to 0, \tag{1.54}$$

the cross sections of higher-partial waves go to zero as $k \to 0$. One intuitive way to understand that is by noticing that when the collision energy is much lower than the centrifugal barrier, which exists only for $l \neq 0$, the particle cannot penetrate the barrier to probe the potential, and thus gets reflected directly. Therefore, at very low temperatures, s-wave scattering dominates and the scattering length, a, is almost the most important quantity in the field of ultracold atomic physics.

1.3 Outline of the thesis

The dissertation is organized as follows: in chapter 2, we first review the first realization of synthetic gauge fields in ultracold quantum gases with the dressed atom approach. Spin-orbit coupling, is shown to be a special case of synthetic gauge fields. Discussions on the novelty of the spin-orbit coupled BECs are given with a focus on the dynamics. The non-adiabatic dynamics in spin-orbit coupled BECs are studied and a quantitative agreement with the celebrated Landau-Zener model is reached. The theoretical calculations are confirmed by the experimental group of Prof. Yong

P. Chen at Purdue, and the experimental results will be discussed. The breakdown of the Landau-Zener model is discussed at the end of the chapter.

Chapter 3 presents a generalized low-energy scattering theory for the isotropic spin-orbit coupling within the pseudo-potential approximation. A systematic method is introduced to analytically solve a class of coupled differential equations by recasting the coupled-channel problem as a simple eigenvalue problem. The exact Green's matrix in the presence of SOC is found, which readily gives the scattering solutions for any two identical particles in any total angular momentum subspace having negligible center-of-mass momentum. Application of this formalism to two spin-1 bosons is provided. The ubiquitous low-energy threshold behavior for systems with isotropic SOC is calculated and the relevant physics is discussed. Additionally, by searching for the poles of the S matrix, a two-body bound state is found for any arbitrarily small and negative scattering length due to the huge degeneracy provided by the isotropic spin-orbit coupling.

In Chapter 4, we calculate the reflection and transmission amplitudes in a one-dimensional Fermi gas with an equal mixing of the Rashba and Dresselhaus spin-orbit coupling (RD-SOC) under an external Raman laser field for all energy range within the pseudo-potential approximation. We show that the presence of RD-SOC together with the Raman field fundamentally change the scattering behavior and can be used to realize very different one-dimensional theoretical models in a single experimental setup. A realistic estimation of experimental parameters is provided with the assistance of confinement-induced resonances (CIRs).

The last chapter summarizes the studies done in the thesis and discusses also possible relevant future work. A focus will be given to the Efimov physics. Since SOC introduces a new scale into the thee-body system, it would be very interesting to study whether there still exists universal three-body bound states, if the answer is yes, and then how the new scale is incorporated into the universal scaling law. The other interesting direction is to explore the interplay of SOC and the higher-partial waves. A general treatment to any types of short-range potential is introduced there to be able to incorporate contributions from higher-partial waves. Other possible extensions will be discussed as well.

2. NON-ADIABATIC DYNAMICS OF A DRIVEN SPIN-ORBIT COUPLED BEC

When BECs were first achieved, physicists were trying to study this new form of matter (although predicted long time ago by Satyendra Nath Bose and Albert Einstein in 1924-1925) by *poking* it in different ways. Releasing two condensates from a double-well potential and allowing them to expand freely, Ketterle's group has observed an interference pattern in the overlapping region, where they met [25]. This demonstrates the phase coherence feature of a condensate when all the atoms occupy the same ground state. By time-modulating the magnetic trapping potential, the shape oscillation is observed [26]. The condensate changes its lengths and aspect ratios periodically with a frequency of the order of the trapping frequency as a response to the modulation. Study of collective excitations of tapped condensates as a many-body system has been an important probe to explain the properties of BECs. Similar explorations of spin-orbit coupled BECs have happened since their first realization in 2011 [27]. Different experiments show different interesting aspects of spin-orbit coupled BECs. Here, we will mainly focus on three topics: phase diagrams, elementary excitations, and dynamics. Through reviewing recent research studies, the novel features of spin-orbit coupled BECs will be depicted. After that, we focus mostly on the non-adiabatic dynamics of SO-coupled BECs.

This chapter is written based on the publication in Phys. Rev. A, **90**, 013616 (2014) and is organized as follows. In Sec. 2.1, we first review the realization of spin-orbit coupled BECs in NIST experiments and then discuss properties of SO-coupled BECs through a series of theoretical and experimental works after that. Later in Sec. 2.2.1, we talk about the classic model studying the non-adiabatic dynamics: the Landau-Zener model. Motivations for studying non-adiabatic dynamics in cold atom systems will be described. In Sec. 2.2.3 and 2.2.4, we show that the driven dynamics in spin-orbit coupled BECs matches very well with the predictions given by the Landau-Zener model for both numerical simulations and experiments in the semi-classical limit [28]. Discussions about the breakdown of Landau-Zener model in certain parameter space will be provided. This point has been addressed in a follow-up paper by Bo Xiong *et al.* [29]. Interesting predictions given there considering the multichannel effect will be sketched too.

2.1 Light-induced gauge potentials: NIST Experiments

Yu-Ju Lin *et al.* first generated a constant vector gauge potential in a Bose-Einstein condensate of ^{87}Rb through atom-light interaction in 2009 [30]. The three Zeeman-split F=1 hyperfine states in Rb atoms are coupled through two-photon transitions by applying two *counter-propagating* lasers with perpendicular linear polarizations ($\hat{z}$ and $\hat{y}$) and a small frequency shift (ω_L and $\omega_L + \Delta\omega_L$) along the x direction. Under the rotating wave approximation, the Hamiltonian describing the system in the frame rotating at $\Delta\omega_L$ can be written, in the internal basis states: $|F, m_F\rangle = |1, -1\rangle$, $|1, 0\rangle$, and $|1, 1\rangle$, as

$$H = \begin{pmatrix} \frac{p_x^2}{2m} - \hbar\delta & \frac{\hbar\Omega}{2} e^{2ik_L x} & 0 \\ \frac{\hbar\Omega}{2} e^{-2ik_L x} & \frac{p_x^2}{2m} - \hbar\epsilon & \frac{\hbar\Omega}{2} e^{2ik_L x} \\ 0 & \frac{\hbar\Omega}{2} e^{-2ik_L x} & \frac{p_x^2}{2m} + \hbar\delta \end{pmatrix}, \tag{2.1}$$

where $k_L = 2\pi/\lambda$, λ is the laser wavelength, $\delta = \Delta\omega_L - \omega_Z$ is the detuning, Ω is the Raman frequency and ϵ is the second-order Zeeman shift. Applying a unitary transformation, U, to the Hamiltonian in Eq. (2.1), we arrive at the following effective Hamiltonian,

$$H_{\text{eff}} = UHU^{\dagger} = \begin{pmatrix} \frac{(p_x + 2\hbar k_L)^2}{2m} - \hbar\delta & \frac{\hbar\Omega}{2} & 0 \\ \frac{\hbar\Omega}{2} & \frac{p_x^2}{2m} - \hbar\epsilon & \frac{\hbar\Omega}{2} \\ 0 & \frac{\hbar\Omega}{2} & \frac{(p_x - 2\hbar k_L)^2}{2m} + \hbar\delta \end{pmatrix}, \tag{2.2}$$

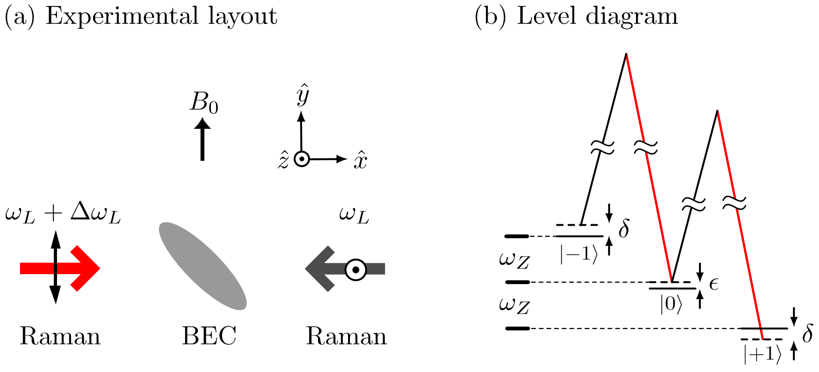

Figure 2.1.: (a)The experimental setup in Spielman's group. ω_L and $\omega_L + \Delta\omega_L$ are the two Raman laser frequencies. B_0 is the bias magnetic field to split the three hyperfine levels in Rb atoms. (b) The three F=1 hyperfine states of Rb atoms. The $|1,-1\rangle$ ($|1,0\rangle$) state is coupled to the $|1,0\rangle$ ($|1,1\rangle$) state by a two-photon transition. ω_Z is the linear Zeeman shift, δ is the detuning, and ϵ is the quadratic Zeeman shift. The figure is taken from Ref. [30].

with the unitary matrix

$$U = \begin{pmatrix} e^{-2ik_L x} & 0 & 0 \\ 0 & 1 & 0 \\ 0 & 0 & e^{2ik_L x} \end{pmatrix}. \tag{2.3}$$

Notice that the terms $\pm 2\hbar k_L$ in Eq. (2.2) come from the nontrivial commutation relation between the kinetic energy operator and the position operator in the matrix, U. After the unitary transformation, p_x in Eq. (2.2) stands for *quasi-momentum*. This term quasi-momentum is borrowed from the Bloch's theorem stating that the wave function of an electron in a periodic potential is a plane wave with quasi-momentum (or crystal momentum) as its wave vector multiplied by a periodic function with the lattice periodicity. In the absence of Raman coupling, the effective Hamiltonian represents three quadratic bands centered separately at quasi-momenta $p_x = -2\hbar k_L$, 0, and $2\hbar k_L$, see the black dashed curves in Fig. 2.2. The hyperfine spin index is not enough to label the three dressed states for each k_x now. We need to introduce another quantum number to label these three unitarily transformed states: $|-1, k_x + 2k_L\rangle$, $|0, k_x\rangle$, and $|1, k_x - 2k_L\rangle$. The Raman coupling couples these three states through two-photon transitions. Every time when the atom absorbs one photon from one laser and emits a stimulated photon into the other laser beam, it will obtain a $2k_L$ momentum kick with a spin change simultaneously.

Since the quasi-momentum is a good quantum number (in the absence of any trapping potential), diagonalizing the effective Hamiltonian in Eq. (2.2) for each $k_x = p_x/\hbar$ gives three eigenenergies, $E_i(k_x)$ for $i = 1, 2, 3$. The energy dispersion relations depend on the three experimentally tunable parameters, δ, Ω and ϵ. The parameter δ controls the overall tilting of the energy bands and the Raman coupling Ω determines the size of gaps opened at the crossing points of the bare bands. We have plotted the three energy bands with different parameters in Fig. 2.2, 2.3 and 2.4. When the parameter is appropriately chosen, the lowest band can have only one single minimum at a nonzero quasi momentum, $k_x = k_{\mathrm{min}}$, see Fig. 2.3. In the case, expanding the lowest energy dispersion around its minimum, we get the effective energy dispersion relation: $E_1(k_x) \approx \hbar^2(k_x - k_{\mathrm{min}})^2/2m^*$, where m^* is the effective mass depending on the curvature of the energy band. The effective Hamiltonian describing the lowest energy band mimics the Hamiltonian of a charged particle in a magnetic field, i.e. $H = (\vec{p} - q\vec{A})^2/2m$. We can interpret the k_{min} as the light-induced vector gauge potential with the effective charge $q = 1$.

Although the vector gauge potential created in the first experiment is constant in space and time, which corresponds to zero electric and magnetic fields, Spielman's group later has created a synthetic magnetic field [31] for neutral atoms by inducing a detuning gradient, which equivalently adds spatial dependence to the vector potential. They demonstrated the existence of vortices inside a Bose-Einstein condensate as one evidence of the artificial magnetic field. In 2011, they have also successfully generated a synthetic electric field [32] by adding time dependence to the vector potential. These experiments were all done with a similar experimental setup shown in Fig. 2.1.

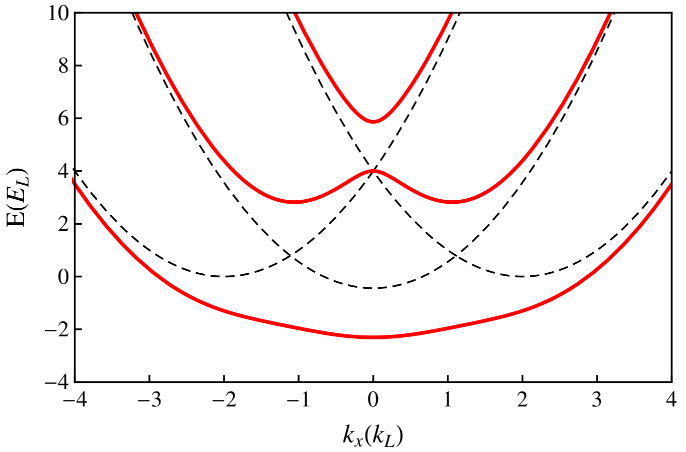

Figure 2.2.: The three effective energy dispersion relations. The red solid curves are for $\hbar\Omega = 4.85E_L$, $\hbar\epsilon = 0.44E_L$ and $\hbar\delta = 0$, where $E_L = \hbar^2 k_L^2/2m$. The black dashed curves are the bare energy dispersion curves in the absence of Raman coupling, Ω.

In 2012, Pengjun Wang *et al.* and Lawrence W. Cheuk *et al.* have realized an equal mixing of Rashba and Dresselhaus spin-orbit coupling in degenerate Fermi gases of ^{40}K [33] and of ^{6}Li respectively [34]. The unique dispersion relation was mapped out by using momentum-resolved radio-frequency spectroscopy and spin-Injection spectroscopy separately. This realization fuels many studies for spin-orbit coupled Fermi gases. From Wang's agreement between the experimental observation of the fermion population change in different energy dispersion branches and a finite temperature calculation, they expect to see a Lifshitz transition of the change in the Fermi surface topology by further cooling down the system. By further confining the system in one-dimensional geometry, they predict to see Majorana fermion modes at the phase boundaries when the Fermi surface topology changes.

2.1.1 Equal Rashba-Dresselhaus-type spin-orbit coupling

At a special parameter regime, $\epsilon \approx \delta > \Omega$, the third state will be far away from the other roughly degenerate states, the three-level system can be reduced into one

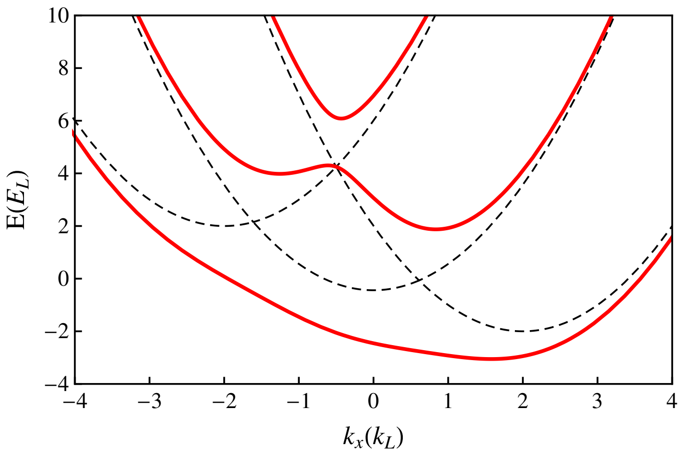

Figure 2.3.: Energy dispersions in the single minimum regime. The red solid curves are for $\hbar\Omega = 4.85E_L$, $\hbar\epsilon = 0.44E_L$ and $\hbar\delta = -2E_L$. The black dashed curves are the bare energy dispersion curves with $\Omega = 0$. The lowest energy dispersion has a single nonzero minima near $k_x \sim 2k_L$, which is the signature of the vector gauge potential.

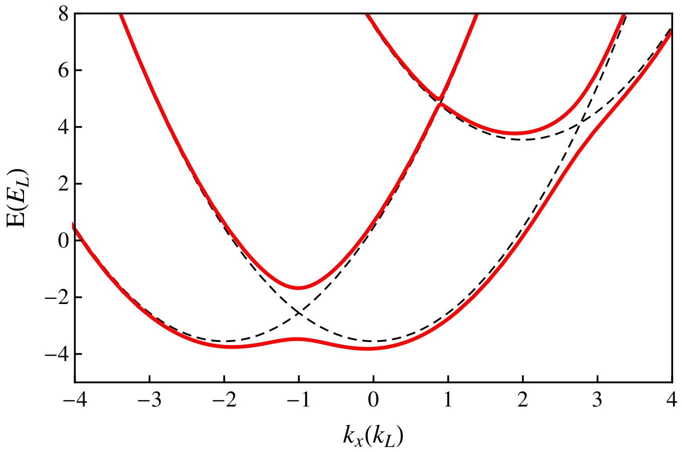

Figure 2.4.: Energy dispersion relations in the spin-orbit coupled regime. The red solid curves are for $\hbar\Omega = 1.8E_L$, $\hbar\epsilon = 3.55E_L$ and $\hbar\delta = 3.55E_L$. The black dashed curves are the bare energy dispersion curves in the absence of Raman coupling. The third state is negligible since it is far enough from the region of interest. The two effective energy bands in the lower-energy regime capture the spin-orbit coupling for an effective spin-$\frac{1}{2}$ system.

effective spin-1/2 system with the characteristic double-minimum energy dispersions, see Fig. 2.4, which is captured by the following Hamiltonian,

$$H_{\text{eff}} = \begin{pmatrix} \frac{(p_x+\hbar k_L)^2}{2m} - \frac{\hbar\delta}{2} & \frac{\hbar\Omega}{2} \\ \frac{\hbar\Omega}{2} & \frac{(p_x-\hbar k_L)^2}{2m} + \frac{\hbar\delta}{2} \end{pmatrix}, \tag{2.4}$$

$$= \frac{\hbar^2 k_x^2}{2m} I_{2\times 2} + \frac{\hbar^2 k_L k_x}{m}\sigma_z + \frac{\hbar\Omega}{2}\sigma_x - \frac{\hbar\delta}{2}\sigma_z, \tag{2.5}$$

where $\sigma_{x,y,z}$ are the Pauli matrices and $I_{2\times 2}$ is the identity matrix. Rewriting Eq.(2.4) in terms of Pauli matrices, a whole new interpretation of this Hamiltonian in Eq. (2.5) is achieved. The second term states that the particle's spin is linked to its *linear* momentum, which is the famous spin-orbit coupling. In solids, the Rashba spin-orbit coupling shows up due to inversion symmetry breaking. An intuitive way to understand the Rashba spin-orbit coupling is to imagine an electron moving with a velocity, $\vec{v}$, in an electric field, $\vec{E}$, which causes the inversion symmetry breaking. The electron will experience a velocity-dependent magnetic field in its rest frame,

$$\vec{B} = \gamma \vec{v} \times \vec{E}/c^2, \tag{2.6}$$

where c is the speed of light and $\gamma = 1/\sqrt{1 - v^2/c^2} \approx 1$. The electron's spin will couple to this magnetic field and lead to the spin-dependent Hamiltonian,

$$H_{\text{SOC}} = \frac{\mu_B}{2c^2}\vec{v} \times \vec{E} \cdot \vec{\sigma}, \tag{2.7}$$

where $\vec{\mu}_e = -g\mu_B\vec{\sigma}/2 = -\mu_B\vec{\sigma}$ is the electron's magnetic moment. The 1/2 factor is the Thomas correction. If the electric field is pointing in the z direction, the Rashba spin-orbit term can be expressed as $H_{\text{SOC}} = \alpha(\vec{\sigma} \times \vec{p}) \cdot \hat{z} = \alpha(\sigma_x p_y - \sigma_y p_x)$ with $\alpha = \mu_B E/2mc^2$. A similar type interaction, Dresselhaus spin-orbit coupling, apears in systems with lack of an inversion center. The Dresselhaus spin-orbit coupling is often written as $H_{\text{D}} = \beta(\sigma_x p_x - \sigma_y p_y)$. Up to a spin rotation, $H_{\text{SOC}} = \alpha(\sigma_x p_x + \sigma_y p_y)$. It is clear to see that the effective spin-orbit Hamiltonian generated in Eq. (2.5) is an equal mixing of Rashba and Dresselhaus spin-orbit coupling.

The spin-orbit coupling has a unique energy dispersion. The Mexican-hat like energy dispersion relation in spin-orbit coupled BECs brings *an extra ground state*

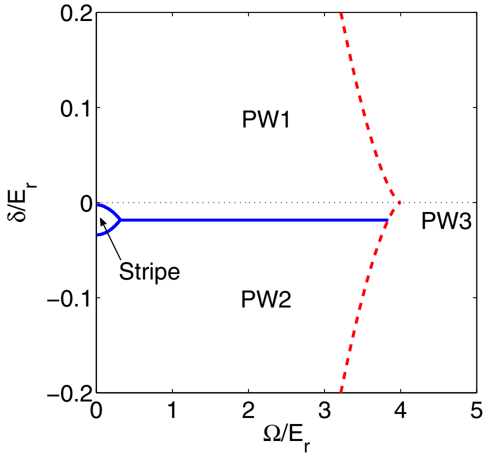

Figure 2.5.: Zero temperature mean-field phase diagram for pseudo-spin $\frac{1}{2}$ of ^{87}Rb (for m_F=0 and -1 in F=1). This figure is taken from Ref. [37].

degeneracy. This ground state degeneracy enriches the phase diagram. Minimization of the energy functional with variational wave function gives the mean-field phase diagram at zero temperature for pseudo-spin $\frac{1}{2}$, $\{F = 1, m_F = 0, -1\}$, of ^{87}Rb, [35][36][37]. The nontrivial stripe phase appears due to the interference of two characteristic momenta when the ground state is degenerate or nearly degenerate. When detuning is large enough, the condensate will fall into either the right or left well, leading to the plane wave phases (PW1 and PW2), see Fig. 2.5. When Raman coupling is large, the energy dispersion is modified to have one energy minimum, so BECs show again a plane wave phase with a different momentum (PW3). Experimentally, it is challenging to reach a high-resolution *in-situ* image to observe the spatial oscillation of the stripe phase with length scale $1/k_L$, where k_L is the laser wave vector. However, the finite-temperature phase diagram is mapped out statically by measuring magnetization many times for points in the parameter space. A finite temperature transition from a stripe phase to a magnetized phase is seen [38].

Not only are the static properties of spin-orbit coupled BECs intriguing, but so also are their collective excitations. The collective dipole oscillation frequency of spin-orbit coupled BECs inside a harmonic trap has been measured to deviate from the trap frequency, which is the case for regular BECs. The SOC-modified frequency is explained well by the effective mass theory [39]. A companion of dipole oscillation in SO-coupled condensates is the magnetization oscillation. It originates from *the absence of Galilean invariance*. In a conventional BEC, the extra term vk_x from the moving a BEC with velocity v along x direction can be gauged away ($\psi \to e^{imvx}\psi$). However, this gauge transformation cannot be gauged away, and would create a Zeeman-energy-like term, $-mvk_L\sigma_z$, in systems without Galilean invariance, such as the SO-coupled BEC. The dynamical oscillations are used as a powerful tool to measure static physical quantities like the spin susceptibility. A quantum phase transition from the magnetic phase to the nonmagnetic one has been observed with the measurement of susceptibility. The lack of Galilean invariance also causes a richer superfluid critical velocity behavior in SO-coupled superfluids [37].

The use of SO-coupled BECs to simulate dynamics of relativistic particles subject to the Dirac equation has been reported [40] [41]. The force-free trembling motion, named as *Zitterbewegung* (ZB), of relativistic electrons has been predicted but almost impossible to be observed due to the large value of light speed. In spin-orbit coupled BECs, the simulated light speed is 10^{10} smaller, so the oscillating amplitude is 10^6 times bigger and make the measurements possible. The spin-momentum locking feature, which causes the simultaneous oscillations in position and velocity accompanying the spin oscillation has been observed and distinguishes ZB from the usual Rabi oscillation.

Due to the *simplicity* of the NIST experiments, the publication on equal Rashba and Dresselhaus (RD) type spin-orbit coupled BECs has soared after its first realization [27]. However, the ongoing research is not only confined on the RD-type spin-orbit coupling. Many papers discuss also about the stereotype of spin-orbit coupling (SOC) in solid-state systems, which is the Rashba SOC. A three-dimensional version of Rashba SOC, the Weyl spin-orbit coupling, is widely discussed in the literature too. However, the last two are limited to theoretical discussions in the current stage.

2.2 Trap-driven dynamics in spin-orbit coupled BECs

To study dynamics of SO-coupled BECs inside a harmonic trap, two different limits can be taken. One is when the Raman coupling, or the energy separation between the two adiabatic energy levels, dominates the behavior of BECs. This happens in a shorter time scale when $t \ll 1/\omega_x$ (ω_x is the trap frequency) since the trapping frequency is taken to be much smaller than the Raman coupling. The effect of the harmonic trap appears in the longer time-scale dynamics. In this limit, the dynamics is governed by the trapping potential. It acts like the kinetic energy in momentum space and controls the motions of BECs. In this section, we will focus on the dynamics induced by the trap, assuming the interatomic interaction is negligible.

2.2.1 Landau-Zener model

The spin-orbit coupled BEC in a harmonic trap can be described by the following Hamiltonian,

$$\begin{aligned} H &= H_{\mathrm{SO}} + V_{\mathrm{trap}} \\ &= \begin{pmatrix} \frac{(\vec{p}+p_L\hat{x})^2}{2m} - \frac{\hbar\delta}{2} & \frac{\hbar\Omega}{2} \\ \frac{\hbar\Omega}{2} & \frac{(\vec{p}-p_L\hat{x})^2}{2m} + \frac{\hbar\delta}{2} \end{pmatrix} + \frac{1}{2}m\omega_x^2x^2 + \frac{1}{2}m\omega_y^2y^2 + \frac{1}{2}m\omega_z^2z^2 \end{aligned} \tag{2.8}$$

where $\omega_{x,y,z}$ are the trapping frequencies. Since the spin-orbit coupling lies in the x direction only, we consider here only the dynamics along the x direction. The motions in the y and z direction are the ground state of the simple harmonic oscillators. Unless we introduce the interatomic interaction, the motion in the x direction is decoupled from those in the y and z directions. Therefore, the simplification in the spin-orbit coupled direction is justified.

$$H = H_{\mathrm{SO}} + V_{\mathrm{trap}} = \begin{pmatrix} \frac{(p_x+p_L)^2}{2m} - \frac{\hbar\delta}{2} & \frac{\hbar\Omega}{2} \\ \frac{\hbar\Omega}{2} & \frac{(p_x-p_L)^2}{2m} + \frac{\hbar\delta}{2} \end{pmatrix} + \frac{1}{2} m\omega_x^2 x^2 \tag{2.9}$$

$$= \begin{pmatrix} \frac{(p_x+p_L)^2}{2m} - \frac{\hbar\delta}{2} & \frac{\hbar\Omega}{2} \\ \frac{\hbar\Omega}{2} & \frac{(p_x-p_L)^2}{2m} + \frac{\hbar\delta}{2} \end{pmatrix} - \frac{\hbar^2}{2} m\omega_x^2 \frac{\partial^2}{\partial {p_x}^2}, \tag{2.10}$$

As we have pointed out, the Raman coupling strength, Ω, determines the gap at zero quasi-momentum between the two adiabatic energy bands, causing an *avoided crossing*. The trapping frequency in experiments is usually much smaller than the intrinsic energy scale (i.e. the energy difference between two adiabatic energy bands) of the spinor BEC, so the trap will drive the BEC in an adiabatic way if it is excited dynamically. Therefore, it is natural to rewrite the Hamiltonian in momentum space as in Eq. (2.10). At $\Omega = 0$, the original kinetic energy term becomes the potential term in momentum space and the harmonic trap behaves like the kinetic energy operator, causing the quasi-momentum of the BEC to change adiabatically. However, the adiabaticity could be shaken if there exist nontrivial avoided crossings created by diabatic coupling terms in the Hamiltonian, such as the Raman coupling here. The non-adiabaticity induced by the trap is the focus of this section. In general, studies of the non-adiabatic dynamics in a many-body system is highly-challenging. Controllable BECs indeed serve as a very good system to investigate the non-adiabatic dynamics. The adiabatic to non-adiabatic transition when the system is driven across the avoided crossing reminds us of the celebrated Landau-Zener model.

The Landau-Zener model is a classic model capturing the transition dynamics in a quantum two-level system with a level energy separation linearly-varying in time. The Landau-Zener formula is derived under certain assumptions to quantity the probability for such a two-level system to start in the ground state at $t \to -\infty$ and end in the higher energy state at $t \to \infty$ after passing through the avoided crossing or vice versa. Although the formula is named after Landau and Zener, this formula was actually derived separately by Landau, Zener, Stueckelberg and Majorana in 1932

[42][43][44][45]. Later, there have been some generalizations to multi-state systems, which are called multi-state Landau-Zener models. Demkov and Osherov have solved a system of a series of parallel levels with one additional level intersecting all the others [46]. The N-level Landau-Zener-type bow-tie model, in which N linear time-dependent diabatic levels cross at the same point in time, and only one selected state in them are coupled with the rest $(N-1)$ states, are analytically solved too[47] [48].

Following Zener's notation, the Landau-Zener Hamiltonian is written as

$$H\begin{pmatrix}\phi_1\\ \phi_2\end{pmatrix}=\begin{pmatrix}\epsilon_1 & \epsilon_{12}\\ \epsilon_{12} & \epsilon_2\end{pmatrix}\begin{pmatrix}\phi_1\\ \phi_2\end{pmatrix}, \tag{2.11}$$

where $\{\phi_1,\phi_2\}$ are the two *diabatic* states, which are time-independent. Several assumptions are made by Zener to derive the final simple expression of transition probabilities. They are separately:

(i) The energy separation between these two levels is linear in time near the crossing point: $\epsilon_1-\epsilon_2=\hbar\alpha t$.

(ii) The coupling between these two diabatic states is time-independent: $\frac{d\epsilon_{12}}{dt}=0$.

(iii) The crossing velocity is estimated by the semi-classical formula: $v=\frac{R-R_0}{t}$, where R_0 is the adiabatic coordinate of the avoided crossing. See Fig. 2.6 (a)(b). Under these three assumptions, we can show that the non-adiabatic transition probability is given by

$$P_{\text{na}}=e^{-2\pi\gamma}, \tag{2.12}$$

with $\gamma=\epsilon_{12}^2/\alpha$. In most cases, the energy levels are not explicitly proportional to time. Instead, there is a adiabatic coordinate, which is going to vary with time when couplings between these adiabatic states are taken into consideration. In systems with timescale separations, we can separate the dynamics of the system into fast and slow dynamics, where the slow dynamics does not change with time dramatically and the slow physical parameter charactering the slow dynamics is the adiabatic coordinate. This concept is well illustrated by the Born-Oppenheimer approximation, where the fast dynamics is that of electrons and the slow one is the nuclear dynamics. Thus, to apply the Landau-Zener formula in Eq. (2.12), we need to determine the α value

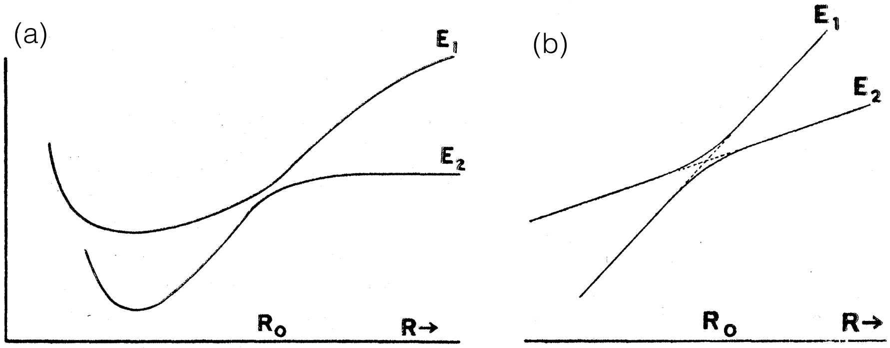

Figure 2.6.: (a) The realistic energy levels with avoided crossing drawn by Zener. R is the adiabatic parameter. R_0 locates the position of the avoided crossing. (b) The ideal two energy levels, which are varying linear in time. These figures are taken from Ref. [43].

for it. Applying the model to our spin-orbit coupled case, we first map our physical quantities to the Landau-Zener model, see Table 2.1.

$$\begin{aligned} i\hbar\frac{\partial}{\partial t}\begin{pmatrix}\phi_1\\ \phi_2\end{pmatrix} &= i\hbar\frac{\partial}{\partial k_x}\frac{\partial k_x}{\partial t}\begin{pmatrix}\phi_1\\ \phi_2\end{pmatrix} = i\hbar v\frac{\partial}{\partial k_x}\begin{pmatrix}\phi_1\\ \phi_2\end{pmatrix} && (2.13)\\ &= \begin{pmatrix}\frac{\hbar^2}{2m}(k_x+k_L)^2-\frac{\hbar\delta}{2} & \frac{\hbar\Omega}{2}\\ \frac{\hbar\Omega}{2} & \frac{\hbar^2}{2m}(k_x-k_L)^2+\frac{\hbar\delta}{2}\end{pmatrix}\begin{pmatrix}\phi_1\\ \phi_2\end{pmatrix} && (2.14)\\ &\approx \begin{pmatrix}\alpha_1(k_x-k_{\mathrm{cr}})+\epsilon_{\mathrm{cr}} & \frac{\hbar\Omega}{2}\\ \frac{\hbar\Omega}{2} & \alpha_2(k_x-k_{\mathrm{cr}})+\epsilon_{\mathrm{cr}}\end{pmatrix}\begin{pmatrix}\phi_1\\ \phi_2\end{pmatrix}, && (2.15)\end{aligned}$$

where velocity $v \equiv \frac{\partial k_x}{\partial t}$, k_{cr} is the quasi-momentum of the diabatic level crossing point, and ϵ_{cr} is the energy at that point. The last equality holds when k_x is near k_{cr}. Comparing Eq. (2.15) to Eq. (2.11), we find the mapping $(\alpha_1-\alpha_2)/v=\alpha$ and $\Omega/(2v)=\epsilon_{12}$. Linearization near the crossing point gives the parameters of α_1 and α_2. As for the velocity, we estimate it in a classical way: $v=\sqrt{2(E-u(k_{\mathrm{cr}}))/m_{\mathrm{eff}}}$, where $m_{\text{eff}} = \frac{1}{m\omega_x^2}$ and $u(k_{\text{cr}})$ is the adiabatic potential energy at crossing point, see Fig. (2.7). Finally, the non-adiabatic transition probability is found to be

$$P_{\text{na}} = e^{-2\pi(\frac{\Omega}{2v})^2/|\frac{\alpha_1-\alpha_2}{v}|}. \tag{2.16}$$

It is clear to see that when the velocity $v \to 0$, the non-adiabatic probability $P_{\text{na}} \sim 0$. We return back to the prediction given by the adiabatic theorem, which states that an infinitely-slow change in some parameter of a system will leave more than enough time for the system to adapt itself very well to its instantaneous eigenstates.

	Real space	Momentum space
Adiabatic parameter	x	k_x
Effective mass	m	$\frac{1}{m\omega_x^2}$
Velocity	$\frac{dx}{dt}$	$\frac{dk_x}{dt}$
Kinetic energy	$-\frac{1}{2m_x}\frac{\partial^2}{\partial x^2}$	$-\frac{1}{2m_{\text{eff}}}\frac{\partial^2}{\partial k_x^2}$

Table 2.1: Transformation of physical quantities between coordinate space and momentum space.

2.2.2 Validity of Landau-Zener model

Reading the Landau-Zener parameter, α defined in the assumption (i) below Eq. (2.11), from adiabatic potentials is sometimes ambiguous. It is not clear to what extent the model will still approximate a real avoided crossing accurately we encounter. One method developed by Clark [49] is illustrated with our example in the following.

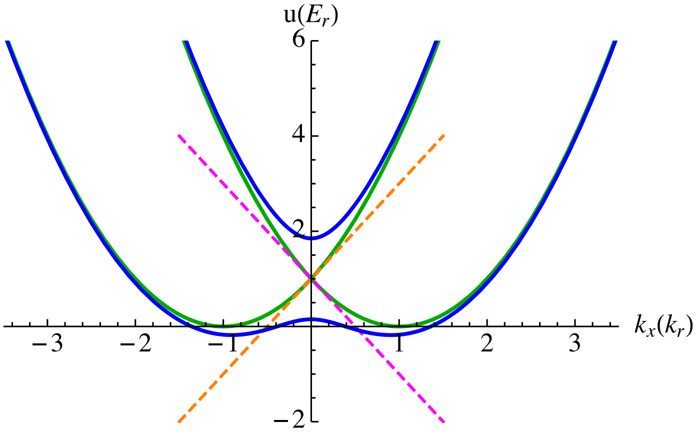

Figure 2.7.: Linearization near the crossing point ($k_{\mathrm{cr}} = 0$) of the two energy bands with $\Omega = 0$ (in green). The blue curves show the adiabatic energy potential curves with $\Omega = 1.7E_L$. Zero detuning ($\delta = 0$) are used in both blue and green curves.

Definition of P and Q matrices

Diagonalizing the spin-orbit Hamiltonian, we get the adiabatic potentials, $u_1(k_x)$ and $u_2(k_x)$, and adiabatic eigenstates, $|\chi_1\rangle$ and $|\chi_2\rangle$. They both depend on k_x *parametrically*. The adiabatic eigenstates are

$$|\chi_1(k_x)\rangle = \begin{pmatrix} \cos\theta(k_x) \\ \sin\theta(k_x) \end{pmatrix}, \tag{2.17}$$

$$|\chi_2(k_x)\rangle = \begin{pmatrix} \sin\theta(k_x) \\ -\cos\theta(k_x) \end{pmatrix}, \tag{2.18}$$

where

$$\tan\theta(k_x) = \frac{\hbar\Omega}{2\hbar^2 k_L k_x/m - \hbar\delta - \sqrt{(2\hbar^2 k_L k_x/m - \hbar\delta)^2 + \hbar^2\Omega^2}}. \tag{2.19}$$

The corresponding energies respectively are

$$u_{1/2}(k_x) = \frac{\hbar^2}{2m}(k_x^2 + k_L^2) \mp \frac{1}{2}\sqrt{(2\hbar^2 k_x k_L/m - \hbar\delta)^2 + \hbar^2\Omega^2}. \tag{2.20}$$

Using the complete eigenbasis, we expand the wave function of the total Hamiltonian in Eq. (2.10) as

$$\Psi(k_x) = \sum_{i=1,2} f_i(k_x)|\chi_i\rangle. \tag{2.21}$$

Inserting Eq.(2.21) into the time-independent Schrödinger equation, we get

$$-\frac{\hbar^2}{2}m\omega_x^2\frac{\partial^2}{\partial k_x^2}f_i + (u_i - E)f_i + \frac{\hbar^2}{2}m\omega_x^2\sum_{j=1,2}\left(\langle\chi_i|\frac{\partial^2}{\partial k_x^2}|\chi_j\rangle f_j + 2\langle\chi_i|\frac{\partial}{\partial k_x}|\chi_j\rangle\frac{\partial}{\partial k_x}f_i\right) = 0, \tag{2.22}$$

for $i = 1, 2$. The P matrix is defined as $P_{ij} = \langle\chi_i|\frac{\partial}{\partial k_x}|\chi_j\rangle$ and the Q matrix as $Q_{ij} = \langle\chi_i|\frac{\partial^2}{\partial k_x^2}|\chi_j\rangle$. It can be shown that the P matrix is an anti-symmetric matrix with no diagonal matrix elements.

The adiabatic formalism based on the spirit of the Born-Oppenheimer approximation introduced above has wide applications. We will come back to it in later chapter when we introduce the hyperspherical coordinate to solve few-body scattering/bound state problems. The adiabatic parameter there is an useful physical quantity for charactering the system size.

The message hidden in the P matrix

We have mentioned in subsection 2.2.1 that the linearization of the Hamiltonian around the crossing point will help us determine the coefficient α when calculating the Landau-Zener probability, P_{na}. In fact, we don't have to do that to find the P_{na}. The information can actually be extracted from the P matrix that we already defined in the last sub-subsection.

The Hamiltonian in Eq. (2.11) can be recast into the adiabatic form. Diagonalizing the Hamiltonian in Eq. (2.11) at fixed t, we get $H(t)\phi_\pm(t) = \epsilon_\pm(t)\phi_\pm(t)$, where the eigenstates $\phi_\pm$ are

$$\phi_- = \cos\theta\phi_1 + \sin\theta\phi_2, \tag{2.23}$$

$$\phi_+ = \sin\theta\phi_1 - \cos\theta\phi_2, \tag{2.24}$$

and the eigenenergies $\epsilon_\pm$ are

$$\epsilon_\pm = \frac{1}{2}(\epsilon_1+\epsilon_2) \pm [\frac{1}{4}(\epsilon_1-\epsilon_2)^2+\epsilon_{12}^2]^{1/2} \tag{2.25}$$

with $\cot\theta = [(\epsilon_1-\epsilon_2)/2-\sqrt{\epsilon_{12}^2+(\epsilon_1-\epsilon_2)^2/4}]/\epsilon_{12}$. The off-diagonal term of P matrix can be derived as

$$\begin{aligned} P_{12} = -P_{21} = \langle\phi_-|\frac{d}{dt}|\phi_+\rangle &= \frac{\langle\phi_-|\frac{dH}{dt}|\phi_+\rangle}{\epsilon_+-\epsilon_-} = \frac{\alpha\sin\theta\cos\theta}{\epsilon_+-\epsilon_-} = \frac{(\alpha/2)\sin 2\theta}{\epsilon_+-\epsilon_-} \\ &= \frac{\alpha\tan\theta/(1+\tan^2\theta)}{\epsilon_+-\epsilon_-} = \alpha\frac{\epsilon_{12}/\sqrt{4\epsilon_{12}^2+(\epsilon_1-\epsilon_2)^2}}{[(\epsilon_1-\epsilon_2)^2+4\epsilon_{12}^2]^{1/2}} = \frac{\alpha\epsilon_{12}}{4\epsilon_{12}^2+(\epsilon_1-\epsilon_2)^2} \\ &= \frac{\alpha\epsilon_{12}}{4\epsilon_{12}^2+\alpha^2t^2} = \frac{1/2(\alpha/\Delta)}{1+(\alpha/\Delta)^2t^2}, \end{aligned} \tag{2.26}$$

where $\Delta = 2\epsilon_{12}$ is the minimum energy difference between these two adiabatic bands. From the above derivation, we see that P_{12} depends only on the ratio of α/Δ, and has a Lorentzian shape in the parameter t. This is a good check to see if the Landau-Zener model can be applied in our case. Also, we find that the full width of P_{12} at half maximum (FWHM) is equal to the inverse of its maximum height, that is, FWHM$= 2/(\alpha/\Delta) = |P_{12,\max}|^{-1} = (\alpha/(2\Delta))^{-1}$. In most cases, we can calculate the P matrix analytically, so it is a simple task to find out the parameter α/Δ simply from finding the maximum value of $|P_{12}|$. Making use of this advantage, we rewrite the non-adiabatic transition probability in this way,

$$P_{LZ} = e^{-2\pi\gamma}, \tag{2.27}$$

with $\gamma = \epsilon_{12}^2/\alpha = (\Delta/2)^2/\alpha = (\Delta/4)/(\alpha/\Delta) = (\Delta/8)|P_{12,\max}|^{-1}$. Mapping to our case,

$$\gamma = (\frac{\epsilon_{12}}{v})^2/(\frac{\alpha}{v}) = (1/v)\epsilon_{12}^2/\alpha = (1/v)(\Delta/8)|P_{12,\max}|^{-1}, \tag{2.28}$$

where Δ is the minimum separation between the two adiabatic SO-coupled bands (u_1 and u_2 in Eq. (2.20)) and $P_{12,\max}$ is the maximum value (in magnitude) of the matrix element $P_{12} = \langle\chi_1|\partial_{k_x}|\chi_2\rangle$. We have verified the validity of the Landau-Zener model in our system in Fig. (2.8). The P matrix represents a perfect Lorentzian shape distribution.

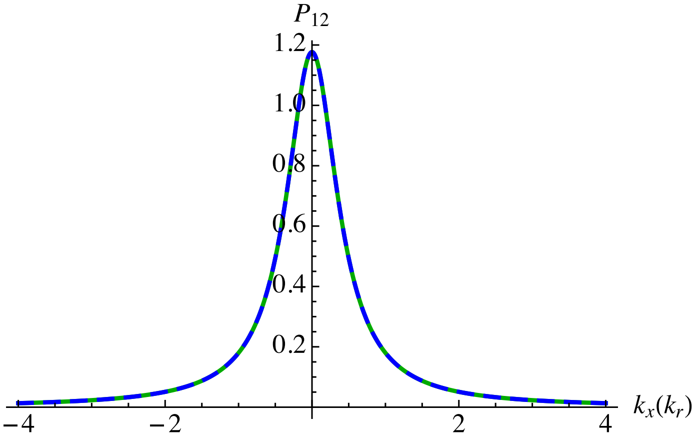

Figure 2.8.: The off-diagonal term, P_{12}, in the P matrix is drawn in green. The blue dashed curve on top of the green curve is a Lorentzian fit to the P_{12} curve. The fitting parameter is $\alpha/\Delta = 2.35$. Parameters used for the P matrix are $\Omega = 1.7E_L$ and $\delta = 0E_L$.

2.2.3 Direct numerical simulation: Chebychev propagation method

Within the mean-field theory, Bose-Einstein condensates can be described well by the Gross-Pitaevskii equation, also known as the non-linear Schrödinger equation based on the assumption that the all the atoms in the condensate occupy the same orbital state and interact through the zero-range potential.

$$i\hbar\frac{\partial}{\partial t}\Psi(\vec{r},t) = \Bigg(-\frac{\hbar^2\nabla^2}{2m} + V(\vec{r}) + U_0|\Psi(\vec{r},t)|^2\Bigg)\Psi(\vec{r},t), \tag{2.29}$$

where $V(\vec{r})$ is any single-particle potential and the non-linear term, $U_0|\Psi|^2$, accounts for the inter-particle interaction. In our discussion below, we disregard the interatomic interaction, and emphasize the effect induced by trap.

To solve the one-dimensional time-dependent Schrödinger equation for the trapped spin-orbit coupled BEC, we apply the Chebychev propagation method [50].

$$i\hbar\dot{\Psi}(q,t) = \hat{H}\Psi(q,t) = \left[-\frac{1}{2}m\omega_y^2\frac{\partial^2}{\partial q^2} + \begin{pmatrix} \frac{\hbar^2}{2m}(q+k_r)^2 - \frac{\delta}{2} & \frac{\Omega_R}{2} \\ \frac{\Omega_R}{2} & \frac{\hbar^2}{2m}(q-k_r)^2 + \frac{\delta}{2} \end{pmatrix}\right]\Psi(q,t), \tag{2.30}$$

where $\Psi(q,t) = \{\Psi_\uparrow(q,t), \Psi_\downarrow(q,t)\}^T$ is a two-component column vector written in the bare state basis ($\{|m_F = 0\rangle, |m_F = -1\rangle\}$). Notice that in this and the following subsections, we will adopt the same notation as we use in [28]. The recoil momentum, $k_r = 2\pi/\lambda$, and the recoil energy, $E_r = \frac{\hbar^2 k_r^2}{2m}$, are used. The counter-propagating setup ensures the equivalence of the recoil momentum, k_r, and the laser wave vector, k_L. We will sometimes use them interchangeably. In general, they are not equal if the laser beams are aligned with a angle. Also the $\hbar\Omega/\hbar\delta$ are replaced by Ω_R/δ with the unit of energy. Expanding the evolution operator, $\hat{U}$, in terms of the Chebychev polynomials with a renormalization of the Hamiltonian H whose eigenvalue ranges from $[\lambda_{\min}, \lambda_{\max}]$, we arrive at

$$\hat{U}(dt) = e^{-i\hat{H}dt/\hbar} = \sum_{n=0}^{\infty} a_n \phi_n(-i\hat{H}_{\text{norm}}) = \sum_{n=0}^{\infty} a_n \phi_n\left(\frac{-i\hat{H} + i(\lambda_{\max} + \lambda_{\min})/2}{(\lambda_{\max} - \lambda_{\min})/2}\right), \tag{2.31}$$

where $\phi_n(x)$ is the complex Chebychev polynomial of order n. The expansion coefficients are

$$a_n = e^{i(\lambda_{\max}+\lambda_{\min})dt/2\hbar} C_n J_n\left(\frac{(\lambda_{\max} - \lambda_{\min})dt}{2\hbar}\right), \tag{2.32}$$

with $C_0 = 1$ and $C_{n\neq 0} = 2$. $J_n(x)$ is the Bessel function of order n. We obtain the wave function at any time by applying the evolution operator to an given initial wave function: $\Psi(q, dt) = \hat{U}(dt)\Psi(q, t = 0)$. To perform the Hamiltonian operation, we represent our wave functions and operators in the Fourier discrete variable representation (Fourier-DVR) [51]. We have chosen equally-spaced grids in our calculations, for instance, for $q \in [q_{\min}, q_{\max}]$, $q_i = q_{\min} + i(q_{\max} - q_{\min})/(N + 1)$ for $i = 1, 2, ..., N$. We have taken $\{q_{\min}, q_{\max}\} = \{-6k_R, 6k_R\}$, and $N = 500$. To converge the series expansion, we require the degree of the expansion in Eq. (2.31) to be larger than $R = (\lambda_{\max} - \lambda_{\min})dt/2\hbar$. In our simulation, we choose the degree to be the least integer greater than or equal to $1.5R$. Since the parameter R depends on dt, the efficiency can be greatly improved by appropriately choosing a suitable time step ($dt = 0.01\hbar/E_R$) for each time propagation.

To best describe what happens in experiments, in our simulations, we use a Gaussian wave packet with its width derived from experiments as our initial wave function. The initial state is prepared in one of the adiabatic states. Note that the adiabatic states ($\{|+\rangle, |-\rangle\}$) are related to the bare states by a unitary transformation and if the initial wave function is far away from the avoided crossing, the adiabatic states are basically the uncoupled bare states. With Chebychev propagation method, we can evolve our system to any later time to study non-adiabatic inter-band transitions. Defining the probability for a BEC to stay in $|\pm\rangle$ as

$$P_{\pm}(t) = \sum_{i=1}^{N} |\Psi_{\pm}(q_i, t)|^2, \tag{2.33}$$

we extract the asymptotic values of the probability for the atom to be in the other adiabatic state after the wave packet passes the avoided crossing. This defines the non-adiabatic transition probability.

We have simulated Landau-Zener probabilities as a function of the Raman coupling strength for several different crossing velocities, see Fig. 2.9. The result indeed shows that the simple LZ formula gives a very good approximation to the non-adiabatic inter-band transition probability in spin-orbit coupled BECs for the parameter space we have investigated.

2.2.4 Experimental confirmation

Tunable Landau-Zener transitions have been observed experimentally in a spin-orbit coupled BEC [28] by Olson *et al.*. They have used a configuration to generate an equal Rashba and Dresselhaus spin-orbit coupling in ^{87}Rb BEC which is similar to the NIST scheme, see Fig. 2.10 (a) and (b). One minor difference is that the laser beams are counter-propagating in the y direction, so the 1D spin-orbit coupling is along the y direction.

The non-adiabatic dynamics through the avoided crossing gapped by the Raman coupling is studied. Two different driving sources are used to study the non-adiabatic transition in SO-coupled BECs due to the non-commutativity of momentum and its

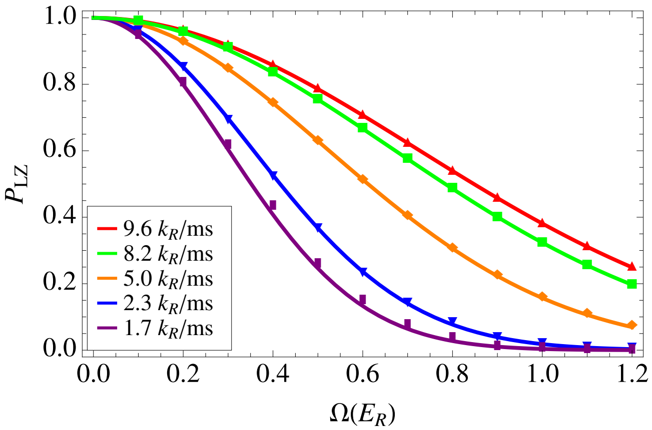

Figure 2.9.: Comparison of the exact numerical solution with Chebychev propagation method (shaped symbols) and the Landau-Zener formula (solid curves) for the non-adiabatic transition probability as a function of the Raman coupling Ω_R . Different colors correspond to different velocities at the crossing point. Taken from Ref. [28].

canonical conjugate. One uses the harmonic trap, $H_{\rm trap} = -\frac{m\omega_y^2}{2}\frac{d^2}{dq^2}$, and the other uses gravity, $img\frac{d}{dq}$, as is indicated on Fig. 2.10(c). Measurements of the Landau-Zener transition probability, $P_{\rm LZ}$, were performed by first preparing the BEC in either the upper or lower SO energy level, then driving the BEC across the avoided crossing, and when the BEC was sufficiently far from the crossing, absorption images after time-of-flight were taken to determine the bare spin population so the $P_{\rm LZ}$.

The dependence of non-adiabatic transition probabilities on Raman coupling, Ω_R, on the difference in the slope of linear energy bands near the crossing, and on the crossing velocity are carefully measured and independently tested, see Fig. 2.11. A bigger Raman coupling strength causes a wider energy separation between the adiabatic energy bands, so a smaller transition probability. Calculations have shown that when $\Omega_R \geqslant 1.2E_R$, the non-adiabatic transition probability is negligible, so we have chosen Ω_R from 0 E_R up to $1.2E_R$. The dependence on velocity confirms the adiabatic limit in the zero velocity limit, while it becomes fully diabatic when $v \gg 1k_R/ms$. For fixed Raman coupling, the difference in the slope of the energy bands is shown to be independent of detuning. The insensitivity of P_{LZ} to detuning is verified too. All the measurements have shown good quantitative agreement with the predictions provided by the Landau-Zener model in Subsection 2.2.1 and direct numerical simulations in Subsection 2.2.3. Possible applications on spin-dependent atomtronic transistors are pointed out. In there, the Raman coupling acts as the gate voltage, the BEC spin polarization acts as the current, and the "drift velocity" is induced by the force that acts as the source-drain voltage. A Stern-Gerlach field is then used in the readout.

λ	k_r	E_r	$\frac{\omega_x}{2\pi}$	$\frac{\omega_y}{2\pi}$	$\frac{\omega_z}{2\pi}$
782.26 nm	$\frac{2\pi}{\lambda}$	$2\pi\hbar$ 3.75 kHz	50-90 Hz	180-450 Hz	180-450 Hz

Table 2.2: Relevant energy scales in experiments.

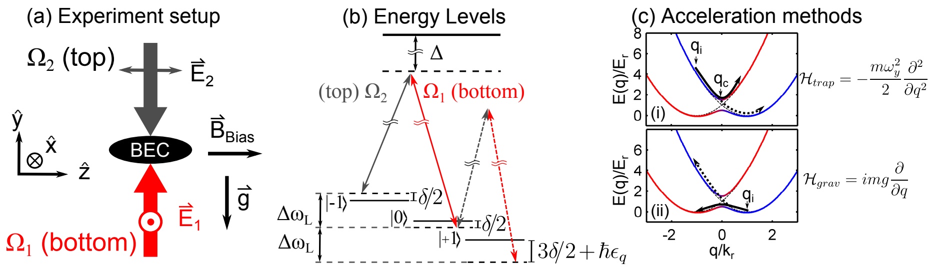

Figure 2.10.: (a) Experimental setup in Chen's group at Purdue. This is very similar to Spielman's setup. However, the spin-orbit coupling is in y direction, instead of x. (b) Three Zeeman-split F=1 levels of Rb atoms coupled by two-photon Raman transitions. (c) Two driving mechanism used to study Landau-Zener transitions: (i) the acceleration induced by the trapping potential drives transitions from the upper to lower dressed eigenlevel, and (ii) the acceleration induced by the gravitational force drives transitions from the lower to upper dressed eigenlevel. Notice that the gravity is along $-y$ direction. This figure is taken from Ref.[28].

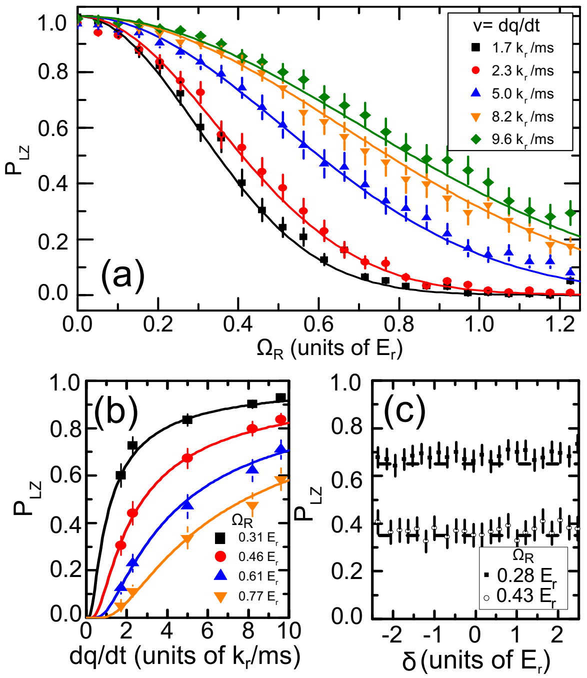

Figure 2.11.: The Landau-Zener transition probability as a function of (a) Raman coupling (b) velocity (c) detuning. This figure is taken from Ref.[28].

2.2.5 Breakdown of the Landau-Zener model in spin-orbit coupled BECs

In the energy regime under discussion so far, where the initial kinetic energy of the condensate is larger than the Raman coupling, Ω, the dynamics in momentum space can be well described by the Landau-Zener model. In another limit, where the coupling is stronger than the initial kinetic energy of the condensate, Bo Xiong *et al.* [29] have pointed out that the multichannel interference effect should be considered to describe the non-adiabatic dynamics in spin-orbit coupled BECs. The deviation from the standard Landau-Zener is found to be around 10%, see Fig. 2.12.

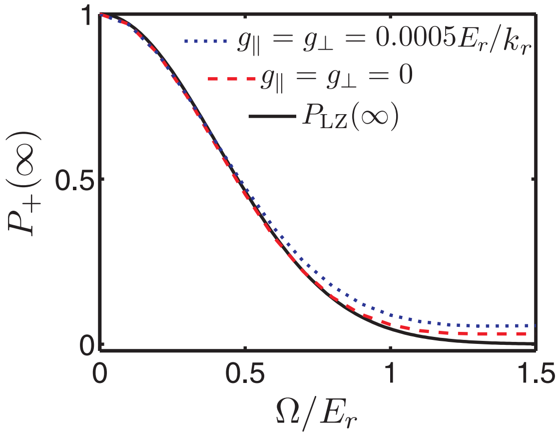

Figure 2.12.: The non-adiabatic transition probabilities calculated from different models. The black curve is from the Landau-Zener formula. The red dashed and blue dotted curves are the full numerical simulations without and with interaction. This figure is taken from Ref. [29].

The multichannel interference comes from the finite momentum distribution of BECs. The momentum-dependent dressed states cause the Rabi frequency to carry momentum dependence as well. This dependence gives the Fresnel interference pattern in the momentum space wave functions and causes a universal oscillating power-law decay in the longer time scale.

The multichannel effect can be seen best when we also take the two-body interaction effect into account. The inter-particle interaction scatters particles between different momentum channels and hence enhances the multichannel effect. The momentum density distribution of the condensate becomes highly-distorted after it passes the avoided crossing, see Fig. 2.13. Since the interaction causes a broadening of the condensate wave function, the velocity of the front part of the wave packet moves faster the the end part. Therefore, more tunneling is observed in the front part due to the higher velocity.

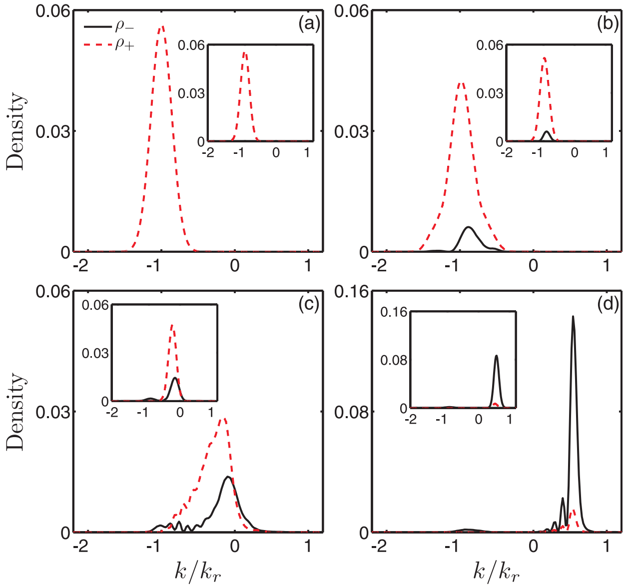

Figure 2.13.: Time evolution of density profiles of the spinor BEC at $tE_r =$ (a) 0, (b) 2.4, (c) 12, and (d) 19.6 with the consideration of the two-body interaction. The panels inside each figure are the non-interacting results. Figures taken from Ref.[29].

2.3 Conclusions

In this chapter, the transition dynamics in the spin-orbit coupled BEC is studied, and the high tunability in the cold atomic system provides us an excellent way to control the crossover from the adiabatic dynamics to the nonadiabatic one. The understanding of the non-adiabatic behavior provides a good indicator to study related physics when adiabaticity is needed. The good control over the dynamics of atoms also suggests a possibility of using a spin-orbit coupled atom as an ”atomtronic” device.

3. ULTRACOLD SCATTERING IN THE PRESENCE OF WEYL SPIN-ORBIT COUPLING

Spin-orbit coupling is characterized by its unusual energy dispersion relations. Early on, the double minimum energy dispersion was proposed to generate macroscopic quantum superposition states with repulsive interatomic interactions [52]. The non-quadratic energy dispersion relation modifies the density of states, and has been shown to significantly change the bound state spectrum [53, 54, 55]. For example, it has been proved theoretically that bound states for two spin-1/2 fermions exist for an arbitrarily weak attraction in the presence of Weyl (or 3D isotropic) spin-orbit coupling [54]. Not only the two-body bound state spectrum but also the scattering formalism becomes modified since SOC exists to infinite distance and this will be the main topic in this chapter.

Duan *et al.* [56] have first treated the scattering problem of two spin-1/2 fermions with zero total angular momentum in the presence of isotropic SOC. We have generalized their treatment so now our formulation applies to any two identical bosons or fermions of arbitrary spin, for arbitrary values of the total angular momentum of the system. An advantage to the choice of isotropic SOC, which is a 3D analog of Rashba SOC, is that it has higher symmetry than other types of SOC, and is more closely related to some cases in condensed matter physics [57, 58]. The conservation of total angular momentum allows us to develop a fully analytical treatment of scattering theory in the presence of SOC. The generalization of two-body scattering to higher spin atoms can extend our understanding to higher spin physics having no counterparts in condensed matter systems. For instance, a system of spin-3/2 fermions with contact potential interactions has been shown to have exact SO(5) symmetry, and a novel quartetting order (a four-fermion version of Cooper pairing) has been proposed [59].

Understanding the two-body physics also paves the way to more interesting varieties of universal Efimov physics [60, 61, 62]. Although Rashba-type SOC has not yet been realized experimentally, proposals have been made that are based on adding more laser fields [63] or else by applying magnetic pulses [15, 16] to imprint an engineered phase onto the atoms.

This chapter is written based on mostly the publication in Phys. Rev. A, **91**, 022706 (2015) and is organized as follows: Sec. 3.1 presents a systematic way to formulate the multichannel 2-body scattering problem with SOC present, and outlines the route to extract the scattering information. The analytical expression for the free Green's matrix with SOC is derived in Sec. 3.2. When the atoms interact through a regularized s-wave interaction, which is an excellent assumption in the ultracold regime, the Lippmann-Schwinger equation can then be cast into a simple form having a closed form solution as shown in Sec. 3.3. Utilization of the Green's matrix and the Lippmann-Schwinger equation enables the analytical scattering wave functions to be found, and the scattering properties extracted. Sec. 3.4 applies our methodology to a system of two identical spin-1 bosonic atoms, and derives the scattering cross sections. An unusual type of threshold behavior is seen to emerge in the low energy scattering cross section. Sec. 3.4 confirms the spontaneous emergence of handedness in this type of system having no parity symmetry. Discussion about two-body bound states is included too. Finally, Sec. 3.5 discusses our conclusions.

3.1 Model

For identical particles interacting with each other in the presence of isotropic 3D spin-orbit coupling, the two-body Hamiltonian is expressed as

$$H_{\mathrm{2b}} = \frac{\hbar^2 \vec{k}_1^2}{2m} + \frac{\hbar^2\lambda}{m}\vec{k}_1 \cdot \vec{s}_1 + \frac{\hbar^2 \vec{k}_2^2}{2m} + \frac{\hbar^2\lambda}{m}\vec{k}_2 \cdot \vec{s}_2 + V(\vec{r}_1 - \vec{r}_2), \tag{3.1}$$

where m is the atomic mass, λ is the strength of the spin-orbit coupling and $V(\vec{r}_1 - \vec{r}_2)$ is the interatomic interaction. The operator $\vec{s}_1$ and $\vec{s}_2$ are the hyperfine spin operators for atom 1 and atom 2; hereafter these are referred to simply as spin. Since the total momentum in the system is conserved, the center of mass motion and the relative motion can be decoupled. The two-body Hamiltonian can be rewritten as usual using the center of mass momentum operator $\vec{P} = \vec{p}_1 + \vec{p}_2$, and the relative momentum operator $\vec{p} = (\vec{p}_1 - \vec{p}_2)/2$. The two-body Hamiltonian then becomes

$$H_{\rm 2b} = H_{\rm com} + H_{\rm rel} \quad = \frac{\vec{P}^2}{4m} + \frac{\hbar\lambda}{2m}\vec{P}\cdot(\vec{s}_1 + \vec{s}_2) + \frac{\vec{p}^2}{m} + \frac{\hbar\lambda}{m}\vec{p}\cdot(\vec{s}_1 - \vec{s}_2) + V(\vec{r}_1 - \vec{r}_2). \tag{3.2}$$

Although the center of mass momentum and the relative motion can be separated out, the relative motion is generally coupled to the center of mass motion via the spin degrees of freedom. To simplify the present calculation, the remainder of this paper is formulated within the center of mass frame and we focus on the case of $\vec{P} = 0$. (Note also that the orbital angular momentum of center of mass is $L_{\vec{R}} = 0$); thus, $H_{\rm 2b} = H_{\rm rel} + V(\vec{r}_1 - \vec{r}_2)$. When the center of mass momentum is nonzero, this breaks the continuous rotational invariance of relative energy spectra and degeneracies of relative band energies are lifted, although we do not discuss it here in detail.

A key first step is to solve the relative Schrödinger equation in the absence of interactions. Since the relative momentum commutes with the non-interacting Hamiltonian, it is advantageous to solve it in momentum space and then Fourier transform the solution back to position space. Taking spin-1 bosons as an example, the non-interacting two-body states are:

$$\langle\vec{r}|\zeta,\xi;\vec{k}\rangle = \frac{1}{\sqrt{2}}\big(\,|\zeta,\hat{k}\rangle_1\,|\xi,-\hat{k}\rangle_2\,e^{i\vec{k}\cdot\vec{r}} + |\xi,-\hat{k}\rangle_1\,|\zeta,\hat{k}\rangle_2\,e^{-i\vec{k}\cdot\vec{r}}\big), \tag{3.3}$$

where $|\zeta, \hat{k}\rangle$ and $|\xi, \hat{k}\rangle$ are one of the following single-particle states:

$$|-, \hat{k}\rangle = \begin{pmatrix} e^{-i\phi_{\vec{k}}} \frac{(1-\cos\theta_{\vec{k}})}{2} \\ -\frac{\sin\theta_{\vec{k}}}{\sqrt{2}} \\ e^{i\phi_{\vec{k}}} \frac{(1+\cos\theta_{\vec{k}})}{2} \end{pmatrix}, \; E_- = \frac{\hbar^2 k^2}{2m} - \frac{\hbar^2 \lambda k}{m} \tag{3.4}$$

$$|0, \hat{k}\rangle = \begin{pmatrix} -e^{-i\phi_{\vec{k}}} \frac{\sin\theta_{\vec{k}}}{\sqrt{2}} \\ \cos\theta_{\vec{k}} \\ e^{i\phi_{\vec{k}}} \frac{\sin\theta_{\vec{k}}}{\sqrt{2}} \end{pmatrix}, \; E_0 = \frac{\hbar^2 k^2}{2m} \tag{3.5}$$

$$|+, \hat{k}\rangle = \begin{pmatrix} e^{-i\phi_{\vec{k}}} \frac{(1+\cos\theta_{\vec{k}})}{2} \\ \frac{\sin\theta_{\vec{k}}}{\sqrt{2}} \\ e^{i\phi_{\vec{k}}} \frac{(1-\cos\theta_{\vec{k}})}{2} \end{pmatrix}, \; E_+ = \frac{\hbar^2 k^2}{2m} + \frac{\hbar^2 \lambda k}{m} \tag{3.6}$$

where $\theta_{\vec{k}}$ and $\phi_{\vec{k}}$ describe the direction of the particle's motion along $\hat{k}$. The eigenstates are expressed in the basis of $\{|1,1\rangle, |1,0\rangle, |1,-1\rangle\}$, which are the eigenstates of the s_z operator for each atom. The three states in Eq.(3.4)$\sim$(3.6) are also eigenstates of the helicity operator, $h = \vec{p}\cdot\vec{s}/p$, with eigenvalues -1, 0, and 1. In general, the eigenvalues range from $-s$, $-s+1$, ... to s for spin $\vec{s}$. The helicity states can be pictured in an intuitive way as follows: when a spin, $\vec{s}$, moves along direction $\hat{k}$, there are $(2s+1)$ possible spin configurations. See Fig. 3.1 for an example. The maximum (minimum) helicity state represents the state when the particle's spin is in parallel (antiparallel) to the direction of its motion. For the same canonical momentum, when spin is aligned with its momentum, the state has the highest eigenvalue. In the following, we will mainly discuss how the particles with definite helicity are going to be scattered to different helicity states through a helicity non-conserving interaction.

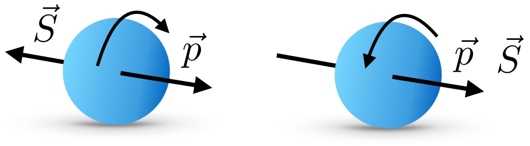

Figure 3.1.: Two different helicity states for a spin-$\frac{1}{2}$ particle.

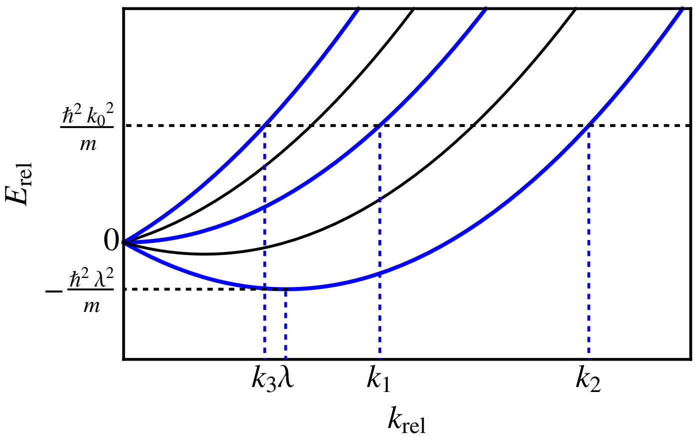

Figure 3.2.: The relative energy-momentum dispersion relation for the spin-1 bosons is depicted. There are 9 bands in total. However, bands with the same resultant spin component along the direction of the relative motion are degenerate. The degeneracies from left to right are 1, 2, 3, 2, and 1. The allowed relative canonical momenta (in blue bands) at $E \equiv \hbar^2 k_0^2/m > 0$, for $|J=0\rangle$ subspace, are labeled by $k_1 = k_0$, $k_2 = \sqrt{k_0^2+\lambda^2}+\lambda$ and $k_3 = \sqrt{k_0^2+\lambda^2}-\lambda$. The unlabeled momenta crossed by black bands are important only when we move to a higher J subspace. The lowest scattering threshold energy occurs at $k_2 = \lambda$. Taken from Ref. [64].

The methodology to solve the two-body scattering problem is sketched below: we first calculate the regular and irregular solutions of the non-interacting system that satisfy the correct boundary conditions, and then use those solutions to construct the free-particle Green's matrix with isotropic spin-orbit coupling. The Green's matrix is then used in the Lippmann-Schwinger equation to solve for the scattered wave functions.

3.2 Green's matrix with spin-orbit coupling

The crucial symmetry in this isotropic spin-orbit system is the conservation of total angular momentum. This allows us to expand the solutions in a complete basis set having a fixed value of the total angular momentum quantum number, J. Because both the orbital angular momentum and the spin angular momentum would be conserved in the absence of spin-orbit coupling, tensor spherical harmonics [65] are adopted as the basis set. These are simultaneous eigenstates of $\{\vec{J}^2, J_z, \vec{L}^2, \vec{S}^2\}$, where $\vec{L}$ is the (relative) orbital angular momentum and $\vec{S} = \vec{s}_1 + \vec{s}_2$ is the total spin angular momentum. In terms of this basis set, spin-orbit coupling simply mixes states with different $\{L, S\}$-values, which label these basis functions. Consequently the Hamiltonian matrix elements in this basis set have nonzero off-diagonal elements. The tensor spherical harmonics are defined as

$$Y_{JM}^{LS}(\theta,\phi) = \sum_{m_L,m_S} C_{Lm_L,Sm_S}^{JM} Y_{Lm_L}(\theta,\phi)\chi(S,m_S) \tag{3.7}$$

where C_{Lm_L,Sm_S}^{JM} is the Clebsch-Gordan coefficient, $Y_{Lm_L}(\theta,\phi)$ is the spherical harmonics, and $\chi(S,m_S)$ is the spin state for total spin S. Any wave function can be expanded in this tensor spherical harmonics basis set,

$$\Psi_\eta^{JM}(r,\theta,\phi) = \sum_{\{L,S\}} \frac{u_{\{L,S\},\eta}^{JM}(r)}{r} \times Y_{JM}^{LS}(\theta,\phi), \tag{3.8}$$

where $u(r)$ is the reduced radial wave function and the index η represents different independent solutions. The matrix element of the kinetic energy operator is easily evaluated, and the result is familiar:

$$\langle (L',S')J'M'|\frac{\vec{p}^2}{m}|(L,S)JM\rangle = (-\frac{\hbar^2}{m}\frac{d^2}{dr^2} + \frac{L(L+1)\hbar^2}{mr^2})\delta_{J,J'}\delta_{M,M'}\delta_{L,L'}\delta_{S,S'}. \tag{3.9}$$

Matrix elements of the spin-orbit coupling term are evaluated using the Wigner-Eckart theorem in the convention of Ref. [65]:

$$\begin{aligned} &\langle (L',S')J'M'|\vec{p}\cdot(\vec{s}_1-\vec{s}_2)|(L,S)JM\rangle \\ &= (-1)^{J+L+S'} \times \delta_{JJ'}\delta_{MM'}\langle L'\|p^{(1)}\|L\rangle\langle S'\|s_1^{(1)}-s_2^{(1)}\|S\rangle \begin{Bmatrix} L' & L & 1 \\ S & S' & J \end{Bmatrix}, \end{aligned} \tag{3.10}$$

where the curly bracket denotes the $6j$ symbol and the double bars stand for reduced matrix elements, which are defined by

$$\langle L' \| p^{(1)} \| L \rangle = \frac{\langle L' m_L' | p_q^{(1)} | L m_L \rangle}{C_{L m_L, 1q}^{L' m_L'}} \sqrt{2L'+1}, \tag{3.11}$$

$$\langle S' \| s^{(1)} \| S \rangle = \frac{\langle S' m_S' | s_q^{(1)} | S m_S \rangle}{C_{S m_S, 1q}^{S' m_S'}} \sqrt{2S'+1}, \tag{3.12}$$

where the superscript inside the parentheses is the rank of the operator and the subscript means the qth component of that tensor operator. All the dependence on magnetic quantum numbers occur now in the Clebsch-Gordan coefficients, in the usual spirit of the Wigner-Eckart theorem. Application of some straightforward angular momentum algebra yields the matrix element of $\vec{p} \cdot (\vec{s}_1 - \vec{s}_2)$,

$$\begin{aligned}
&\langle (L', S') J' M' | \vec{p} \cdot (\vec{s}_1 - \vec{s}_2) | (L, S) J M \rangle \\
&= \delta_{JJ'} \delta_{MM'} \sqrt{(2S+1)(2S'+1)} \begin{Bmatrix} L' & L & 1 \\ S & S' & J \end{Bmatrix} (-1)^{J+L+S'+s_1+s_2} \\
&\times \Bigg[-(-1)^{S} \sqrt{s_1(s_1+1)(2s_1+1)} \begin{Bmatrix} s_1 & s_2 & S \\ S' & 1 & s_1 \end{Bmatrix} + (-1)^{S'} \sqrt{s_2(s_2+1)(2s_2+1)} \begin{Bmatrix} S & S' & 1 \\ s_2 & s_2 & s_1 \end{Bmatrix} \Bigg] \\
&\times \begin{cases} -i\hbar(\frac{d}{dr} - \frac{L}{r}) \sqrt{(L+1)} & \text{if } L' = L+1 \\ i\hbar(\frac{d}{dr} + \frac{L+1}{r}) \sqrt{L} & \text{if } L' = L-1 \end{cases}
\end{aligned} \tag{3.13}$$

The spin-orbit interaction couples states with orbital angular momentum differing by one, which reflects the fact that the rank of the momentum operator is one. The above matrix elements enable the n-coupled radial differential equations to be written for any two spins with any total angular momentum J in their center of mass frame. The number n represents the total number of basis functions in $|J\rangle$ subspace. To solve the coupled differential equations, we make an *ansatz* that the regular solutions take the form,

$$\underline{f}_\eta(r) = \begin{pmatrix} c_1 k_\eta r j_{L_1}(k_\eta r) \\ c_2 k_\eta r j_{L_2}(k_\eta r) \\ c_3 k_\eta r j_{L_3}(k_\eta r) \\ \vdots \end{pmatrix}, \tag{3.14}$$

where $j_{L_i}(k_\eta r)$ is the spherical Bessel function, L_1, L_2 and so on are the allowed L values from the basis functions of $n = 1, n = 2, ...$, and k_η is the canonical momentum for the ηth independent solution at a fixed incident energy, E. The total number of the independent solutions, η, is equal to the total number of the basis functions, n. For non-zero J, degeneracies of bands become important and the total number of *different* k_η may be less than the total number of basis functions concerned. However, this does not affect the form of solution given in Eq. (3.14).

Plugging in this ansatz into the coupled differential equations, the differential equations reduce to an eigenvalue problem, $\underline{\tilde{H}}\ \underline{\tilde{\Psi}} = \tilde{E}\underline{\tilde{\Psi}}$, where $\underline{\tilde{H}}$ is given by

$$\begin{aligned} \langle L', S'|\tilde{H}|L, S\rangle &= (-1)^{J+L+S'+s_1+s_2}\sqrt{(2S+1)(2S'+1)} \\ &\times \Bigg[-(-1)^S \begin{Bmatrix} s_1 & s_2 & S \\ S' & 1 & s_1 \end{Bmatrix} \times \sqrt{s_1(s_1+1)(2s_1+1)} \\ &+ (-1)^{S'} \begin{Bmatrix} S & S' & 1 \\ s_2 & s_2 & s_1 \end{Bmatrix} \times \sqrt{s_2(s_2+1)(2s_2+1)} \Bigg] \\ &\times \frac{i\hbar^2 \lambda k}{m} \begin{Bmatrix} L' & L & 1 \\ S & S' & J \end{Bmatrix} \begin{cases} \sqrt{(L+1)} & \text{if } L' = L+1 \\ \sqrt{L} & \text{if } L' = L-1, \end{cases} \end{aligned} \tag{3.15}$$

and

$$\underline{\tilde{\Psi}} = \{c_1, c_2, c_3, ...\}^T. \tag{3.16}$$

The eigenvalues of the matrix $\tilde{H}$ will solve for canonical momenta for fixed energy $E = \tilde{E} + \hbar^2 k_\eta^2/m$. With the standard technique of diagonalization, the solutions of $\{c_1, c_2, \dots\}$ can be found, so are the regular solutions. The solutions irregular at the origin are obtained by replacing the spherical Bessel functions by spherical Neumann functions, $y_{L_i}(k_\eta r)$,

$$\underline{g}_\eta(r) = \begin{pmatrix} c_1 k_\eta r y_{L_1}(k_\eta r) \\ c_2 k_\eta r y_{L_2}(k_\eta r) \\ c_3 k_\eta r y_{L_3}(k_\eta r) \\ \vdots \end{pmatrix}. \tag{3.17}$$

The above solutions in Eq. (3.14) and Eq. (3.17) will be properly energy normalized for an appropriate choice of the momentum-dependent constants, as is carried out below. The reduced radial Green's matrix is shown in Appendix B to be

$$\underline{\mathscr{G}}(r, r') = \begin{cases} \pi \underline{f}(r) \underline{g}^\dagger(r') & \text{for} \quad r < r', \\ \pi \underline{g}(r) \underline{f}^\dagger(r') & \text{for} \quad r > r'. \end{cases} \tag{3.18}$$

The factor π appears because of our choice of normalization. More details about energy normalization are also given in appendix A.

3.3 Lippmann-Schwinger equation

To solve the scattering wave function for two atoms with isotropic spin-orbit coupling, we apply the Lippmann-Schwinger equation, which is the integral form of the Schrödinger equation.

$$\Psi(\vec{r}) = \Psi_0(\vec{r}) + \int G(\vec{r}, \vec{r}') V(\vec{r}') \Psi(\vec{r}') d\vec{r}', \tag{3.19}$$

where $\Psi_0(\vec{r})$ is the non-interacting solution, $G(\vec{r}, \vec{r}')$ is the free Green's function without 2-body interaction, $V(\vec{r}')$. To compute the wave function that describes scattering processes, we must in general solve the 3-dimensional integral equation in a self-consistent way, which for an arbitrary two-body potential relies on numerics. However, for low energy scattering, the interatomic interaction is well described by the regularized s-wave Fermi pseudo potential, $V(\vec{r}) = \frac{4\pi\hbar^2 a_s}{m} \delta(\vec{r}) \frac{\partial}{\partial r}(r)$, where a_s is the s-wave scattering length. It can be shown that the 3D integral equation can be reduced to a 1D radial integral equation, and the scattered wave functions can be obtained in a closed form solution,

$$R(r) = R_0(r) + \int_0^\infty G(r,r')V(r')R(r')r'^2 dr'. \tag{3.20}$$

Here $R_0(r)$ is the free radial two-body wave function. To better illustrate the idea, consider the case of *zero* total angular momentum, since in this subspace, the s-wave channel is always present.

For any two identical particles with spins having zero total angular momentum, the channel structure is $\{L,S\} = \{0,0\}$, $\{1,1\}$, $\{2,2\}$, $\ldots$, and $\{2s_1, 2s_1\}$ since from spin statistics $L+S$ has be to even to incorporate the symmetry of identical bosons or fermions. There are $(2s_1+1)$ channels in total. The regularized s-wave contact potential is

$$\underline{V}(r) = \begin{pmatrix} g\frac{\delta(r)}{4\pi r^2}\frac{\partial}{\partial r}r & 0 & \ldots \\ 0 & 0 & \ldots \\ \vdots & \vdots & \ddots \end{pmatrix}_{(2s_1+1)\times(2s_1+1)}, \tag{3.21}$$

where $g = 4\pi\hbar^2 a_s/m = 4\pi\tilde{g}$. After applying the operation, $\int_0^\infty dr\tilde{g}\delta(r)\frac{\partial}{\partial r}(r)$, to both sides of Eq. (3.20), the scattering solutions have the following closed form representation:

$$\begin{pmatrix} R_{1\eta}(r) \\ R_{2\eta}(r) \\ R_{3\eta}(r) \\ \vdots \end{pmatrix} = \begin{pmatrix} R_{0,1\eta}(r) + G_{11}(r,0)\frac{\tilde{g}}{1-\tilde{g}G_{11}^{\text{reg}}(0,0)}R_{0,1\eta}^{\text{reg}}(0) \\ R_{0,2\eta}(r) + G_{21}(r,0)\frac{\tilde{g}}{1-\tilde{g}G_{11}^{\text{reg}}(0,0)}R_{0,1\eta}^{\text{reg}}(0) \\ R_{0,3\eta}(r) + G_{31}(r,0)\frac{\tilde{g}}{1-\tilde{g}G_{11}^{\text{reg}}(0,0)}R_{0,1\eta}^{\text{reg}}(0) \\ \vdots \end{pmatrix}, \tag{3.22}$$

where $\eta (= 1,2,3,\ldots,2s_1+1)$ labels solutions with different canonical momenta, regularized functions $f^{\text{reg}}(0) \equiv \frac{\partial}{\partial r}(rf(r))|_{r\to 0}$, and $f^{\text{reg}}(0,0) \equiv \frac{\partial}{\partial r}(rf(r,0))|_{r\to 0}$.

For systems with nonzero total angular momentum, the algebra can become slightly more involved. The complexity mainly comes from the fact that there are more than one basis function with the same orbital angular momentum but different total spin angular momentum. Degeneracies appear for the two-particle states within some non-zero total angular momentum subspace. This is expected as was already seen in the discussion of Sec. 3.1. Nevertheless, even in this situation, the same methodology can be applied to reduce the coupled differential equations to an eigenvalue problem.

3.4 Another example: two spin-1 bosons

The formalism presented above has been verified to reproduce the results presented by Duan *et al.* for two identical spin-1/2 fermions. The following applies our methodology to the system of two identical spin-1 bosons as a concrete example. One thing worth pointing out is that the normalization factors of the regular/irregular solutions were not written out explicitly in the Duan *et al.* study, presumably because the factors could be taken to be identical for all the independent solutions. But in the present generalized treatment, it is necessary to keep track of them to ensure flux conservation.

For two spin-1 bosons with $J = 0$, there are only three relevant channels with $\{L, S\} = \{0, 0\}, \{1, 1\}$ and $\{2, 2\}$. The coupled reduced radial differential equations are

$$\frac{\hbar^2}{m}\begin{pmatrix} -\frac{d^2}{dr^2} & \frac{i2\sqrt{2}\lambda}{\sqrt{3}}(\frac{d}{dr}+\frac{1}{r}) & 0 \\ \frac{i2\sqrt{2}\lambda}{\sqrt{3}}(\frac{d}{dr}-\frac{1}{r}) & -\frac{d^2}{dr^2}+\frac{2}{r^2} & \frac{i2\lambda}{\sqrt{3}}(\frac{d}{dr}+\frac{2}{r}) \\ 0 & \frac{i2\lambda}{\sqrt{3}}(\frac{d}{dr}-\frac{2}{r}) & -\frac{d^2}{dr^2}+\frac{6}{r^2} \end{pmatrix}\begin{pmatrix} u_{00}^{00} \\ u_{11}^{00} \\ u_{22}^{00} \end{pmatrix} = E\begin{pmatrix} u_{00}^{00}(r) \\ u_{11}^{00}(r) \\ u_{22}^{00}(r) \end{pmatrix}. \tag{3.23}$$

The tridiagonal structure signatures the existence of the spin-orbit coupling. Assuming the regular solution has this form,

$$\{u_{00}^{00}(r), u_{11}^{00}(r), u_{22}^{00}(r)\}^T = \{c_1 kr j_0(kr), c_2 kr j_1(kr), c_3 kr j_2(kr)\}^T, \tag{3.24}$$

the following eigenvalue problem is obtained.

$$\begin{pmatrix} \frac{\hbar^2k^2}{m}-E & 2i\hbar^2\sqrt{\frac{2}{3}}\frac{\lambda k}{m} & 0 \\ -2i\hbar^2\sqrt{\frac{2}{3}}\frac{\lambda k}{m} & \frac{\hbar^2k^2}{m}-E & 2i\hbar^2\sqrt{\frac{1}{3}}\frac{\lambda k}{m} \\ 0 & -2i\hbar^2\sqrt{\frac{1}{3}}\frac{\lambda k}{m} & \frac{\hbar^2k^2}{m}-E \end{pmatrix}\begin{pmatrix} c_1 \\ c_2 \\ c_3 \end{pmatrix} = 0, \tag{3.25}$$

Diagonalization of Eq. (3.25) yields the eigenvalues and eigenvectors.

$$\begin{pmatrix} c_1 \\ c_2 \\ c_3 \end{pmatrix} = \begin{pmatrix} \sqrt{\frac{1}{3}} \\ 0 \\ \sqrt{\frac{2}{3}} \end{pmatrix} \text{ for } E = \frac{\hbar^2 k^2}{m}, \tag{3.26}$$

$$\begin{pmatrix} c_1 \\ c_2 \\ c_3 \end{pmatrix} = \begin{pmatrix} \sqrt{\frac{1}{3}} \\ i\sqrt{\frac{1}{2}} \\ -\sqrt{\frac{1}{6}} \end{pmatrix} \text{ for } E = \frac{\hbar^2 k^2}{m} - \frac{2\hbar^2 \lambda k}{m}, \tag{3.27}$$

$$\begin{pmatrix} c_1 \\ c_2 \\ c_3 \end{pmatrix} = \begin{pmatrix} \sqrt{\frac{1}{3}} \\ -i\sqrt{\frac{1}{2}} \\ -\sqrt{\frac{1}{6}} \end{pmatrix} \text{ for } E = \frac{\hbar^2 k^2}{m} + \frac{2\hbar^2 \lambda k}{m}. \tag{3.28}$$

The eigenstates are orthonormal. Moreover, the same energy dispersion relations between the relative energy E and the relative momentum k are obtained by directly diagonalizing the non-interacting Hamiltonian in momentum space. The three thick blue curves plotted in Fig. 3.2 display the energy dispersions from Eq. 3.26 to Eq. 3.28. After writing the incident energy in the notation $E \equiv \hbar^2 k_0^2/m$, the canonical momenta for channel 1 to 3 are found to be $k_1 = k_0, k_2 = \lambda + \sqrt{\lambda^2 + k_0^2}$, and $k_3 = -\lambda + \sqrt{\lambda^2 + k_0^2}$. The set of regular solutions are

$$\frac{\underline{f}(r)}{r} = \begin{pmatrix} \frac{N_1}{\sqrt{3}} k_1 j_0(k_1 r) & \frac{N_2}{\sqrt{3}} k_2 j_0(k_2 r) & \frac{N_3}{\sqrt{3}} k_3 j_0(k_3 r) \\ 0 & i\frac{N_2}{\sqrt{2}} k_2 j_1(k_2 r) & -i\frac{N_3}{\sqrt{2}} k_3 j_1(k_3 r) \\ \frac{N_1\sqrt{2}}{\sqrt{3}} k_1 j_2(k_1 r) & -\frac{N_2}{\sqrt{6}} k_2 j_2(k_2 r) & -\frac{N_3}{\sqrt{6}} k_3 j_2(k_3 r) \end{pmatrix}. \tag{3.29}$$

The above solution can also be confirmed by projecting the plane wave solution in Eq. (3.3) onto the $|J = 0\rangle$ subspace. That is, the column vector $|\alpha\rangle$ of Eq. (3.29) labeled by k_α has one-to-one correspondence with the $|J = 0\rangle$ part of the helicity states in Eq. (3.3). The normalization factors $\{N_1, N_2, N_3\} = \sqrt{\frac{2\mu}{\pi\hbar^2}}\{\sqrt{\frac{1}{k_1}}, \sqrt{\frac{1}{k_2-\lambda}}, \sqrt{\frac{1}{k_3+\lambda}}\}$ to each independent solution are added to ensure that their Wronskians with the irregular solutions (see appendix A) are identical, which in turn guarantees that the computed interaction K-matrix will be symmetric. This step is in fact equivalent to enforcing energy normalization of wave function in the case without spin-orbit coupling.

The multichannel scattering formalism presented here is different from previous treatments when there is no single-particle potential existing even at large distances. In previous studies, one often chooses the asymptotically free states as the base pair of independent solutions to define phaseshifts or reaction matrices and then study how short range interaction mixes different channels and causes particles to be scattered among those channels prior to being detected at large distances. And the incoming basis states expanded in the usual formulations of scattering theory having no long range channel coupling are diagonal solution matrices, which is not the case here as in Eq. (3.29).

After plugging in the free Green's matrix $\underline{G}(r,r') = \underline{\mathscr{G}}(r,r')/(rr')$ from Eq. (3.18) and the free radial wave function $\underline{R}_0(r) = \underline{f}(r)/r$ from Eq. (3.29), we obtain the scattering solutions. The reaction matrix K is determined through the correct asymptotic solution:

$$\underline{R}(r)|_{r\to\infty} \sim \frac{\underline{f}(r)}{r} - \frac{\underline{g}(r)}{r}\underline{K}, \tag{3.30}$$

where we find

$$\underline{K} = \frac{-2a_s}{3}\begin{pmatrix} \frac{k_1}{2} & k_2\sqrt{\frac{k_1}{2(k_2+k_3)}} & k_3\sqrt{\frac{k_1}{2(k_2+k_3)}} \\ k_2\sqrt{\frac{k_1}{2(k_2+k_3)}} & \frac{k_2^2}{(k_2+k_3)} & \frac{k_2k_3}{(k_2+k_3)} \\ k_3\sqrt{\frac{k_1}{2(k_2+k_3)}} & \frac{k_2k_3}{(k_2+k_3)} & \frac{k_3^2}{(k_2+k_3)} \end{pmatrix}. \tag{3.31}$$

From the $\underline{K}$ matrix, the $\underline{S}$ matrix is determined by the usual relation, $\underline{S} = (\underline{I}+i\underline{K})(\underline{I}-i\underline{K})^{-1}$. The unitarity of the $\underline{S}$ matrix is guaranteed by the real and symmetric reaction K matrix as it is in Eq. (3.31).

The scattered solutions defining the $\underline{S}$ matrix can be expressed as in Eq. (3.30),

$$R_{|00,\vec{k}_1\rangle\to|00,\hat{r}\rangle} \underset{r\to\infty}{\longrightarrow} \sqrt{2}\frac{S_{11}-1}{2ik_1}\frac{e^{ik_1 r}}{r}\left|00,\hat{r}\right\rangle \tag{3.32}$$

$$R_{|00,\vec{k}_1\rangle\to|--,\hat{r}\rangle} \underset{r\to\infty}{\longrightarrow} \sqrt{2}\sqrt{\frac{k_1}{k_2-\lambda}}\frac{S_{12}}{2ik_1}\frac{e^{ik_2 r}}{r}\left|--,\hat{r}\right\rangle \tag{3.33}$$

$$R_{|00,\vec{k}_1\rangle\to|++,\hat{r}\rangle} \underset{r\to\infty}{\longrightarrow} \sqrt{2}\sqrt{\frac{k_1}{k_3+\lambda}}\frac{S_{13}}{2ik_1}\frac{e^{ik_3 r}}{r}\left|++,\hat{r}\right\rangle \tag{3.34}$$

$$R_{|--,\vec{k}_2\rangle\to|00,\hat{r}\rangle} \underset{r\to\infty}{\longrightarrow} \sqrt{2}\sqrt{\frac{(k_2-\lambda)}{k_1}}\frac{S_{21}}{2ik_2}\frac{e^{ik_1 r}}{r}\left|00,\hat{r}\right\rangle \tag{3.35}$$

$$R_{|--,\vec{k}_2\rangle\to|--,\hat{r}\rangle} \underset{r\to\infty}{\longrightarrow} \sqrt{2}\frac{S_{22}-1}{2ik_2}\frac{e^{ik_2 r}}{r}\left|--,\hat{r}\right\rangle \tag{3.36}$$

$$R_{|--,\vec{k}_2\rangle\to|++,\hat{r}\rangle} \underset{r\to\infty}{\longrightarrow} \sqrt{2}\sqrt{\frac{k_2-\lambda}{k_3+\lambda}}\frac{S_{23}}{2ik_2}\frac{e^{ik_3 r}}{r}\left|++,\hat{r}\right\rangle \tag{3.37}$$

$$R_{|++,\vec{k}_3\rangle\to|00,\hat{r}\rangle} \underset{r\to\infty}{\longrightarrow} \sqrt{2}\sqrt{\frac{k_3+\lambda}{k_1}}\frac{S_{31}}{2ik_3}\frac{e^{ik_1 r}}{r}\left|00,\hat{r}\right\rangle \tag{3.38}$$

$$R_{|++,\vec{k}_3\rangle\to|--,\hat{r}\rangle} \underset{r\to\infty}{\longrightarrow} \sqrt{2}\sqrt{\frac{k_3+\lambda}{k_2-\lambda}}\frac{S_{32}}{2ik_3}\frac{e^{ik_2 r}}{r}\left|--,\hat{r}\right\rangle \tag{3.39}$$

$$R_{|++,\vec{k}_3\rangle\to|++,\hat{r}\rangle} \underset{r\to\infty}{\longrightarrow} \sqrt{2}\frac{S_{33}-1}{2ik_3}\frac{e^{ik_3 r}}{r}\left|++,\hat{r}\right\rangle \tag{3.40}$$

where the basis $\left|\zeta\xi,\hat{r}\right\rangle \equiv \left|\zeta,\hat{r}\right\rangle\left|\xi,-\hat{r}\right\rangle$. From Eq. (3.3) and Eq. (3.32)∼(3.40), the incoming and outgoing current fluxes are determined by the velocity operator, $\vec{v} = \vec{p}/\mu + \hbar\lambda(\vec{s_1}-\vec{s_2})/m$. The flux densities for the three possible incoming states at energy $E = \hbar^2 k_0^2/\mu$ can be calculated to be $\vec{j}_1 = (\hbar k_0/\mu)\hat{k}_1$ and $\vec{j}_{2/3} = (\hbar\sqrt{k_0^2+\lambda^2}/\mu)\hat{k}_{2/3}$. The flux difference in different channels is incorporated in a way to ensure flux conservation as we have seen in the nontrivial fore factors of scattered wave functions from Eq. (3.32) to Eq. (3.40). The integrated partial cross sections are found by integrating the flux ratio over all solid angles. The total cross section for particles incident in channel α with some helicity to be scattered into channel β of another helicity is

$$\sigma_{\alpha\beta} = \frac{2\pi}{k_\alpha^2}\left|S_{\alpha\beta}-\delta_{\alpha\beta}\right|^2, \tag{3.41}$$

where k_α is the canonical momentum in the incoming state and is determined by the energy, say $E \equiv \hbar^2 k_0^2/m$, and the SOC strength, λ. From now on, we will simply denote k_0 by k. For example, all the x axes of graphs plotting cross sections are $k_0 \equiv k$

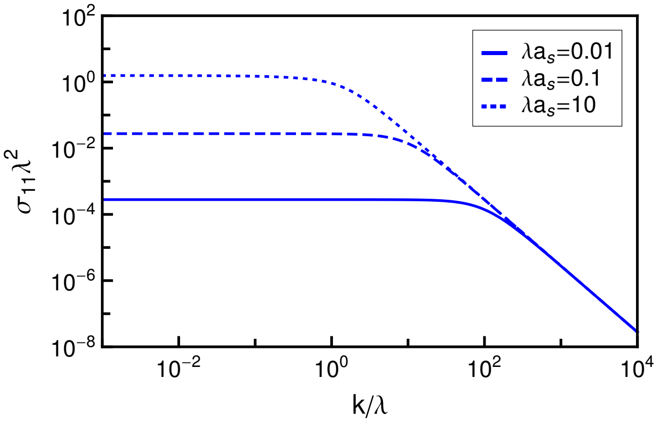

Figure 3.3.: The dimensionless rescaled cross sections to go from the incoming state $|00, \vec{k}_1\rangle$ to the outgoing state $|00, \hat{r}\rangle$ for different values of λa_s as functions of the dimensionless quantity k/λ. Taken from Ref. [64].

for simplicity. Using the SOC strength as the unit of the momentum, the cross section can be rescaled as a function of the dimensionless quantity, λa_s, by choosing the unit of cross section as $1/\lambda^2$. From the estimation in [15][16], a realistic achievable value of the SOC strength $\lambda \simeq 1 - 10/\mu m$, and this guides our chosen values of λa_s in the plots shown for the cross sections.

Turning off the spin-orbit coupling, all of the cross sections display the well-known Wigner threshold law [66]: insensitive to energy in the low k limit (or lower E limit) and proportional to k^{-2} in the higher k limit. This transition happens when $k \sim \frac{1}{a_s}$. The unusual factor, 8/9, is due to the choice of the helicity basis.

$$\sigma_{ij} = \frac{8\pi a_s^2}{9 + 9a_s^2 k^2} \approx \begin{cases} \frac{8\pi a_s^2}{9} & k \ll \frac{1}{a_s} \\ \frac{8\pi}{9k^2} & k \gg \frac{1}{a_s} \end{cases} \quad \forall\, i, j. \tag{3.42}$$

In the limit of high k (but still low energy) scattering, the scattering cross section becomes insensitive to the existence of spin-orbit coupling. This is expected since at small distance, the short-range interaction dominates and the physics of SOC becomes

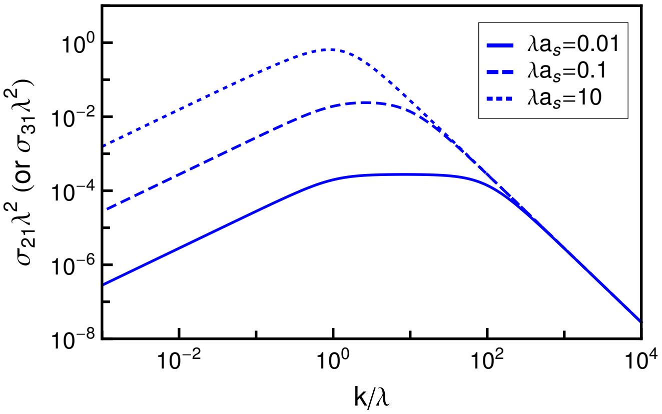

Figure 3.4.: The dimensionless rescaled cross sections to go from from the incoming state $|--, \vec{k}_2\rangle$ ($|++, \vec{k}_3\rangle$) to the outgoing state $|00, \hat{r}\rangle$ for different values of λa_s as functions of the dimensionless quantity k/λ. Taken from Ref. [64].

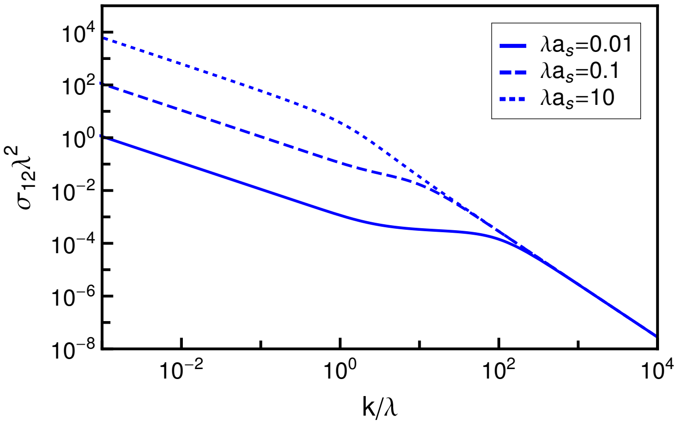

Figure 3.5.: The dimensionless rescaled cross sections to go from the incoming state $|00, \vec{k}_1\rangle$ to the outgoing state $|--, \hat{r}\rangle$ for different values of λa_s as functions of the dimensionless quantity k/λ. Taken from Ref. [64].

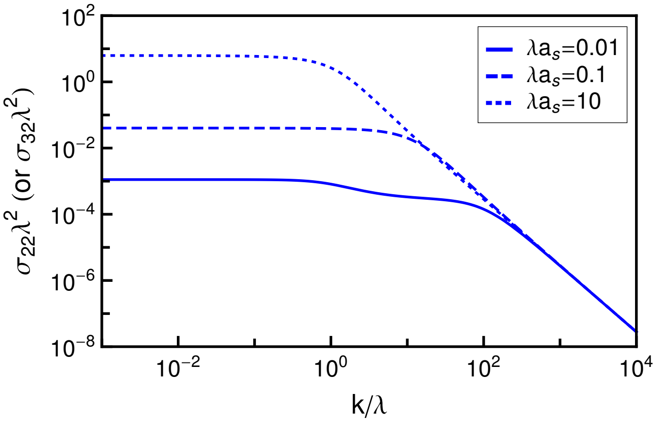

Figure 3.6.: The dimensionless rescaled cross sections to go from the incoming state $|{-}{-},\vec{k}_2\rangle$ ($|{+}{+},\vec{k}_3\rangle$) to the outgoing state $|{-}{-},\hat{r}\rangle$ for different values of λa_s as functions of the dimensionless quantity k/λ. Taken from Ref. [64].

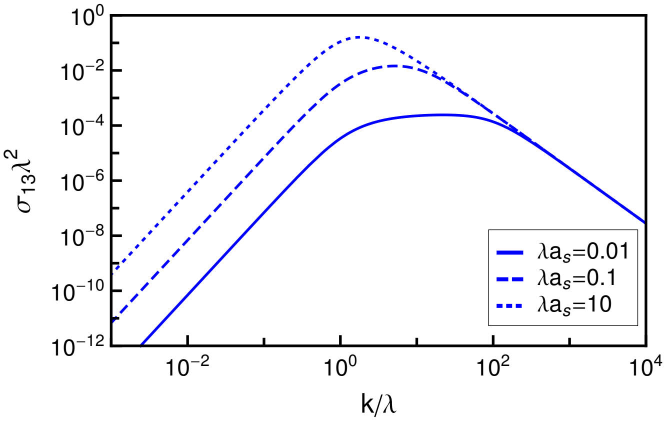

Figure 3.7.: The dimensionless rescaled cross sections to go from the incoming state $|00,\vec{k}_1\rangle$ to the outgoing state $|{+}{+},\hat{r}\rangle$ for different values of λa_s as functions of the dimensionless quantity k/λ. Taken from Ref. [64].

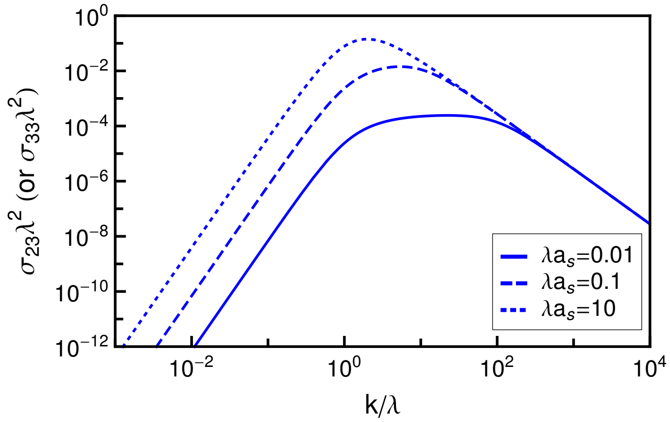

Figure 3.8.: The dimensionless rescaled cross sections to go from the incoming state $|{-}{-}, \vec{k}_2\rangle$ ($|{+}{+}, \vec{k}_3\rangle$) to the outgoing state $|{+}{+}, \hat{r}\rangle$ for different values of λa_s as functions of the dimensionless quantity k/λ. Taken from Ref. [64].

insignificant. All cross sections are combined into the same curve in this limit, namely $\sigma_{ij} \sim 8\pi/(9k^2)$ as in the high energy limit of non-SOC cases.

The effect of spin-orbit coupling becomes important as energy decreases below the energy scale set by SOC. This explains why there exists a transitional plateau when $\lambda < k < 1/a_s$. This is of course possible only when the interatomic interaction is weaker than SOC. The cross sections in the low k limit are no longer energy independent and show some unusual features. The cross sections in different channels are characterized by different power laws at very low temperatures. Scattering is enhanced or suppressed depending on which outgoing channels are taken. The scaling laws are summarized as follows in terms of the appropriate k_α for $\alpha = 1, 2, 3$, which are the wavenumbers that vanish at the relevant threshold. Since k_1 and k_3 both go to zero with different power laws at the threshold energy $E = \hbar^2 k^2/m \to 0$, where $k_3 \propto k_1^2$, we will express those relevant cross sections in terms of $k_1 \equiv k$ for consistency.

$$\sigma_{11} \approx \frac{8\pi a_s^2}{9 + 16(\lambda a_s)^2} \qquad \text{for } k \ll \lambda \tag{3.43}$$

$$\sigma_{21} \approx \frac{8\pi a_s^2}{9 + 16(\lambda a_s)^2} \frac{k}{\lambda} \qquad \text{for } k \ll \lambda \tag{3.44}$$

$$\sigma_{12} \approx \frac{32\pi a_s^2}{9 + 16(\lambda a_s)^2} \left(\frac{k}{\lambda}\right)^{-1} \qquad \text{for } k \ll \lambda \tag{3.45}$$

$$\sigma_{22} \approx \frac{32\pi a_s^2}{9 + 16(\lambda a_s)^2} \qquad \text{for } k \ll \lambda \tag{3.46}$$

$$\sigma_{13} \approx \frac{2\pi a_s^2}{9 + 16(\lambda a_s)^2} \left(\frac{k}{\lambda}\right)^{3} \qquad \text{for } k \ll \lambda \tag{3.47}$$

$$\sigma_{23} \approx \frac{2\pi a_s^2}{9 + 16(\lambda a_s)^2} \left(\frac{k}{\lambda}\right)^{4} \qquad \text{for } k \ll \lambda \tag{3.48}$$

Notice that for the channel σ_{22}, the appropriate scaling momentum is $k_2 \to 0$. However, in this case, channel 1 and 3 should be included as closed channels since energy $E < 0$, which is beyond the scope of our discussion here. We will simply consider the scaling law of σ_{22} as $E \to 0$ (or $k \to 0$). The cross sections in Eq. (3.43)−Eq. (3.46) are all consistent with the expected Wigner threshold law behavior, but σ_{13} and σ_{23} deviate, which is one notable effect of the spin-orbit interaction in this system.

Although we have only included the short-range interaction, the modification of threshold laws is expected since the SOC exists to an infinitely large distance. The new scaling laws indeed show up as a result of the unusual energy dispersion relation in the presence of SOC. The energy bands generate different canonical momenta as well as different velocities (or flux densities) in different channels. The difference in flux densities needs to be considered carefully also in the threshold laws. The original Wigner's theory has been modified to incorporate the effect from SOC. Inspection of Eq. (3.31) shows that each element of the reaction matrix $K_{\alpha\beta}$ is proportional to $K_{\alpha\beta} \propto k_\alpha k_\beta / \sqrt{\tilde{k}_\alpha \tilde{k}_\beta}$ where $\tilde{k}_\alpha = k_1$ for α =1 and $(k_2 + k_3)$ for $\alpha = 2$ or 3. Thus, the cross section at low energy scales like $\sigma_{\alpha\beta} \propto k_\beta^2 / (\tilde{k}_\alpha \tilde{k}_\beta)$. For example, the channel $\sigma_{12} \sim k_2^2/(k_1(k_2 + k_3)) \sim \lambda/k$. The divergence of σ_{12} with only short range interaction might seem unnatural, but the divergence of superelastic cross sections does occur in ordinary non-SOC scattering since the atoms are scattered into a larger final momentum state. This is true for the familiar Wigner laws already [66].

Even when the cross sections in some channels (σ_{11}, σ_{22}, and σ_{32}) at low temperatures in the presence of SOC are insensitive to energy, the effect of SOC can still be seen by studying the threshold values. When $\lambda a_s \lesssim 1$ ($\lambda a_s \gtrsim 1$), the cross section σ_{22} or σ_{32} is increased (decreased) from the non-SOC case. For the particular channel in σ_{11}, the cross section is smaller than the non-SOC case until λa_s reaches 1 from above. Therefore, the effect of SOC cannot be differentiated even in the very low energy limit when $\lambda a_s \lesssim 1$ in the $|00, \hat{r}\rangle \rightarrow |00, \hat{r}\rangle$ channel.

From Fig. 3.3 to Fig. 3.8, processes where particles transfer to the lowest helicity state labeled by k_2 are enhanced compared to the non-SOC case. Moreover, particles are preferentially scattered into the k_2 channel where the particle's momentum is antiparallel to its spin direction, regardless of their incidence channel. Fig. (3.9) shows that the k_2 channel will dominate among all helicity states, as can be seen by comparing the ratios of the different scattering cross sections.

$$\frac{\sigma_{\alpha\beta}}{\sigma_{\beta\alpha}} = \left(\frac{k_\beta}{k_\alpha}\right)^2. \tag{3.49}$$

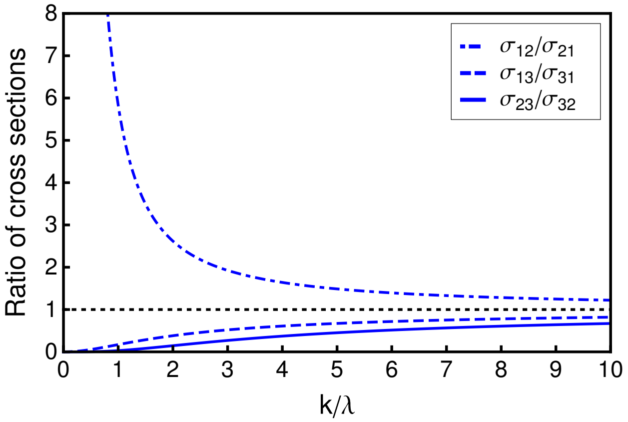

Figure 3.9.: The ratios of cross sections at $\lambda a_s = 1$. Scattering into the lowest helicity state (channel labeled by k_2) dominates at low energy. For cases without spin-orbit coupling, all three ratios are equal to unity, drawn as a black dotted line for reference. Taken from Ref. [64].

We think the SOC system, which can also be interpreted as spins in a momentum-dependent B field, is an analog to an antiferromagnetic system. The magnetic potential energy is minimized when spin is antiparallel to the direction of field. Similarly, particles would like to stay in their lowest helicity states when the particle's spin has a reverse direction to its momentum. The spontaneous handedness appears in parity-breaking systems when interaction can cause fluctuation among system's eigenstates.

The bound state information can also be predicted by searching for the poles of $\underline{S}$ matrix. The scattering threshold energy here is $E_T = -\hbar^2\lambda^2/2\mu$, see Fig. 3.2. For energy $E < E_T$, all channels are closed. We take the following analytical continuation:

$$k_1 = i\kappa \tag{3.50}$$

$$k_2 = i\sqrt{\kappa^2 - \lambda^2} + \lambda \tag{3.51}$$

$$k_3 = i\sqrt{\kappa^2 - \lambda^2} - \lambda, \tag{3.52}$$

where κ is chosen to be positive so the exponentially growing part in the incoming scattering wave functions is killed. The bound state wave function can be found by plugging the continuation into the outgoing wave functions. The new feature brought into the bound state wave function by SOC is that the function is now decaying exponentially with an spatial oscillation whose frequency is set by λ. The binding energy for the bound pair is given by $E_b = E_T + \hbar^2\kappa^2/2\mu > 0$, where κ is found by solving $\mathrm{Det}(\underline{I} - i\underline{K}) = 0$. The binding energy returns to the usual case with an overall constant shift, depending on the strength of SOC, when a_s is approaching zero from the positive side.

$$E_b = \begin{cases} \frac{\hbar^2}{2\mu a_s^2} + \frac{\hbar^2\lambda^2}{2\mu} & \frac{1}{\lambda a_s} \to +\infty \\ \frac{(9-\sqrt{33})\hbar^2\lambda^2}{12\mu} + 4\sqrt{\frac{2}{11} - \frac{1}{\sqrt{33}}}\frac{\hbar^2\lambda}{\mu a_s} & \frac{1}{\lambda a_s} \to 0 \\ \frac{2\hbar^2\lambda^4 a_s^2}{9\mu} & \frac{1}{\lambda a_s} \to -\infty. \end{cases} \tag{3.53}$$

One interesting effect from SOC shows up in the small and negative a_s limit. The binding energy scales algebraically as $\lambda^4 a_s^2$, which indicates that the existence of a two-body bound state no matter how small and attractive the scattering length is as long as SOC exists [54, 63]. The two-body bound state information paves the way to more complex trimer systems.

3.5 Conclusions

The very existence of the spin-orbit coupling to the infinite distance changes the two-body scattering in a fundamental way, for instance, the parity symmetry is broken and the coupling of spin and the translational motion of an atom has reduced the symmetry of the system to only the conservation of *total* angular momentum. In this chapter, we develop a more general treatment of ultracold scattering in the presence of isotropic spin-orbit coupling based on the previous study in Ref. [56]. The formulation can now be applied to any two identical particles with arbitrary spin, in any total angular momentum subspace. This should enable a deeper understanding of low

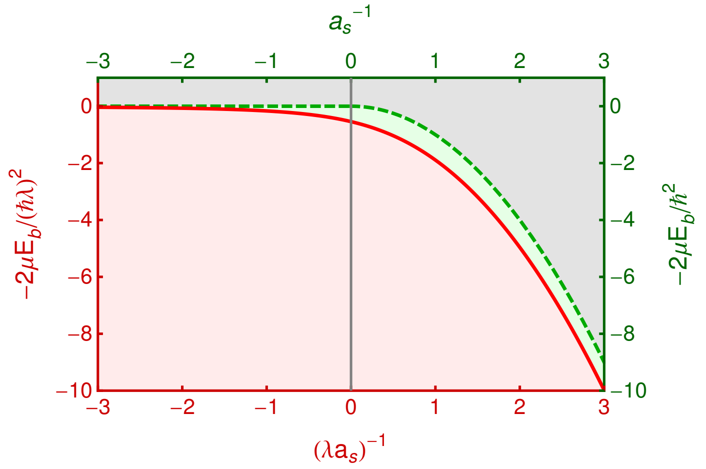

Figure 3.10.: The two-body binding energy for two spin-1 bosons in the presence (red solid line) and absence (green dashed line) of SOC. The bottom and left axes apply to the red curve, and the top and right axes apply to the green dashed curve. Taken from Ref. [64].

energy scattering (or two-body bound states) in the presence of an artificial gauge field, especially those which are non-abelian.

4. SCATTERING IN THE PRESENCE OF RASHBA-DRESSELHAUS SPIN-ORBIT COUPLING IN A REDUCED DIMENSIONALITY

Two-body scattering constitutes the fundamental process in various physical systems ranging from ultracold dilute gases to energetic quark-gluon plasmas. Many interesting phenomena are found already in one-dimensional quantum scattering processes. For instance, when a low-energy particle incidents on a potential well, a transmission resonance could happens when a total destructive interference occurs between the wave reflected on the left wall and all the waves reflected on the right wall. This is exactly the principle for Fabry-Perot interferometers in optics. For another instance, a quantum particle can tunnel through a double-barrier structure as if no potential exists when the particle's energy (even if it is lower than the potential height) is resonant with the quasi-bound state supported by the potential.

In Sec. 4.1, we calculate the transmission and reflection coefficients in 1D ultracold Fermi gases in the presence of an equal-mixing of Rashba-Dresselhaus spin-orbit coupling (RDSOC). Scattering resonances are found whenever the incident energy approaches a scattering threshold or a quasi-bound state. Next, in Sec. 4.2, we propose to observe these 1D scattering resonances with the assistance of confinement-induced resonances (CIRs), where the effective 1D interaction strength could be tuned by changing the ratio of the two length scales set by the background scattering length and the transverse trapping size. The modification of the CIR position by the Raman field will be calculated. Possibilities of using Raman-dressed atomic gases to realize 1D theoretical models with infinitely-repulsive gases or infinitely-attractive gases are discussed at the end of the chapter.

4.1 Scattering resonances in a 1D Rashba-Dresselhaus spin-orbit coupled Fermi gas

We begin by considering the binary collision in the experimental protocol in Zhang's group [33], where they have realized the Rashba-Dresselhaus SOC in a spin-1/2 degenerate Fermi gas with ^{40}K atoms. Since the SOC is in one dimension, we consider only the Hamiltonian associated with the direction of the spin-orbit coupling. The Hamiltonian describing the system is

$$\begin{aligned} H_{\rm 1D} =& H_{\rm 1D}^{(1)} + H_{\rm 1D}^{(2)} + V(x) \qquad (4.1) \\ =& \frac{\hbar^2 k_1^2}{2m} + \frac{\hbar^2\lambda}{m} k_1\sigma_{1x} + \frac{\hbar\Omega}{2}\sigma_{1z} + \frac{\hbar\delta}{2}\sigma_{1x} + \\ & \frac{\hbar^2 k_2^2}{2m} + \frac{\hbar^2\lambda}{m} k_2\sigma_{2x} + \frac{\hbar\Omega}{2}\sigma_{2z} + \frac{\hbar\delta}{2}\sigma_{2x} + V(x), \qquad (4.2) \end{aligned}$$

where $\sigma_{i=x,y,z}$ are Pauli matrices for spin-1/2 particles, λ is the SOC strength, Ω is the Raman coupling strength, δ is the two-photon detuning, and $V(x)$ is the interparticle interaction, where x is the relative coordinate. Without the Raman coupling term, the 1D Rashba-Dresselhaus spin-orbit coupling can be gauged away, so the existence of the Raman field is essential in our discussions below. This is very different from the Rashba SOC in 2D or the Weyl SOC in 3D, where the non-abelian nature alone makes their effects nontrivial already. Chapter 3 has given a nice example. The coexistence of the SOC and the Raman field modifies the energy dispersions in a nontrivial way. The SOC shifts the quadratic energy bands sideway, and the Raman field, which is orthogonal to the SOC direction, opens a gap at the band crossings, please see Fig. 4.1. The gap is called a spin-orbit gap, which has been used in experiments to show the existing of spin-orbit coupling in a 1D quantum wire [67]. For large enough Ω, two energy minima will merge into a single minimum in the lowest energy band of the dispersion relation, please see Fig. 4.2. Defining the relative momentum and the

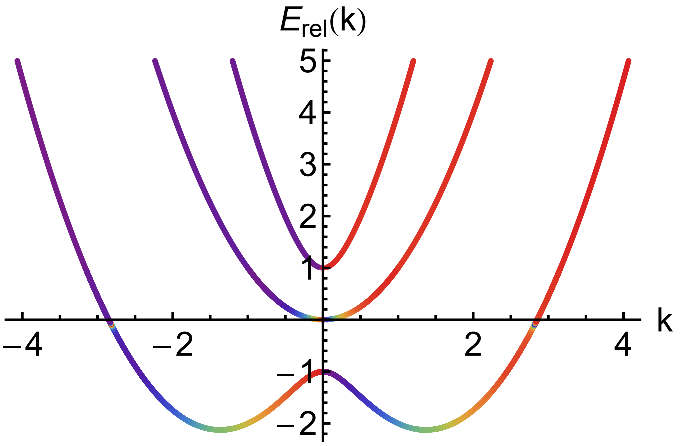

Figure 4.1.: The relative energy dispersions are color-coded with the transmission (reflection) coefficients at the quasi-momenta with positive (negative) group velocities assuming the incoming waves are selected to be the right-going waves. The parameters used here are $\hbar\Omega = 1 \times (2E_r)$, $\lambda = \sqrt{2} \times (k_r)$, $g_{1\text{D}} = -1 \times (2E_r/(\hbar k_r))$, and $\hbar\delta = 0 \times (2E_r)$ in the unit system of $\hbar = 1$, $m = 1$, and $k_r = 1$. With the definition, the energy unit is $2E_r$.

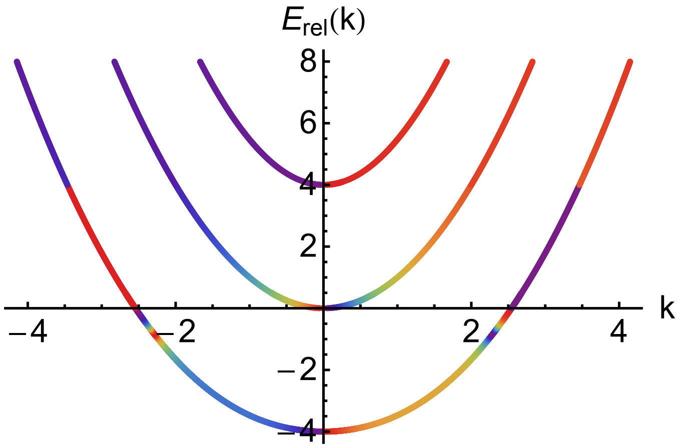

Figure 4.2.: The relative energy dispersions are color-coded with the transmission (reflection) coefficients on the positive (negative) k side. The parameters used here are $\Omega = 4 \times (2E_r)$, $\lambda = 1k_r$, $g_{1\text{D}} = -1 \times (2E_r/(\hbar k_r))$, and $\delta = 0E_r$ in the unit system of $\hbar = 1$, $m = 1$, and $k_r = 1$.

total momentum as $k = (k_2 - k_1)/2$ and $K = k_1 + k_2$, we can recast the Hamiltonian in Eq. (4.2) into the following expression,

$$H_{1\mathrm{D}} = \frac{\hbar^2 K^2}{2M} + \frac{\hbar^2 k^2}{2\mu} + \begin{pmatrix} 0 & \frac{\hbar^2\sqrt{2}k\lambda}{m} & -\frac{\hbar^2\sqrt{2}k\lambda}{m} & 0 \\ \frac{\hbar^2\sqrt{2}k\lambda}{m} & \hbar\Omega & 0 & \frac{\hbar^2 K\lambda}{\sqrt{2}m} + \frac{\hbar\delta}{\sqrt{2}} \\ -\frac{\hbar^2\sqrt{2}k\lambda}{m} & 0 & -\hbar\Omega & \frac{\hbar^2 K\lambda}{\sqrt{2}m} + \frac{\hbar\delta}{\sqrt{2}} \\ 0 & \frac{\hbar^2 K\lambda}{\sqrt{2}m} + \frac{\hbar\delta}{\sqrt{2}} & \frac{\hbar^2 K\lambda}{\sqrt{2}m} + \frac{\hbar\delta}{\sqrt{2}} & 0 \end{pmatrix} + V(x), \tag{4.3}$$

where the matrix is written in the singlet and triplet basis, which are defined as $\{|S\rangle, |T_1\rangle, |T_2\rangle, |T_3\rangle\} = \{(|\uparrow\downarrow\rangle - |\downarrow\uparrow\rangle)/\sqrt{2}, |\uparrow\uparrow\rangle, |\downarrow\downarrow\rangle, (|\uparrow\downarrow\rangle + |\downarrow\uparrow\rangle)/\sqrt{2}\}$. Also, remember that $M = 2m$ and $\mu = m/2$. These vectors form a complete basis for the Hilbert space of two spin-1/2 particles. However, if we move into the center of mass frame of the two colliding atoms (i.e. $K = 0$), the triplet channel, $|T_3\rangle$, could be decoupled from the rest three states in the zero detuning case. That is achieved by technically orthogonalizing the two degenerate two-body states, in which one atom locates in the bottom band and the other in the upper band of the one-body dispersion. Therefore, the dimension of the spin Hilbert space is nicely decreased into three.

Restricting ourselves to this subspace, the 1D Hamiltonian is simplified to be

$$H_{1\mathrm{D}} = \frac{\hbar^2 k^2}{2\mu} + \begin{pmatrix} 0 & \frac{\hbar^2\sqrt{2}k\lambda}{m} & -\frac{\hbar^2\sqrt{2}k\lambda}{m} \\ \frac{\hbar^2\sqrt{2}k\lambda}{m} & \hbar\Omega & 0 \\ -\frac{\hbar^2\sqrt{2}k\lambda}{m} & 0 & -\hbar\Omega \end{pmatrix} + V(x). \tag{4.4}$$

To help our calculations later, we list the non-interacting solution of the Hamiltonian in Eq. (4.4) here.

$$\Psi_1(x) = \frac{1}{2\sqrt{k^2 + \Delta^2}} \begin{pmatrix} -\sqrt{2}k \\ -(\sqrt{k^2+\Delta^2} + \Delta) \\ \sqrt{k^2+\Delta^2} - \Delta \end{pmatrix} e^{ikx} \tag{4.5}$$

$$\Psi_2(x) = \frac{1}{\sqrt{2(k^2+\Delta^2)}} \begin{pmatrix} -\sqrt{2}\Delta \\ k \\ k \end{pmatrix} e^{ikx} \tag{4.6}$$

$$\Psi_3(x) = \frac{1}{2\sqrt{k^2+\Delta^2}} \begin{pmatrix} \sqrt{2}k \\ -(\sqrt{k^2+\Delta^2}-\Delta) \\ \sqrt{k^2+\Delta^2}+\Delta \end{pmatrix} e^{ikx}, \tag{4.7}$$

where $\Delta = \Omega/(2\lambda)$. The corresponding eigenenergies are

$$E_1 = \hbar^2(k^2 + \sqrt{4k^2\lambda^2 + m^2\Omega^2/\hbar^2})/m, \tag{4.8}$$

$$E_2 = \hbar^2 k^2/m \tag{4.9}$$

$$E_3 = \hbar^2(k^2 - \sqrt{4k^2\lambda^2 + m^2\Omega^2/\hbar^2})/m. \tag{4.10}$$

Notice that the spinor parts of the full wave functions in Eq. (4.5)-(4.7) are orthogonal only at the same wave vector, k. For fixed energy, E, the spinors are *not* orthogonal. The orthogonality of the total wave function in different channels is brought back after a spatial integral of the plane wave function givening that

$$\int_{-\infty}^{\infty} dx e^{i(k_1-k_2)x} = 2\pi\delta(k_1-k_2). \tag{4.11}$$

The channel structure of the multichannel scattering in the presence of RD spin-orbit coupling and the Raman field is determined by (i) the relative incoming scattering energy, E, and (ii) the relative strength between $(\hbar k/m)\lambda$ and Ω. When the Raman coupling strength is stronger than $\Omega_c = 2\hbar\lambda^2/m$, the energy bands are in the single-minimum regime. In this regime, for $-\hbar\Omega < E < 0$, there are one open channel and two closed channels. For $0 < E < \hbar\Omega$, there are two open channels and one closed channel. For $E > \hbar\Omega$, all channels are open.

The channel structure becomes slightly more complex when the Raman strength is weaker than Ω_c (or it is equivalent to say when the RDSOC strength is significant). In this double-minimum regime, the channel structure is the same as in the single-minimum regime for $E > -\hbar\Omega$. However, the double-minimum scattering threshold,

$E_{\mathrm{t}}^{\mathrm{DM}} = \frac{-\hbar^2\lambda^2}{m} - \frac{m\Omega^2}{4\lambda^2}$, moves below the single minimum threshold, $E_{\mathrm{t}}^{\mathrm{SM}} = -\hbar\Omega$. Therefore, when $E_{\mathrm{t}}^{\mathrm{DM}} < E < -\hbar\Omega$, the double-minimum structure increases the number of open channels into two. The extra open channel indeed comes from the *nonexistence* of any solution of the upper band. The combined fourth-order equation of the most upper and lowest band always gives four algebraic solutions at any given real energy. It then becomes a matter of how these four solutions are distributed among these two bands.

In a 1D low-energy collision, the binary interaction can be well approximated by a contact delta potential with an effective coupling strength $g_{1\mathrm{D}}$. Assuming a 1D pseudo-potential, $V(x) = g_{1\mathrm{D}}\delta(x)|\mathrm{S}\rangle\langle\mathrm{S}|$, where S stands for the singlet state, the scattering amplitudes can be solved analytically by matching the solutions to the proper boundary conditions with the given channel structures plus the condition of the continuity of the wave function and its derivative except in the singlet component. The singlet component of the wave function experiences a first derivative discontinuity due to a delta-type potential.

For our calculation below, we consider the following initial condition, where there is only a single incident channel coming from the side of the negative infinity. Depending on the incoming energy, we might have multiple choices of the incoming (outgoing) channels, and this affects our definitions of the reflectivity and the transmitivity.

For single-channel scattering, the reflectivity, R, is defined as the ratio of the reflective flux to the incoming flux, $R = j_R/j_i$. In multi-channel scattering, R is found by summing over all (open) final states and averaging over all (open) initial states given multiple choices.

$$R \equiv \langle \sum_{f\in\mathrm{open}} \frac{j_{R,f}}{j_i} \rangle_i. \tag{4.12}$$

where i stands for initial and f for final. The transmitivity, T, has a similar definition by simply changing the reflective flux into the transmitted flux. One can verify that $R+T = 1$, which is guaranteed by the flux conservation. Since the spin-orbit coupling can be viewed as a spin-dependent vector potential, the current flux involves a term associated with the vector potential. The current flux for the states in Eq. (4.5)-(4.7) are

$$j_1 = \frac{\hbar}{m}\big(2k + \frac{4k\lambda^2}{\sqrt{4k^2\lambda^2 + m^2\Omega^2/\hbar^2}}\big) \tag{4.13}$$

$$j_2 = \frac{\hbar}{m}2k \tag{4.14}$$

$$j_3 = \frac{\hbar}{m}\big(2k - \frac{4k\lambda^2}{\sqrt{4k^2\lambda^2 + m^2\Omega^2/\hbar^2}}\big). \tag{4.15}$$

Noticing that the middle band has the usual quadratic dispersion relation, we simply get the familiar formula of the current flux for the free particle with a reduced mass, $\mu = m/2$.

In Fig. 4.3 and Fig. 4.9, the reflectivity is plotted against the scattering energy in the single-minimum (SM) and double-minimum (DM) regimes respectively. Rich scattering resonance structures are found when we scan over the real energy axis. At zero energy, there is a total reflection in both SM and DM cases. This is expected as in the usual scattering without SOC since the incident energy is too weak for particles to pass through (matches our classical intuition). The more interesting resonances happen when the incident energy is below zero. Therefore, we extract the peak positions of the total reflection as a function of the 1D interaction strength, g_{1D}, in the energy range between $[-\Omega, 0]$ in Fig. 4.8(a) and Fig. 4.12(a). The total reflection shows up as a result of a resonance when the scattering state energy coincides with the energy of the quasi-bound state splitting off from the higher close bands. For some parameter range, there may exist simultaneously two quasi-bound states since two of the higher closed bands all have the singlet component except the middle branch at $k = 0$, see Fig. 4.4. Recall that the SOC has no effect at $k = 0$, the three stationary states from the highest to the lowest band are $|T_1\rangle$, $|S\rangle$ and $|T_2\rangle$ respectively.

For the discussion below, we choose the unit system with $\hbar \equiv 1$, $m \equiv 1$, and the recoil momentum $k_r = 2\pi/\lambda_{\text{Laser}} \equiv 1$. Therefore, the energy unit is $2E_r$, where $E_r = \hbar^2 k_r^2/2m$ is the recoil energy. For instance, when we say $\Omega = 2$, what it means is $\Omega = 4E_r$. From the conventional wisdom, we know that no matter how weak the attraction is, there is always a bound state in 1D. This explains the existence of a resonance

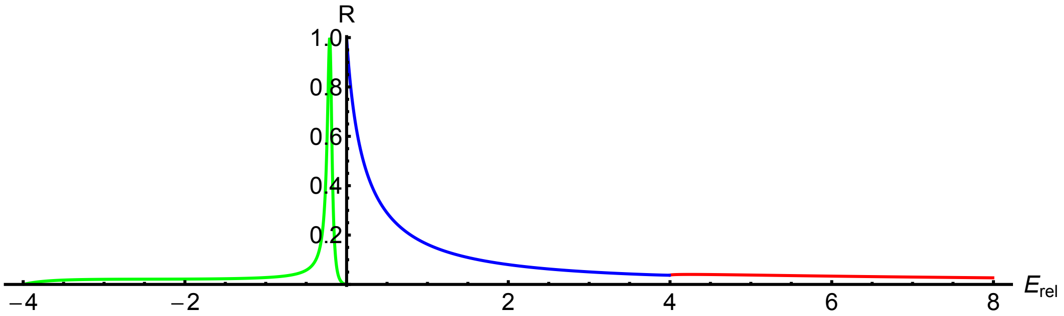

Figure 4.3.: The reflection coefficient plot as a function of the two-body relative energy for $g = -1$, $\Omega = 4$ and $\lambda = 1$ with $\hbar = 1$ and $m = 1$. The region with the green (blue,red) curve stands for the case with only one (two,three) open channel(s).

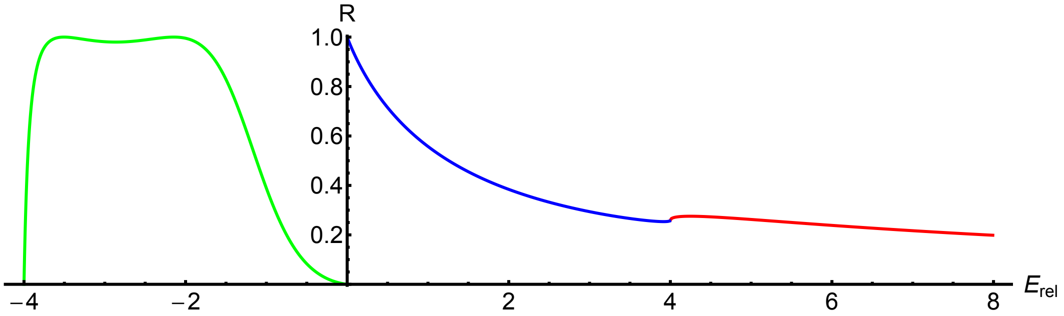

Figure 4.4.: The reflection coefficient plot as a function of the two-body relative energy for $g = -3$, $\Omega = 4$, $\lambda = 1$ with $\hbar = 1$ and $m = 1$. The region with the green (blue,red) curve stands for the case with only one (two,three) open channel(s).

in Fig. 4.8(a) for the weakly-interacting region. For instance, it is located between $-2.7 < g_{1\text{D}} < 0$ in the case of $\Omega = 4$. As we keep increasing $g_{1\text{D}}$, the second resonance peak appears when $-3.2 < g_{1\text{D}} < -2.7$ for $\Omega = 4$ (PS: check what the accurate number is). The second resonance peak is due to the quasi-bound state formed by the upper most band with a *non*-quadratic dispersion relation. This deviation from the usual quadratic band makes the quasi-bound state behave abnormally. First of all, it shows up only when the attraction is strong enough and the Raman coupling is

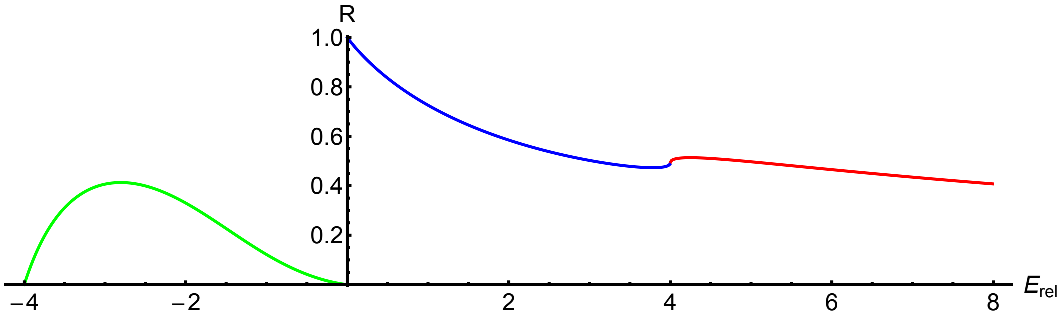

Figure 4.5.: The reflection coefficient plot as a function of the two-body relative energy for $g = -5$, $\Omega = 4$, and $\lambda = 1$ with $\hbar = 1$ and $m = 1$. The region with the green (blue,red) curve stands for the case with only one (two,three) open channel(s).

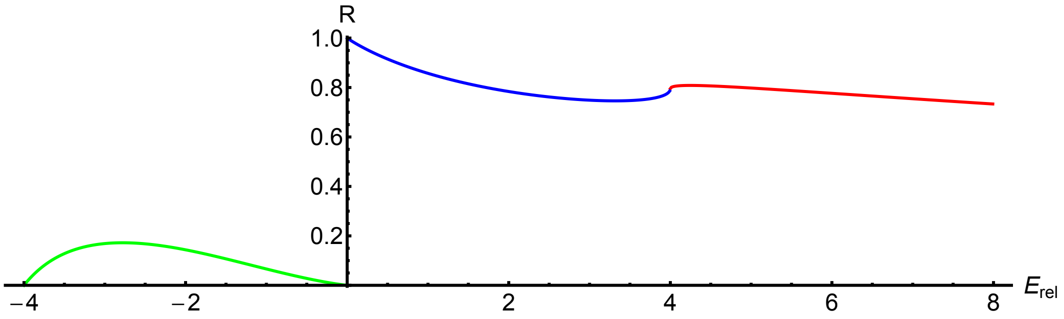

Figure 4.6.: The reflection coefficient plot as a function of the two-body relative energy for $g = -10$, $\Omega = 4$, and $\lambda = 1$ with $\hbar = 1$ and $m = 1$. The region with the green (blue,red) curve stands for the case with only one (two,three) open channel(s).

not too strong. When Ω is too big, the second resonance disappears, see the purple line in Fig. 4.8(b). Secondly, the stronger attraction indeed leads to a weaker quasi-bound state in the upper band. Moving to the double-minimum regime, we find very different physics. In Fig. 4.12(a), we see that there is always only a resonance peak and the peak position is never asymptotically approaching $E = -\Omega$ no matter how strong the attraction is. Our understanding to it is because the upper band does not have a solution (or become *transparent*) when energy goes below $E_{24} = -m\Omega^2/(4\lambda)$,

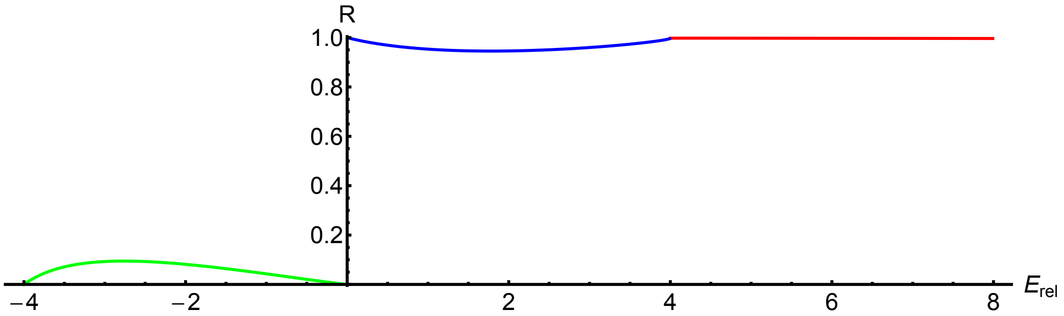

Figure 4.7.: The reflection coefficient plot as a function of the two-body relative energy for $g = -100$, $\Omega = 4$, and $\lambda = 1$ with $\hbar = 1$ and $m = 1$. The region with the green (blue,red) curve stands for the case with only one (two,three) open channel(s).

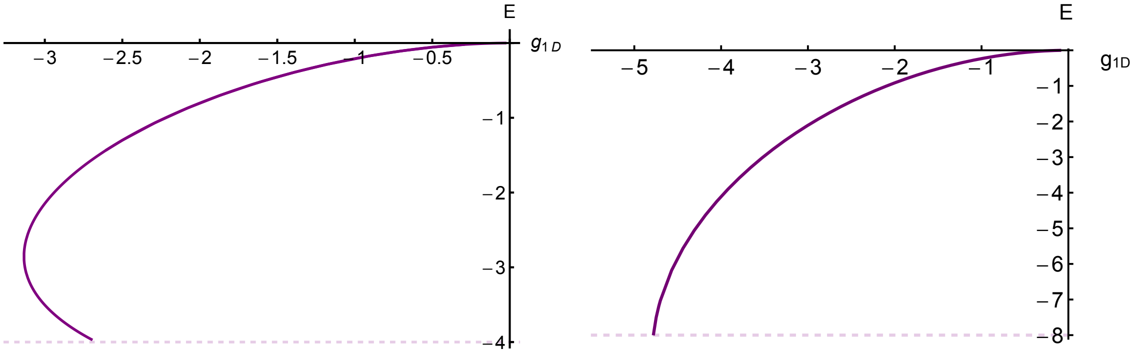

(a) $\Omega = 4$ and $\lambda = 1$

(b) $\Omega = 8$ and $\lambda = 1$

Figure 4.8.: The positions of the energy, where total reflection occurs, is shown as a function of the 1D interaction strength in the single-minimum regime.

in which four out of six solutions in k come from the lowest band. Thus, before the interaction is attractive enough to support a bound state, the upper band has become transparent already. Therefore, no two resonance peaks at the same g_{1D} could be found simultaneously in the DM regime.

Comparing the scattering behaviors when the incident energy is at the lowest scattering threshold in the SM and DM cases, a striking difference is found. For the SM case, there is total transmission; however, for the DM case, there is a total

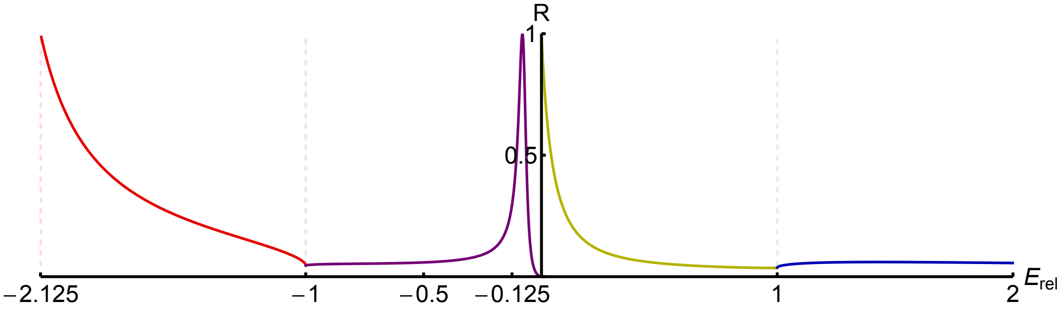

Figure 4.9.: The reflection coefficient plot as a function of the two-body relative energy for $g = -1$, $\Omega = 1$, and $\lambda = \sqrt{2}$ with $\hbar = 1$ and $m = 1$. The region with the red (purple, green, blue) curve stands for the case with only two (one, two, three) open channel(s).

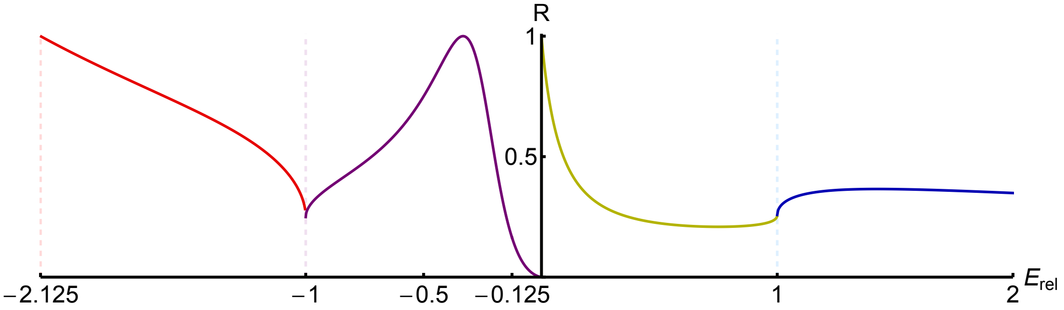

Figure 4.10.: The reflection coefficient plot as a function of the two-body relative energy for $g = -3$, $\Omega = 1$, and $\lambda = \sqrt{2}$ with $\hbar = 1$ and $m = 1$. The region with the red (purple, green, blue) curve stands for the case with only two (one, two, three) open channel(s).

reflection. We think this is related with the fact that we need a minimum attraction to form a true two-body bound state in the SM regime, but not in the DM regime, see Fig. 4.13(a) and 4.13(b).

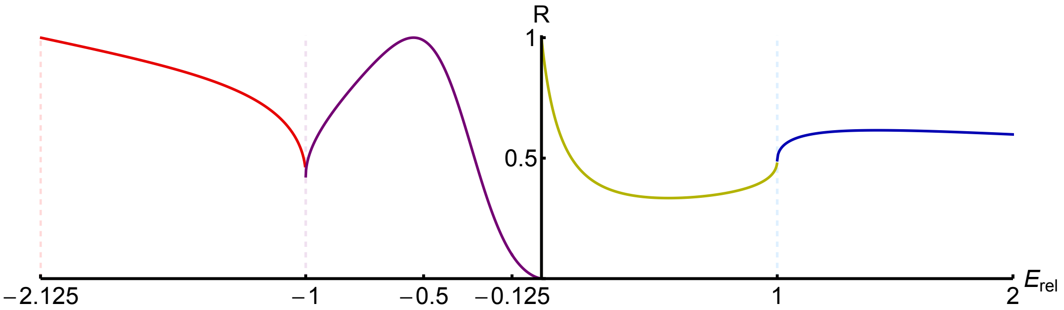

Figure 4.11.: The reflection coefficient plot as a function of the two-body relative energy for $g = -5$, $\Omega = 1$, and $\lambda = \sqrt{2}$ with $\hbar = 1$ and $m = 1$. The region with the red (purple, green, blue) curve stands for the case with only two (one, two, three) open channel(s).

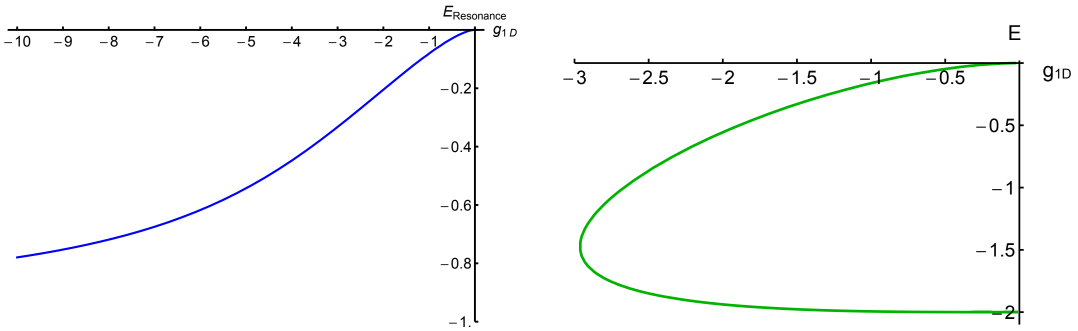

(a) $\Omega = 4$ and $\lambda = 1$

(b) $\Omega = \Omega_c$

Figure 4.12.: The positions of the total reflection as a function the 1D interaction strength in (a) the double-minimum regime and (b) the critical Ω value with the quartic dispersion.

4.2 Confinement-induced resonance in RD SOC BECs

We derive the effective 1D interaction strength (g_{1D}) under a strong transverse confinement in the presence of SOC and Raman fields. We first derive the Green's function and then derive g_{1D} by integrating out the excited transverse states. The derivation in this section is based on the literature [68].

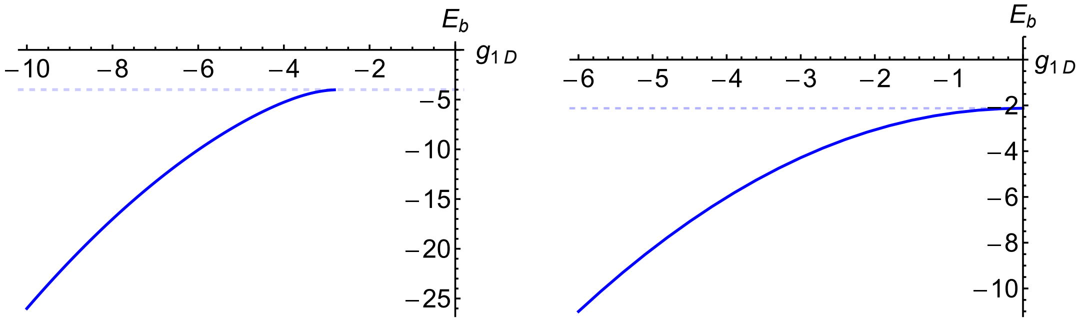

(a) $\Omega = 4$ and $\lambda = 1$ (b) $\Omega = 1$ and $\lambda = \sqrt{2}$

Figure 4.13.: Plots of bound state energies as a function of the 1D interaction strength in different regimes.

4.2.1 Quasi-one-dimensional scattering length

Atom-atom interactions are strongly affected by the external condition. BECs and DFGs are usually confined in trapping potentials, which could be either of magnetic origin or of optical origin. If the harmonic confinements are much stronger in two spatial dimensions (the transverse direction or $\hat{\rho}$) than in the third dimension (the longitudinal direction, or $\hat{x}$), we create an effective one-dimensional system in the direction of the weak confinement if the temperature/chemical potential of the system is low enough not to excite any transverse motions, i.e. $E_x < 2\hbar\omega_\perp$.

Under such conditions, if two atoms collide, they would behave like in one dimension kinematically. The effective 1D scattering length could be derived by first assuming the transverse state stay in the ground state of the transverse harmonic trap and then integrating out the transverse motion. Expressing the Hamiltonian as

$$H = H_{\text{com}} - \frac{\hbar^2}{2\mu}\left(\frac{\partial^2}{\partial x^2} + \frac{\partial^2}{\partial \rho^2}\right) + \frac{1}{2}\mu\omega_\perp^2\rho^2 + V(x, y, z), \tag{4.16}$$

where the reduced mass $\mu = (1/m_1 + 1/m_2)^{-1} = m/2$ and $\omega_\perp$ is the transverse trapping (angular) frequency. A good ansatz to the solution of the 3D Schrödinger equation in Eq. (4.16) is $\Psi(x, y, z) = \psi(x)\phi^{0,0}(\rho)$, where $\phi^{0,0}(\rho)$ is the ground state of the 2D harmonic oscillator with energy $E_\perp = \hbar\omega_\perp$. The subscripts label the quantum numbers, n_y and n_z (or equivalently n and m_z depending on the choice of coordinates). Plug in the ansatz, and sandwich from the left-hand side with the conjugate wave function of $\phi^{0,0}(\rho)$, we get

$$-\frac{\hbar^2}{2\mu}\frac{\partial^2}{\partial x^2}\psi(x) + g_{1D}\delta(x)\psi(x) = (E - E_\perp)\psi(x), \tag{4.17}$$

where $g_{1D} = g_{\mathrm{3D}}|\phi^{0,0}(0)|^2 = g_{\mathrm{3D}}/(\pi a_\perp^2)$ with the 3D interaction strength $g_{\mathrm{3D}} = \frac{2\pi\hbar^2 a_s}{\mu}$. From the above argument, we would intuitively think the effective 1D interaction strength is merely modified by a constant determined by the the transverse ground state wave function. This is true only when we are away from resonances. If the higher transverse modes can hold a quasi-bound state in the system, then it would cause a resonance phenomenon in the 1D interaction strength when the scattering energy is close to the energy of the quasi-bound state supported by the higher transverse modes. This is called confinement-induced resonance (CIR). We would simply write down the effective 1D interaction strength formula here without deriving it. For interested readers, we appoint them to the following references [69] [70].

$$g_{\mathrm{1D}} = \frac{2\hbar^2 a_s}{\mu a_\perp^2}\frac{1}{1 - Ca_s/a_\perp}, \tag{4.18}$$

where $C \approx 1.4603$ and $a_\perp = \sqrt{\frac{\hbar}{\mu\omega_\perp}}$ (a_s is the 3D background scattering length). g_{1D} diverges as $a_s/a_\perp = 1/C \approx 0.68$. The tunability of 1D interaction strength to positive infinity ($g_{\mathrm{1D}} \to \infty$) opens the possibility to realize the 1D impenetrable boson gas, or the Tonks-Girardeau (TG) gas [71]. In the opposite site, $g_{\mathrm{1D}} \to -\infty$ contributes to the realization of a super Tonks-Girardeau (s-TG) gas [72][73].

4.2.2 Free 3D Green's function

In this subsection, we are going to derive the effective 1D interaction strength under the condition of a strong transverse confinement. The assumptions we make here are (i) the two-body interaction is captured by the regularized s-wave Fermi pseudopotential $V(r) = |s\rangle\langle s|\frac{4\pi\hbar^2 a_s}{m}\delta(\vec{r})\frac{\partial}{\partial r}(r) \equiv |s\rangle\langle s|g_{\mathrm{3D}}\delta(\vec{r})\frac{\partial}{\partial r}(r)$, and (ii) the transverse

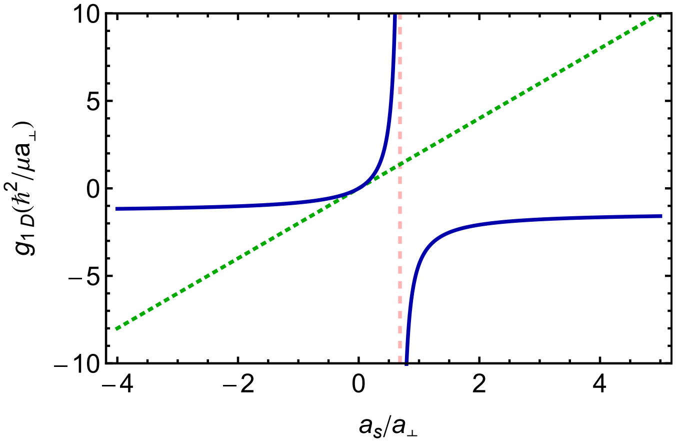

Figure 4.14.: Effective 1D interaction strength as a function of the 3D background scattering length. The dashed pink line labels the position of CIR, whose value is around $1/C \approx 0.68$. The dotted green line depicts $g_{\rm 1D}$ in the absence of resonance, which is linearly proportional to $a_{\rm s}$ as expected.

motion is in its ground state. To satisfy condition (ii), it is required that the kinetic energy in the longitudinal direction cannot exceed the energy gap between the transverse ground state and the first excited state, which is $2\hbar\omega_\perp$.

In the following, we will start from the 3D Lippmann-Schwinger equation and derive an effective 1D solution from that. The effective 1D interaction strength could be extracted out by comparing the effective 1D solution with the true 1D solution. Since we don't have any good quantum number in the free RD-SOC Hamiltonian except the center-of-mass momentum and the relative momentum, we would not go to the subspace of the total angular momentum like we do when dealing with the Weyl SOC in Ch. 3. Here, it is more advantageous to tackle the problem in the momentum space and then Fourier transform the solution back to the real space. Also, due to the translational invariance, the Green's function satisfies $G_{\rm 3D}(\epsilon, \vec{r}, \vec{r}') = G_{\rm 3D}(\epsilon, \vec{r} - \vec{r}')$, so we can simply take $\vec{r}' = 0$ in our derivations. The three-dimensional free Green's function describing the RD-SOC system is

$$G_{\mathrm{3D}}(\epsilon, x, y=0, z=0) = \langle x, 0, 0| \frac{1}{\epsilon - \hat{H} + i\eta} |0, 0, 0\rangle. \tag{4.19}$$

Notice that the motion in the y and z direction remain the same, we could choose y and z coordinates to be zero without loss of generosity. Separating the non-interacting Hamiltonian into two parts: $H = H_0 + H_\perp$,

$$G_{\mathrm{3D}}(\epsilon, x, y=0, z=0) = \langle x, 0, 0| \frac{1}{\epsilon - (\hat{H}_0 + \hat{H}_\perp) + i\eta} |0, 0, 0\rangle. \tag{4.20}$$

Inserting a complete set into Eq. (4.20),

$$\begin{aligned} & G_{\mathrm{3D}}(\epsilon, x, y=0, z=0) \\ &= \sum_{m,k,n_y,n_z} \langle x, 0, 0|m, k, n_y, n_z\rangle\langle m, k, n_y, n_z| \frac{1}{\epsilon - (\hat{H}_0 + \hat{H}_\perp) + i\eta} |m, k, n_y, n_z\rangle\langle m, k, n_y, n_z|0, 0, 0\rangle \\ &= \sum_{m,k,n_y,n_z} \langle x, 0, 0|m, k, n_y, n_z\rangle \frac{1}{\epsilon - [E_m(k) + (n_x + n_y + 1)\hbar\omega_\perp] + i\eta} \langle m, k, n_y, n_z|0, 0, 0\rangle \end{aligned} \tag{4.21}$$

where $|m, k, n_y, n_z\rangle \equiv |m, k\rangle|n_y, n_z\rangle$ with $|m, k\rangle$ ($E_m(k)$) the eigenstates (eigenenergies) of the 1D RD-SOC Hamiltonian (see Eq. (4.5)-(4.7)) and $|n_y, n_z\rangle$ the solution of a 2D harmonic oscillator. This complete set is a solution of the non-interacting Hamiltonian in momentum space, so it reduces the inverse operator into a regular expression of a function.

Next, we separate the Green's function into two parts: one with the transverse motion in its ground state and the other one carries the rest higher energy states. The second part actually captures all the virtual transitions during the collision processes, in which the excited states could be accessed via two-body collisions. Therefore, we expect the resonance condition to come form $G_{\mathrm{3D},2}$.

$$G_{\mathrm{3D}}(\epsilon, x, y=0, z=0) = G_{\mathrm{3D},1}(\epsilon, x, y=0, z=0) + G_{\mathrm{3D},2}(\epsilon, x, y=0, z=0), \tag{4.22}$$

with

$$G_{\rm 3D,1}(\epsilon, x, y=0, z=0) = \sum_{m,k} \langle x,0,0|m,k,0,0\rangle \frac{1}{\epsilon - (E_m(k)+\hbar\omega_\perp)+i\eta} \langle m,k,0,0|0,0,0\rangle, \text{ and} \tag{4.23}$$

$$G_{\rm 3D,2}(\epsilon, x, y=0, z=0) = \sum_{\substack{m,k\\ n_y,n_z\neq 0}} \langle x,0,0|m,k,n_y,n_z\rangle \frac{1}{\epsilon - [E_m(k)+(n_x+n_y+1)\hbar\omega_\perp]+i\eta} \langle m,k,n_y,n_z|0,0,0\rangle. \tag{4.24}$$

The solutions of a 1D harmonic oscillator are well-known results, which are

$$\langle y|n_y\rangle = \phi_{n_y}(y) = \left(\frac{\mu\omega_\perp}{\pi\hbar 2^{2n_y}(n_y!)^2}\right)^{1/4} \exp\Big(-\frac{\mu\omega_\perp y^2}{2\hbar}\Big) H_{n_y}\left[(\frac{\mu\omega_\perp}{\hbar})^{1/2} y\right] \tag{4.25}$$

$$\text{with } E_y = (n_y + \frac{1}{2})\hbar\omega_\perp, \tag{4.26}$$

where $H_n(y)$ are the Hermite polynomials. The length scale of the transverse trapping potential is conveniently defined as $a_\perp = (\frac{\hbar}{\mu\omega_\perp})^{1/2}$. Rewriting the harmonic solution in terms of the trap length scale,

$$\langle y|n_y\rangle = \phi_{n_y}(y) = \left(\frac{1}{\sqrt{\pi}2^{n_y}n_y!a_\perp}\right)^{1/2} \exp\Big(-\frac{y^2}{2a_\perp^2}\Big) H_{n_y}(y/a_\perp). \tag{4.27}$$

The solution, $\phi_{n_z}(z)$, can be found by replacing y with z. Plug into Eq. (4.23) and Eq. (4.24), we simplify $G_{\rm 3D,1}$ and $G_{\rm 3D,2}$ into

$$G_{\rm 3D,1}(\epsilon, x, 0, 0) = \sum_{m,k} |\phi_0(0)|^4 \frac{\langle x|m,k\rangle\langle m,k|0\rangle}{\epsilon - (E_m(k)+\hbar\omega_\perp)+i\eta} \text{ and} \tag{4.28}$$

$$G_{\rm 3D,2}(\epsilon, x, 0, 0) = \sum_{\substack{m,k\\ n_y,n_z\neq 0}} |\phi_{n_y}(0)|^2|\phi_{n_z}(0)|^2 \frac{\langle x|m,k\rangle\langle m,k|0\rangle}{\epsilon - (E_m(k)+(n_x+n_y+1)\hbar\omega_\perp)+i\eta} \tag{4.29}$$

From Eq. (4.28), we see that the function $G_{\rm 3D,1}$ is simply the one-dimensional Green's function for H_0 multiplied by a constant, $|\phi_0(0)|^4$, with a shifted energy origin by $\hbar\omega_\perp$.

For convenience, we would redefine our energy origin by shifting $\epsilon \to (\epsilon - \hbar\omega_\perp)$. By doing that, the zero of the energy, ϵ, agrees with the zero of the 1D system described by H_0.

Calculations of $G_{\mathrm{3D},2}$ require more attentions. Using the identity,

$$\frac{1}{n} = \int_0^\infty dt \exp(-nt) \text{ for } n > 0 \tag{4.30}$$

we transform the denominator into the exponent of an exponential function. For convenience, we use the trap energy as the energy unit, and rewrite the integral in the dimensionless format,

$$G_{\mathrm{3D},2}(\tilde{\epsilon}, x, y=0, z=0) = \\ -\sum_{m,k,n_y\neq 0,n_z\neq 0} \int_0^\infty \frac{dt}{\hbar\omega_\perp} |\phi_{n_y}(0)|^2 |\phi_{n_z}(0)|^2 e^{-(\tilde{E}_m(k)+n_y+n_z-\tilde{\epsilon})t} \langle x|m,k\rangle\langle m,k|0\rangle, \tag{4.31}$$

where the notation, $\sim$, denotes that variables are scaled to the trap unit. The summation over n_y and n_z can be performed with the assistance of the completeness identity of Hermite polynomials,

$$\sum_{n=0}^\infty \frac{1}{n!}\Big(\frac{t}{2}\Big)^n H_n(y)H_n(z) = (1-t^2)^{-1/2} \exp\left[\frac{2yzt - (y^2+z^2)t^2}{1-t^2}\right]. \tag{4.32}$$

To use the identity, we first complete the summation with missing terms from $n_y = 0$ and $n_z = 0$, applying the identity, and then subtract back the $n_y = 0$ and $n_z = 0$ terms, then we arrive at

$$\begin{aligned} & G_{\mathrm{3D},2}(\epsilon, x, y=0, z=0) \\ &= -\sum_{m,k} \int_0^\infty \frac{dt}{\hbar\omega_\perp} e^{-(E_m(k)-\epsilon)t} \left(\frac{1}{\sqrt{\pi}a_\perp}\right)^2 \left[\left(\frac{1}{\sqrt{1-e^{-2t}}}\right)^2 - 1\right] \langle x|m,k\rangle\langle m,k|0\rangle \\ &= -\frac{1}{\pi a_\perp^2} \sum_{m,k} \int_0^\infty \frac{dt}{\hbar\omega_\perp} e^{-(E_m(k)-\epsilon)t} \left(\frac{1}{e^{2t}-1}\right) \langle x|m,k\rangle\langle m,k|0\rangle \end{aligned} \tag{4.33}$$

Starting from Eq. (4.33), we will omit the notation, $\sim$, for simplicity. Keep in mind that the dimensionless numbers are scaled to the trap unit. As we have already seen in Sec. 3.3 or will see in the next subsection, the interacting wave function depends only on the {1,1} component of the free Green's function under the s-wave assumption. Thus, only $(G_{3\mathrm{D},2})_{11}$ is calculated below.

$$\begin{aligned}
&(G_{3\mathrm{D},2})_{11}(\epsilon, x, y=0, z=0)\\
&= -\frac{1}{2\pi a_\perp^2}\int_0^\infty \frac{dt}{\hbar\omega_\perp}\int_{-\infty}^{\infty}\frac{dk}{2\pi\frac{a_\perp}{\sqrt{2}}}e^{ikx}\frac{e^{-\frac{k^2t}{2}}e^{\frac{\epsilon t}{2}}}{e^t-1}\left(\frac{\Delta^2}{k^2+\Delta^2}+\frac{k^2}{k^2+\Delta^2}\cosh(\lambda\sqrt{k^2+\Delta^2}t)\right)\\
&\equiv \chi_1+\chi_2 \qquad (4.34)
\end{aligned}$$

with

$$\chi_1 = -\frac{\sqrt{2\pi}}{2\sqrt{2}\pi^2 a_\perp^3\hbar\omega_\perp}\int_0^\infty dt e^{\epsilon t/2}\frac{1}{\sqrt{t}(e^t-1)} \quad \text{and} \qquad (4.35)$$

$$\chi_2 = -\frac{1}{2\sqrt{2}\pi^2 a_\perp^3\hbar\omega_\perp}\int_0^\infty dt\frac{e^{\epsilon t/2}}{e^t-1}\int_{-\infty}^{\infty}dk e^{ikx}\frac{k^2}{k^2+\Delta^2}\left(\cosh(\lambda\sqrt{k^2+\Delta^2}t)-1\right)e^{-k^2t/2}. \qquad (4.36)$$

Notice that in Eq. (4.34), the momentum k is scaled to the trap unit, $(a_\perp/\sqrt{2})^{-1}$. Any other matrix elements of the free Green's function could be calculated in a similar way.

4.2.3 Effective 1D interaction strength

Following the same procedures in Sec. 3.3, the 3D interacting solution with the regularized s-wave pseudo potential could be found as follows.

$$\Psi_{3\mathrm{D}}(x,y,z) = \Psi_{3\mathrm{D},0}(x,y,z) + \frac{g_{3\mathrm{D}}(\Psi_{3\mathrm{D},0}(0,0,0))_{11}}{1-g_{3\mathrm{D}}(G_{3\mathrm{D}}(0,0,0))_{r,11}}\begin{pmatrix}(G_{3\mathrm{D}}(x,0,0))_{11}\\(G_{3\mathrm{D}}(x,0,0))_{21}\\(G_{3\mathrm{D}}(x,0,0))_{31}\end{pmatrix}, \qquad (4.37)$$

where the reduced function is defined as $G_{3\mathrm{D},0}(0,0,0)_r \equiv \lim_{r\to 0}\partial_r(rG_{3\mathrm{D},0}(x,y,z)$. Under the strong transverse confinement, it is reasonable to postulate $\Psi_{3\mathrm{D}}(x,y,z) =$

$\Psi(x)\phi_0(y)\phi_0(z)$. So the quasi-one-dimensional (Q1D) interacting solution derived from Eq. (4.37) can be expressed as

$$\Psi_{\mathrm{Q1D}}(x) = \Psi_{\mathrm{Q1D},0}(x) + \frac{g_{\mathrm{3D}}(\Psi_{\mathrm{Q1D},0}(0))_{11}}{1 - g_{\mathrm{3D}}(G_{\mathrm{3D}}(0,0,0))_{r,11}} \begin{pmatrix} (G_{\mathrm{3D}}(x,0,0))_{11} \\ (G_{\mathrm{3D}}(x,0,0))_{21} \\ (G_{\mathrm{3D}}(x,0,0))_{31} \end{pmatrix}, \tag{4.38}$$

where $\Psi_{\mathrm{Q1D}}(x) \equiv \Psi_{\mathrm{3D}}(x)/(\phi_0(y)\phi_0(z))$. Comparing it with the true interacting 1D solution,

$$\Psi_{\mathrm{1D}}(x) = \Psi_{\mathrm{1D},0}(x) + \frac{g_{\mathrm{1D}}(\Psi_{\mathrm{1D},0}(0))_{11}}{1 - g_{\mathrm{1D}}(G_{\mathrm{1D}}(0))_{r,11}} \begin{pmatrix} (G_{\mathrm{1D}}(x))_{11} \\ (G_{\mathrm{1D}}(x))_{21} \\ (G_{\mathrm{1D}}(x))_{31} \end{pmatrix}, \tag{4.39}$$

the effective 1D interacting strength can be extracted out from the equality

$$\frac{g_{\mathrm{3D}}(\Psi_{\mathrm{Q1D},0}(0))_{11}}{1 - g_{\mathrm{3D}}(G_{\mathrm{3D}}(0,0,0))_{r,11}} \approx \frac{g_{\mathrm{1D}}(\Psi_{\mathrm{1D},0}(0))_{11}}{1 - g_{\mathrm{1D}}(G_{\mathrm{1D}}(0))_{r,11}} |\phi_0(0)|^4. \tag{4.40}$$

Remember that the 3D Green's function at $x \to \infty$ is differed from the 1D Green's function by the function $|\phi_0(0)|^4$. Therefore,

$$g_{\mathrm{1D}} = \frac{g_{\mathrm{3D}}|\phi_0(0)|^4}{1 - g_{\mathrm{3D}}(\chi_{1,r}(0) + \chi_2(0))}, \tag{4.41}$$

where the subscript, r, in χ_{1r} stands for *reduced*, in which the divergent part has been subtracted out from the integral.

$$\chi_{1r} = -\frac{\sqrt{2\pi}}{2\sqrt{2}\pi^2 a_\perp^3 \hbar\omega_\perp} \int_0^\infty dt \left(\frac{e^{\epsilon t/2}}{\sqrt{t}(e^t - 1)} - \frac{1}{t^{3/2}} \right), \tag{4.42}$$

where the integral part of χ_{1r} is related with the integral representation of the Hurwitz zeta function, -$\zeta(1/2, 1 - \epsilon/2)$ [cite]. To best compare the formula modified by SOC with the old one, we rewrite the formula of g_{1D} in two dimensionless integrals, C_1 and C_2. Therefore,

$$g_{\mathrm{1D}} = \frac{2\hbar^2 a_s}{\mu a_\perp^2} \frac{1}{1 - (C_1 + C_2) a_s / a_\perp}, \tag{4.43}$$

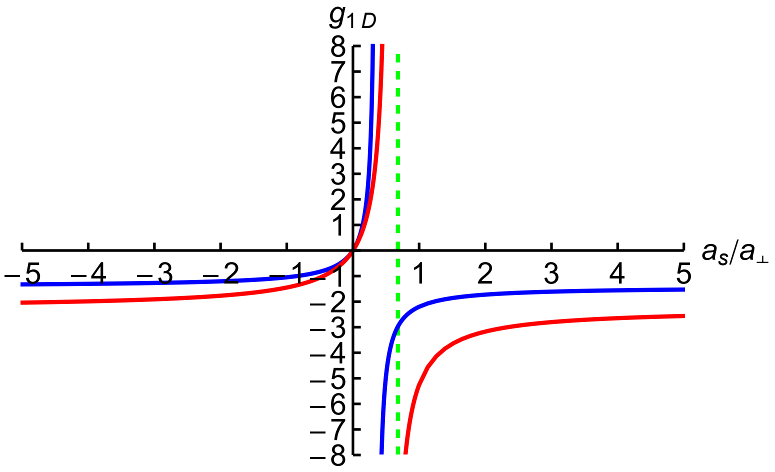

Figure 4.15.: The effective 1D interaction strength under the influence of the RD-SOC. The parameter used is $\Omega = 4\hbar\omega_\perp$. The blue curve denotes $g_{1\mathrm{D}}$ at the lowest scattering energy ($E = -4\hbar\omega_\perp$). The red curve depicts $g_{1\mathrm{D}}$ at the highest possible scattering energy ($E = -2\hbar\omega_\perp$) to ensure the assumption of the strong transverse confinement. The green dashed line labels the position of conventional CIR position ($a_s/a_\perp = 0.68$). We see the existence of Raman lasers modifies the CIR position.

where

$$C_1 = -\frac{1}{\sqrt{\pi}}\int_0^\infty dt\left(\frac{e^{\epsilon t/2}}{\sqrt{t}(e^t-1)} - \frac{1}{t^{3/2}}\right) = -\zeta(\frac{1}{2}, 1-\frac{\epsilon}{2}) \quad \text{and} \tag{4.44}$$

$$C_2 = -\frac{1}{\sqrt{2\pi}}\int_0^\infty dt\frac{e^{\epsilon t/2}}{e^t-1}\int_{-\infty}^\infty dk\frac{k^2}{k^2+\Delta^2}\left(\cosh(\lambda\sqrt{k^2+\Delta^2}t)-1\right)e^{-k^2t/2}. \tag{4.45}$$

A quick check on the validity of the above formula is by taking $\lambda \to 0$. In this case, $C_2 = 0$ and $C_1 \approx 1.4603$ at the lowest threshold energy, $\epsilon = 0$, which returns back to Olshanii's result [69].

Fig. 4.15 shows the effective 1D interaction strength as a function of the 3D background scattering length. We observe that the existence of the Raman lasers shifts the resonance position to the left at the lowest scattering threshold. This is encouraging from the experimental point of view. Since it means that for the same a_s we need less stronger trapping frequencies to reach resonance. Furthermore, we plot how the resonance position changes as a function of Ω in Fig. 4.16. It shows that by increasing the value of Raman coupling strengths, we significantly reduce the requirement in the trapping frequency. However, increasing the Raman coupling strength causes heating problems.

One comment on Fig. 4.16 is that when $\Omega = 0$, $a_s/a_\perp = 0.68$, which is the normal CIR position. This is because when the Raman laser is off, the RD-SOC in the effective 1D system could be gauged away by a unitary transformation. So we don't expect any change in the resonance position.

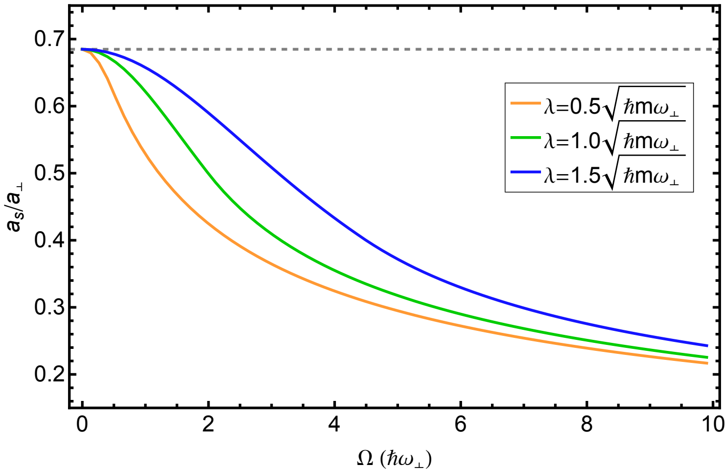

Figure 4.16.: The effective 1D interaction strength as a function of the Raman coupling strength at different RD-SOC strengths. When $\Omega = 0$, we return back to the normal CIR case, which is marked by the gray dashed line.

4.3 Estimation of experimental parameters

In this section, we estimate the parameter necessary for the experiments with potassium-40, which is one common example used for spin-1/2 fermionic gases. ^{40}K has a background scattering length, $a_s \approx 9$ nm. From [33], we learn that the spin-orbit strength is around the order of $\sqrt{\hbar m\omega_\perp}$, whose prediction is provided by the green curve in Fig. 4.16. The corresponding value of $a_s/a_\perp$ at a fixed Ω can be found once the transverse trap frequency is given. If we use $\omega_\perp \approx 70$ kHz, which is the number being realized in 2D optical lattice experiments [5], we find CIR position occurs at $a_s/a_\perp = 0.11$, and it could be approached by increasing the Raman intensity to 2.8 MHz. So far, the maximum Raman intensity that being explored in experiments [74] is around 40×3.7 kHz=148 kHz. The potential issue with a large Raman laser intensity is heating from spontaneous emission. The spontaneous emission rate scales as $W\Gamma/\Delta^2$, where W is the laser intensity, Γ is the linewidth of the excited states, and Δ is the detuning, please see Fig. 4.17. Also remember that the spin-flipped Raman process is proportional to $W\Delta_{FS}/\Delta^2$, where Δ_{FS} is the fine structure splitting, please refer to Fig. 4.17 again. So a smaller ratio of Γ/Δ_{FS} would help decrease the heating rate. This ratio is often larger for lighter elements, so choosing atomic species properly would help reduce the problem. For instance, comparing the three atomic species, which have been used in experiments, rubidium-87 is more favorable than potassium-40, and potassium-40 is more advantageous than lithium-6. More details can be found in [75] and the supplementary material in [76].

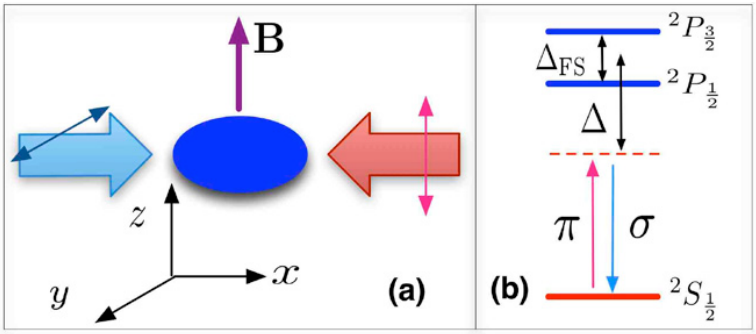

Figure 4.17.: (a) Typical Raman coupling scheme to generate spin-orbit coupling in ultracold atoms. (b)The atomic energy levels for the a two-photon Raman transition in alkali atoms. Pictures taken from [77].

To probe the resonance above the lowest scattering threshold but still under the limit set by the quasi-1D approximation, we need to apply a even higher trap frequency. The upper limit of a potentially achievable trap frequency in magnetic chip traps or optical dipole traps is predicted to be around the order of several MHz [78], which is promising.

4.4 Conclusions

In this chapter, we have studied the scattering processes in spin-orbit coupled systems with reduced dimensionalities. Scattering resonances are found whenever the scattering energies match either scattering thresholds or quasi-bound states supported by upper closed bands. Estimation of the experimental parameters are provided to assist the observation of these resonances. The capability of realizing either a perfect reflection or a perfect opaqueness at the lowest scattering threshold by simply tuning the Raman laser intensity provides us a new dimension of controlling the cold atom experiments.

Realizations of 1D theoretical models, such as Tonks-Girardeau gases and Luttinger liquids, are made possible with confinement-induced resonances. The extra Raman coupling reduces the harsh requirement in the trap frequencies, however, with the potential issue in heating.

5. SUMMARY AND OUTLOOK

Spin-orbit coupling in cold atoms has generated much excitement. The new properties of spin-orbit coupled quantum degenerate gases have been widely explored not only from the many-body perspectives but also the few-body viewpoints. In this thesis work, we have studied the spin-orbit coupled quantum gases mainly from the theoretical few-body perspectives in the following three aspects: scattering, resonance, and bound state formation. In chapter three, we have seen that the existence of spin-orbit coupling changes the scattering behaviors in a fundamental way, which gives new scattering threshold laws and leads to the spontaneous handedness in spin-orbit coupled systems. In Chapter four, we have explored scattering resonances in the multichannel scattering in the presence of equal Rashba and Dresselhaus spin-orbit coupling. We find that whenever, the scattering energy of the incoming state, which is located between different scattering threshold in different channels, hits a quasi-bound state energy state supported by the closed channels, the resonance between the scattering state and the quasi-bound state leads to a total reflection. At threshold energies, the abnormal scattering behaviors show up due to the abnormal dispersion relations of a square root dependence in energy. The above conclusions have been reached in Chapter 4. With regards to the bound state formation, if the presence of spin-orbit coupling enhances the energy density of state, the atoms will form a bound state easier compared to the usual cases of a quadratic dispersion with spin degeneracies. For instance, the 3D Weyl spin-orbit coupling has a huge degeneracy due to the spherical symmetry of the constant energy surfaces, two Weyl spin-orbit coupled atoms could form a bound state even in the regime with a negative scattering length in three spatial dimension. If the energy dependence of the density of states does not vary from the usual cases, then the condition of bound state formation remain the same. This is verified in the double-minimum regime with an equal mixing of Rashba-Dresselhaus spin-orbit coupling in Chapter 4. The in-detail conclusions could be found at the end of each chapter.

In the following sections, we discuss several possible extensions suggested by the studies so far. One interesting study would be to include the p-wave interaction. Since spin-orbit coupling mixes different partial waves, it would be interesting to explore the interplay of spin-orbit coupling and the simultaneous existence of the s- and p-wave interactions. We discuss the partial wave interference due to spin-orbit coupling in Sec. 5.1. In Sec. 5.2, we adapt the hyperspherical coordinate framework to three-body systems in the presence of spin-orbit coupling with the motivation to investigate how the new length scale of spin-orbit coupling affects the universality in ultracold atomic systems. In the last section, we will briefly discuss other interesting potential directions of studying synthetic gauge fields in ultracold atomic systems to conclude the dissertation.

5.1 SOC-induced partial wave interferences in the ultracold scattering

In this section, we set up the scattering formalism to cope with any type of short-range potential with the method of the Harmin-Fano local frame transformation [79, 80, 81, 82] under the assumption of the length scale separation. We acknowledge the contribution from Panos Giannakeas in the derivations here. The method we develop here would be very useful to explore the importance of the contribution of the higher-partial waves when SOC exists. Also, the method goes beyond the pseudo-potential approximation, so a realistic two-body interaction, such as a Lennard-Jones potential, may be included easily.

5.1.1 Application of the local frame transformation

The original idea of the local frame transformation is based on the fact that a system is separable in different coordinate systems in two different regions of the configuration space. Therefore, the full solution can be derived by propagating the wave functions in the inner region with a symmetry there to the outer region with another different symmetry through a local non-unitary frame transformation. The validity of the treatment is based on the assumption of *length scale separation*.

Since the spin-orbit coupling couples different partial waves, our treatment elegantly deals with the crucial feature of spin-orbit coupling by matching the short-range solution under the influence of the two-body interaction to the asymptotic solutions affected only by spin-orbit coupling. The validity of the treatment is based on the assumption of a *length scale separation*, see Fig. 5.1. If the length scale determined by spin-orbit coupling, λ^{-1} (we adopt the same notation from the preceding chapter), is much longer than the potential range controlled by the two-body interaction, then we can solve the two-body scattering problem in the presence of spin-orbit coupling by knowing only the non-interacting two-body solutions with spin-orbit coupling and their connections to the interacting two-body solutions in the absence of spin-orbit coupling.

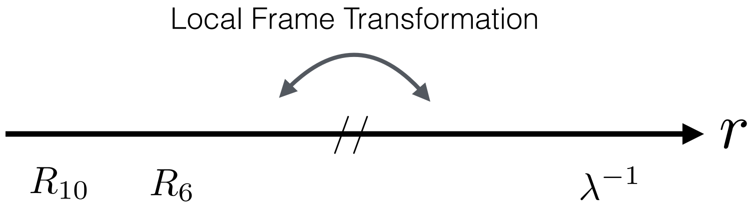

Figure 5.1.: The length scale separation in spin-orbit coupled systems. The parameter, λ, is the SOC strength with the unit of momentum/$\hbar$. R_n is the length scale for $-C_n/r^n$ type of potentials. R_6 is the length scale for the van der Waals potential.

Chapter 3 shows that the scattering solution with the Weyl spin-orbit coupling is given by

$$\underline{\psi}^{\mathrm{SOC}}(r) = \frac{\underline{f}(r)}{r} - \frac{\underline{g}(r)}{r}\underline{K}^{\mathrm{SO}}, \tag{5.1}$$

where

$$\frac{\underline{\underline{f}}(r)}{r} = \begin{pmatrix} \frac{1}{\sqrt{3}}\frac{k_1}{\sqrt{k_1}}j_0(k_1r) & \frac{1}{\sqrt{3}}\frac{k_2}{\sqrt{k_2-\lambda}}j_0(k_2r) & \frac{1}{\sqrt{3}}\frac{k_3}{\sqrt{k_3+\lambda}}j_0(k_3r) \\ 0 & \frac{i}{\sqrt{2}}\frac{k_2}{\sqrt{k_2-\lambda}}j_1(k_2r) & -\frac{i}{\sqrt{2}}\frac{k_3}{\sqrt{k_3+\lambda}}j_1(k_3r) \\ \frac{\sqrt{2}}{\sqrt{3}}\frac{k_1}{\sqrt{k_1}}j_2(k_1r) & -\frac{1}{\sqrt{6}}\frac{k_2}{\sqrt{k_2-\lambda}}j_2(k_2r) & -\frac{1}{\sqrt{6}}\frac{k_3}{\sqrt{k_3+\lambda}}j_2(k_3r) \end{pmatrix}, \tag{5.2}$$

where

$$k_1 = k \tag{5.3}$$

$$k_2 = \sqrt{k^2+\lambda^2}+\lambda \tag{5.4}$$

$$k_3 = \sqrt{k^2+\lambda^2}-\lambda, \tag{5.5}$$

Notice that the overall factor $\sqrt{\frac{2\mu}{\pi\hbar^2}}$ is removed in Eq. (5.2) compared to the result in Ch. 3. The irregular solution, $\underline{g}(r)$, can be obtained by replacing $j_\ell(k_ir)$ with $y_\ell(k_ir)$ for $i \in \{1,2,3\}$. The scattering energy, $E = \hbar^2k^2/m$, is determined by the wave number $k_1 = k$. These three different wave numbers are related with each other. The following relations will be useful later.

$$k_2 - \lambda = k_3 + \lambda \tag{5.6}$$

$$k_1^2 = k_2k_3. \tag{5.7}$$

In the short-range region, $r \ll 1/\lambda$, the effect of SOC is negligible. Therefore, the free 3D scattering solution describes the solution in this region very well.

$$\psi^{\text{3D}}(r) = F(r) - G(r)K^{\text{3D}}, \tag{5.8}$$

where the regular solution is

$$F(r) = \begin{pmatrix} \sqrt{k_1}j_0(k_1r) & 0 & 0 \\ 0 & \sqrt{k_1}j_1(k_1r) & 0 \\ 0 & 0 & \sqrt{k_1}j_2(k_1r) \end{pmatrix}, \tag{5.9}$$

and the irregular solution is

$$G(r) = \begin{pmatrix} \sqrt{k_1}y_0(k_1r) & 0 & 0 \\ 0 & \sqrt{k_1}y_1(k_1r) & 0 \\ 0 & 0 & \sqrt{k_1}y_2(k_1r) \end{pmatrix}. \tag{5.10}$$

Now we want to find the connection between the two sets of solution in the short-range and long-range regions. The multiplication theorem [83] is used to relate the solutions.

$$j_\ell(k_j r) = (\frac{k_j}{k_1})^\ell \sum_{n=0}^{\infty} \frac{1}{n!}\left[\frac{1-(k_j/k_1)^2}{2}\right]^n (k_1 r)^n j_{\ell+n}(k_1 r) \tag{5.11}$$

$$y_\ell(k_j r) = (\frac{k_1}{k_j})^{\ell+1} \sum_{n=0}^{\infty} \frac{1}{n!}\left[\frac{1-(k_j/k_1)^2}{2}\right]^n (k_1 r)^n y_{\ell-n}(k_1 r) \tag{5.12}$$

Assuming the scattering energy is low, the first term in the infinite sums of Eq. (5.11) and Eq. (5.12) suffices. Therefore,

$$j_\ell(k_j r) \approx \left(\frac{k_j}{k_1}\right)^\ell j_\ell(k_1 r), \tag{5.13}$$

$$y_\ell(k_j r) \approx \left(\frac{k_1}{k_j}\right)^{\ell+1} y_\ell(k_1 r). \tag{5.14}$$

Therefore, the regular solution with SOC in Eq. (5.2) can be rewritten in terms of the 3D free regular solution in Eq. (5.9) as follows:

$$\begin{aligned}\frac{f(r)}{r} &= \begin{pmatrix} \frac{1}{\sqrt{3}}\frac{k_1}{\sqrt{k_1}} j_0(k_1 r) & \frac{1}{\sqrt{3}}\frac{k_2}{\sqrt{k_2-\lambda}} j_0(k_2 r) & \frac{1}{\sqrt{3}}\frac{k_3}{\sqrt{k_3+\lambda}} j_0(k_3 r) \\ 0 & \frac{i}{\sqrt{2}}\frac{k_2}{\sqrt{k_2-\lambda}} j_1(k_2 r) & -\frac{i}{\sqrt{2}}\frac{k_3}{\sqrt{k_3+\lambda}} j_1(k_3 r) \\ \frac{\sqrt{2}}{\sqrt{3}}\frac{k_1}{\sqrt{k_1}} j_2(k_1 r) & -\frac{1}{\sqrt{6}}\frac{k_2}{\sqrt{k_2-\lambda}} j_2(k_2 r) & -\frac{1}{\sqrt{6}}\frac{k_3}{\sqrt{k_3+\lambda}} j_2(k_3 r) \end{pmatrix} \\ &= \begin{pmatrix} \sqrt{k_1} j_0(k_1 r) & 0 & 0 \\ 0 & \sqrt{k_1} j_1(k_1 r) & 0 \\ 0 & 0 & \sqrt{k_1} j_2(k_1 r) \end{pmatrix} \underbrace{\begin{pmatrix} \frac{1}{\sqrt{3}} & \frac{1}{\sqrt{3}}\sqrt{\frac{k_1}{k_2-\lambda}}\frac{k_2}{k_1} & \frac{1}{\sqrt{3}}\sqrt{\frac{k_1}{k_3+\lambda}}\frac{k_3}{k_1} \\ 0 & \frac{i}{\sqrt{2}}\sqrt{\frac{k_1}{k_2-\lambda}}\frac{k_2^2}{k_1^2} & -\frac{i}{\sqrt{2}}\sqrt{\frac{k_1}{k_3+\lambda}}\frac{k_3^2}{k_1^2} \\ \frac{\sqrt{2}}{\sqrt{3}} & -\frac{1}{\sqrt{6}}\sqrt{\frac{k_1}{k_2-\lambda}}\frac{k_2^3}{k_1^3} & -\frac{1}{\sqrt{6}}\sqrt{\frac{k_1}{k_3+\lambda}}\frac{k_3^3}{k_1^3} \end{pmatrix}}_{U}\end{aligned} \tag{5.15}$$

$$\equiv F(r)U, \tag{5.16}$$

where U is the frame transformation matrix. Similarly, we can relate the irregular solutions in these two regions with the transformation matrix of V.

$$\frac{g(r)}{r} = \begin{pmatrix} \frac{1}{\sqrt{3}}\frac{k_1}{\sqrt{k_1}}y_0(k_1r) & \frac{1}{\sqrt{3}}\frac{k_2}{\sqrt{k_2-\lambda}}y_0(k_2r) & \frac{1}{\sqrt{3}}\frac{k_3}{\sqrt{k_3+\lambda}}y_0(k_3r) \\ 0 & \frac{i}{\sqrt{2}}\frac{k_2}{\sqrt{k_2-\lambda}}y_1(k_2r) & -\frac{i}{\sqrt{2}}\frac{k_3}{\sqrt{k_3+\lambda}}y_1(k_3r) \\ \frac{\sqrt{2}}{\sqrt{3}}\frac{k_1}{\sqrt{k_1}}y_2(k_1r) & -\frac{1}{\sqrt{6}}\frac{k_2}{\sqrt{k_2-\lambda}}y_2(k_2r) & -\frac{1}{\sqrt{6}}\frac{k_3}{\sqrt{k_3+\lambda}}y_2(k_3r) \end{pmatrix}$$

$$= \begin{pmatrix} \sqrt{k_1}y_0(k_1r) & 0 & 0 \\ 0 & \sqrt{k_1}y_1(k_1r) & 0 \\ 0 & 0 & \sqrt{k_1}y_2(k_1r) \end{pmatrix} \underbrace{\begin{pmatrix} \frac{1}{\sqrt{3}} & \frac{1}{\sqrt{3}}\sqrt{\frac{k_1}{k_2-\lambda}} & \frac{1}{\sqrt{3}}\sqrt{\frac{k_1}{k_3+\lambda}} \\ 0 & \frac{i}{\sqrt{2}}\sqrt{\frac{k_1}{k_2-\lambda}}\frac{k_1}{k_2} & -\frac{i}{\sqrt{2}}\sqrt{\frac{k_1}{k_3+\lambda}}\frac{k_1}{k_3} \\ \frac{\sqrt{2}}{\sqrt{3}} & -\frac{1}{\sqrt{6}}\sqrt{\frac{k_1}{k_2-\lambda}}\frac{k_1^2}{k_2^2} & -\frac{1}{\sqrt{6}}\sqrt{\frac{k_1}{k_3+\lambda}}\frac{k_1^2}{k_3^2} \end{pmatrix}}_{V} \tag{5.17}$$

$$\equiv G(r)V, \tag{5.18}$$

With the matrices, U and V, we can derive the K matrix in the presence of the 3D isotropic SOC in terms of the K matrix in the absence of SOC. Since

$$\psi^{\mathrm{3D}}U = (F - GK^{\mathrm{3D}})U = \frac{f(r)}{r} - \frac{g(r)}{r}V^{-1}K^{\mathrm{3D}}U, \tag{5.19}$$

we get

$$\psi^{\mathrm{SOC}} = \frac{f(r)}{r} - \frac{g(r)}{r}K^{\mathrm{SOC}} \equiv \psi^{\mathrm{3D}}U = \frac{f(r)}{r} - \frac{g(r)}{r}(V^{-1}K^{\mathrm{3D}}U). \tag{5.20}$$

Therefore,

$$K^{\mathrm{SOC}} = V^{-1}K^{\mathrm{3D}}U. \tag{5.21}$$

The above equation tells us that we can find the scattering solution in the presence of SOC by only knowing the *non-interacting* stationary solution with SOC given that the scattering solution with the same short-range potential is known! The matrix K^{3D} is defined in the usual sense,

$$K^{\mathrm{3D}} = \begin{pmatrix} \tan\delta_0 & 0 & 0 \\ 0 & \tan\delta_1 & 0 \\ 0 & 0 & \tan\delta_2 \end{pmatrix}, \tag{5.22}$$

where δ_ℓ are the ℓ-wave phase shifts. They are determined by the two-body interaction. Plenty of research on finding the scattering phase shifts [84][cite more] are available and could be immediately applied in our spin-orbit coupled systems.

As a sanity test of our result, we now apply the local frame transformation method to the scattering problem in Chapter 3, where we consider only the s-wave interaction. When we include only the lowest partial wave interaction, the 3D K matrix is reduced to

$$K^{\mathrm{3D}} = \begin{pmatrix} \tan\delta_0 & 0 & 0 \\ 0 & 0 & 0 \\ 0 & 0 & 0 \end{pmatrix}. \tag{5.23}$$

In the low-energy scattering, $\tan\delta_0 = -ka_s$, where a_s is s-wave scattering length. Plugging Eq. (5.23) into Eq. (5.21), we get

$$K^{\mathrm{SOC}} = V^{-1}K^{\mathrm{3D}}U = \frac{-2a_s}{3(k_2+k_3)} \begin{pmatrix} \frac{k_1(k_2+k_3)}{2} & k_2\sqrt{\frac{k_1(k_2+k_3)}{2}} & k_3\sqrt{\frac{k_1(k_2+k_3)}{2}} \\ k_2\sqrt{\frac{k_1(k_2+k_3)}{2}} & k_2^2 & k_2k_3 \\ k_3\sqrt{\frac{k_1(k_2+k_3)}{2}} & k_3k_2 & k_3^2 \end{pmatrix}, \tag{5.24}$$

which is equivalent to the K matrix we have derived in Eq. (3.31). It can be shown easily with the identities listed in Eq. (5.6) and Eq. (5.7).

When evaluating the K matrix with SOC, we use the following identity to avoid performing matrix inversions, which are more time-consuming than finding conjugate transpose of matrices.

$$K^{\mathrm{SOC}} = V^{-1}K^{\mathrm{3D}}U = U^{\dagger}K^{\mathrm{3D}}U. \tag{5.25}$$

Eq. (5.25) is the key result of our derivations here. It could be used to explore the interplay of different type interaction, such as Lennard-Jones interactions or dipolar interactions and the spin-orbit coupling. Even more interestingly, because of the mixing of partital waves, the synthetic spin-orbit coupling could potentially provide a new way to engineer p-wave interaction [85], which contributes to realizations of fractional quantum hall states [86][87] and p-wave superfluidity [88][89].

5.2 Three-body physics with synthetic spin-orbit coupling

One central theme in various branches of physics is the universality, and few-body systems are wonderful places to observe this phenomenon. When a few particles are interacting through short-range interactions with divergent scattering length, their properties exhibit universality. From the Efimov trimers [90][91] in nuclear physics to the ultracold atomic clusters in quantum gases, their binding energies in the unitary limit are all found to follow the same discrete scaling laws despite the very different details in the separate systems. These remarkable theoretical predictions have been experimentally verified [92] thanks to the advances of the experimental techniques in atom trapping/cooling [93] and the capability of tuning scattering length via external fields, which is known as Feshbach resonances [7]. Investigation of few-body physics not only brings us astonishing physics, like universality [94], but also provides practical purposes in controlling the stability of quantum gases [95]. Furthermore, it helps us to bridge the gap between few-body physics and many-body physics by identifying the key aspects of macroscopic properties of a many-body system through few-body solutions.

In this section, we construct the foundation to prepare us to study the three-body physics in the presence of spin-orbit coupling with the aim to understand how the new length scale introduced by SOC affects the universality in few-body worlds. We first re-express the three-body Hamiltonian in the presence of isotropic spin-orbit coupling (SOC) in terms of the hyperspherical coordinate. The traditional three-body Hamiltonian without spin-orbit coupling is well studied, so the crucial part is how one can write the linear momentum operator in the hyperspherical coordinate, which couples to spin causing the SOC. Here, we follow a similar procedure as in Kuppermann's work [96] to derive *the matrix gradient operator* and then obtain the kinetic energy operator and the SOC operator from there. With those, the full Hamiltonian describing the spin-orbit coupled system in hyperspherical coordinate is achieved, which is a starting point to explore the multi-particle physics in the presence of synthetic spin-orbit coupling.

5.2.1 Mass-scaled Jacobi coordinates

The full Hamiltonian for three spins with isotropic spin-orbit coupling:

$$H_{3\mathrm{b}} = \frac{\vec{p}_1^2}{2m_1} + \frac{\vec{p}_2^2}{2m_2} + \frac{\vec{p}_3^2}{2m_3} + \frac{\hbar\lambda}{m_1}\vec{p}_1 \cdot \vec{\sigma}_1 + \frac{\hbar\lambda}{m_2}\vec{p}_2 \cdot \vec{\sigma}_2 + \frac{\hbar\lambda}{m_3}\vec{p}_3 \cdot \vec{\sigma}_3 + V(r_{12}, r_{23}, r_{31}), \quad (5.26)$$

where $\vec{p}_i = -i\hbar\nabla_{\vec{r}_i}$ with commutation relations, $[x_i, p_{i,x}] = [y_i, p_{i,y}] = [z_i, p_{i,z}] = i\hbar$ $(i = 1, 2, 3)$. In the following, we are going to rewrite the Hamiltonian in terms of mass-scaled Jacobi coordinates and then separate the center of mass coordinate from the relative coordinates. The Jacobi coordinates, $\{\vec{\rho}_{0i} | i = 1, ..., N\}$, for a system of size N are defined as the set of the $N-1$ relative coordinates plus the center of mass coordinate. The ith relative coordinate is the vector pointing from the center of mass of the first i particles to the $(i+1)$th particle for $i = 1, 2, ..., N-1$. The Nth Jacobi coordinate, which connects the center of mass of the first $N-1$ particles to the last particle, is exactly the c.o.m. coordinate of the full system. It is a useful coordinate system to describe any physical system with global translational invariance $([\sum_i \vec{p}_i, \hat{H}] = 0)$ since the last coordinate (or the center of mass coordinate) can be separated from the other $(N-1)$ relative coordinates. The *mass-scaled* Jacobi coordinates for any number of particle sets (N) are defined as follows:

$$\vec{\rho}_j = \sqrt{\frac{\mu_j}{\mu}}\vec{\rho}_{0j}, \quad (5.27)$$

where $\mu_j = (\sum_{i=1}^{j} m_i \times m_{j+1}) / \sum_{i=1}^{j+1} m_i$ and $\mu = (\Pi_{i=1}^{N} m_i / \sum_{i=1}^{N} m_i)^{1/(N-1)}$. The reason for mass scaling the Jacobi coordinates will become clear later when we write down the kinetic energy operator. For a triatomic system, the first Jacobi coordinate is the vector pointing from particle 1 to particle 2, and the second Jacobi coordinate is the vector pointing from the c.o.m. of the first two particles to the third particle.

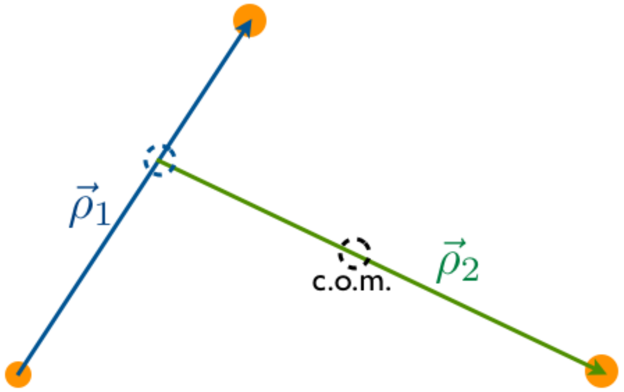

[htp!]

Figure 5.2.: The Jacobi coordinates (without mass scaling) for the three-body system. The first Jacobi vector connect the first two particles, and the second Jacobi vector connects the center of mass of the first two particles with the third particle. We could imagine an imaginary particle with mass equal to $(m_1 + m_2)$ standing in the spot of the center of mass of the first two particles. So the second Jacobi vector simply connects the imaginary particle we cook up and the third particle. The center of mass of the imaginary particle and the third particle is exactly the center of mass of the whole system. So the vector pointing from the origin to the system's c.o.m. is the third Jacobi vector or the c.o.m. vector of the three-body system. This logic applies to any system of size N, which is a nonzero positive integer.

Please refer to Fig. 5.2 for a pictorial explanation. The mass-scaled Jacobi coordinates for a three-body system are:

$$\vec{\rho}_1 = (\vec{r}_1 - \vec{r}_2)/d \tag{5.28}$$

$$\vec{\rho}_2 = (\frac{m_1\vec{r}_1 + m_2\vec{r}_2}{m_1 + m_2} - \vec{r}_3)d \tag{5.29}$$

$$\vec{\rho}_3 = \frac{\sum_{i=1,2,3} m_i\vec{r}_i}{M}, \tag{5.30}$$

where $d^2 = \mu/\mu_1 = \mu_2/\mu = (m_3/\mu)(1 - m_3/M)$, $\mu^2 = m_1 m_2 m_3/M$ with $M = m_1 + m_2 + m_3$. The corresponding canonical momenta for the above three Jacobi coordinates are

$$\begin{aligned} \vec{\pi}_1 &= \frac{\mu}{d}(\frac{\vec{p}_1}{m_1} - \frac{\vec{p}_2}{m_2}) && (5.31)\\ \vec{\pi}_2 &= \mu d(\frac{\vec{p}_1 + \vec{p}_2}{m_1 + m_2} - \frac{\vec{p}_3}{m_3}) && (5.32)\\ \vec{\pi}_3 &= \vec{p}_1 + \vec{p}_2 + \vec{p}_3. && (5.33) \end{aligned}$$

They satisfy the commutation relations, $[\hat{\rho}_{1j}, \hat{\pi}_{1k}] = [\hat{\rho}_{2j}, \hat{\pi}_{2k}] = [\hat{\rho}_{3j}, \hat{\pi}_{3k}] = i\hbar\delta_{j,k}$ for $\{j,k\} = \{1,2,3\}$. The inverse transformation is

$$\begin{aligned} \vec{p}_1 &= \frac{d\mu_{1,2}}{\mu}\vec{\pi}_1 + \frac{m_1 m_3}{d\mu M}\vec{\pi}_2 + \frac{m_1}{M}\vec{\pi}_3 && (5.34)\\ \vec{p}_2 &= -\frac{d\mu_{1,2}}{\mu}\vec{\pi}_1 + \frac{m_2 m_3}{d\mu M}\vec{\pi}_2 + \frac{m_2}{M}\vec{\pi}_3 && (5.35)\\ \vec{p}_3 &= -\frac{\mu_{12,3}}{d\mu}\vec{\pi}_2 + \frac{m_3}{M}\vec{\pi}_3, && (5.36) \end{aligned}$$

where $\mu_{1,2} = \mu_1 = m_1 m_2/(m_1 + m_2)$ and $\mu_{12,3} = \mu_2 = (m_1 + m_2)m_3/(m_1 + m_2 + m_3)$. So the new Hamiltonian in Jacobi coordinates is

$$\begin{aligned} H_{\mathrm{3b}} &= \frac{\vec{\pi}_1^2}{2\mu} + \frac{\vec{\pi}_2^2}{2\mu} + \frac{\hbar\lambda d\mu_{1,2}}{\mu}\left[\vec{\pi}_1 \cdot (\frac{\vec{\sigma}_1}{m_1} - \frac{\vec{\sigma}_2}{m_2})\right] + \frac{\hbar\lambda}{d\mu}\vec{\pi}_2 \cdot \left[\frac{m_3}{M}(\vec{\sigma}_1 + \vec{\sigma}_2) - \frac{\mu_{12,3}}{m_3}\vec{\sigma}_3\right]\\ &\quad + \left[\frac{\vec{\pi}_3^2}{2M} + \frac{\hbar\lambda}{M}\vec{\pi}_3 \cdot (\vec{\sigma}_1 + \vec{\sigma}_2 + \vec{\sigma}_3)\right] + V(r_{12}, r_{23}, r_{31}). \qquad (5.37) \end{aligned}$$

Here we see the advantage of applying the "mass-scaled" Jacobi coordinates. The canonical momenta except the c.o.m. one will share the same effective mass, μ. Considering the case of zero c.o.m. momentum ($\vec{\pi}_3 = 0$), the relative Hamiltonian becomes

$$H_{\mathrm{3b}}^{\mathrm{rel}} = \frac{\vec{\pi}_1^2}{2\mu} + \frac{\vec{\pi}_2^2}{2\mu} + \frac{\hbar\lambda d\mu_{1,2}}{\mu}\vec{\pi}_1 \cdot (\frac{\vec{\sigma}_1}{m_1} - \frac{\vec{\sigma}_2}{m_2}) + \frac{\hbar\lambda}{d\mu}\vec{\pi}_2 \cdot \left[\frac{m_3}{M}(\vec{\sigma}_1 + \vec{\sigma}_2) - \frac{\mu_{12,3}}{m_3}\vec{\sigma}_3\right] + V(r_{12}, r_{23}, r_{31}), \qquad (5.38)$$

where $\vec{\pi}_1 = -i\hbar\nabla_{\vec{\rho}_1}$ and $\vec{\pi}_2 = -i\hbar\nabla_{\vec{\rho}_2}$. The interaction Hamiltonian can also be expressed in terms of $\vec{\rho}_1$ and $\vec{\rho}_2$ only with

$$V(r_{12}, r_{23}, r_{31}) = V(|d\vec{\rho}_1|, |d\vec{\rho}_1/2 - \vec{\rho}_2/d|, |d\vec{\rho}_1/2 + \vec{\rho}_2/d|). \qquad (5.39)$$

5.2.2 The hyperspherical coordinates

In the section, we are going to write the two 3-dimensional Cartesian Jacobi vectors in a 6-dimensional hyperspherical coordinate. There are several ways of defining hyperspherical coordinates. One way to categorize different hyperspherical coordinates is whether the coordinate is a space-fixed coordinate or a body-fixed one. Here, we define them in the body-fixed frame of reference. In this frame, the six Jacobi coordinates are expressed in terms of three internal coordinates, $\{\rho, \theta, \delta\}$, which determine the overall size and shape, and three Euler angles, $\{\alpha, \beta, \gamma\}$, which determine the orientation of this triangular plane formed by three particles.

$$\boldsymbol{\rho}^{\mathrm{sf}} = \left(\vec{\rho}_{N-1}, \quad ... \quad \vec{\rho}_2, \quad \vec{\rho}_1\right) = \begin{pmatrix} x_{N-1} & ... & x_2 & x_1 \\ y_{N-1} & ... & y_2 & y_1 \\ z_{N-1} & ... & z_2 & z_1 \end{pmatrix} = \mathbf{R}^T(\alpha, \beta, \gamma)\rho\mathbf{N}(\theta)\mathbf{Q}(\delta), \tag{5.40}$$

where the three Euler angles rotate the space-fixed coordinate frame to the body-fixed principal-axes-of-inertia frame (passive rotation). Here, we apply the z-y-z convention.

$$\mathbf{R}(\alpha, \beta, \gamma) = \mathbf{M}_1(\gamma)\mathbf{M}_2(\beta)\mathbf{M}_1(\alpha) \tag{5.41}$$

where $\mathbf{M}_1$ and $\mathbf{M}_2$ are

$$\mathbf{M}_1(\omega) = \begin{pmatrix} \cos\omega & \sin\omega & 0 \\ -\sin\omega & \cos\omega & 0 \\ 0 & 0 & 1 \end{pmatrix} \tag{5.42}$$

$$\mathbf{M}_2(\omega) = \begin{pmatrix} \cos\omega & 0 & -\sin\omega \\ 0 & 1 & 0 \\ \sin\omega & 0 & \cos\omega \end{pmatrix} \tag{5.43}$$

The matrix $\mathbf{N}$ and $\mathbf{Q}$ separately are

$$\mathbf{N}(\theta) = \begin{pmatrix} \cos\theta & 0 & 0 \\ 0 & \sin\theta & 0 \\ 0 & 0 & 0 \end{pmatrix} \text{ and } \mathbf{Q}(\delta) = \begin{pmatrix} \cos\delta & \sin\delta \\ -\sin\delta & \cos\delta \\ 0 & 0 \end{pmatrix}. \tag{5.44}$$

The matrix $\mathbf{Q}$ is a row-orthogonal but not a row-orthonormal matrix since

$$\mathbf{Q}\mathbf{Q}^T = \begin{pmatrix} 1 & 0 & 0 \\ 0 & 1 & 0 \\ 0 & 0 & 0 \end{pmatrix}, \tag{5.45}$$

which is not an identity matrix. Before we perform the Euler rotations, the two relative Jacobi coordinates describe the three particles lying in the body-frame $x-y$ plane with their z components being zero. The angles θ and δ are the internal angles that characterize the principal-axes moment of inertia of the system and the rotational freedom around the z-axis away from the principal-axes-of-inertia coordinate.

$$\rho\mathbf{N}(\theta)\mathbf{Q}(\delta) = \begin{pmatrix} \rho\cos\theta\cos\delta & \rho\cos\theta\sin\delta \\ -\rho\sin\theta\sin\delta & \rho\sin\theta\cos\delta \\ 0 & 0 \end{pmatrix} \tag{5.46}$$

The fact that only one angle, θ, characterizes the principal axes moment of inertia is because for a triatomic system, two principal axes must lie in the plane and the third one (here, the z axis) must be perpendicular to the plane. Thus, the moment of inertia for the perpendicular axis is the sum of that of the other two. In general, we need two angles to specify the moment of inertia of the principal axes. For system size $N \geq 4$, please consult Kuppermann's papers [97][98] for a rather straightforward generalization.

5.2.3 The matrix gradient operator

We define the matrix gradient operator $\boldsymbol{\nabla}$ by

$$\boldsymbol{\nabla} = \begin{pmatrix} \partial/\partial x_1 & \partial/\partial x_2 \\ \partial/\partial y_1 & \partial/\partial y_2 \\ \partial/\partial z_1 & \partial/\partial z_2 \end{pmatrix}. \tag{5.47}$$

The kinetic energy operator can be written in a concise form as

$$T = -\frac{\hbar^2}{2\mu}\mathrm{tr}(\boldsymbol{\nabla}\boldsymbol{\nabla}^T). \tag{5.48}$$

The matrix gradient operator is composed of the coefficients of the expansion of the total derivative operator in 6D Cartesian coordinates formed by two relative Jacobi coordinates,

$$\hat{d} = \sum_{j=1}^{2} \left[dx_j \frac{\partial}{\partial x_j} + dy_j \frac{\partial}{\partial y_j} + dz_j \frac{\partial}{\partial z_j} \right]. \tag{5.49}$$

Another way to express the same operator would be to express it in terms of the six coordinates in the hyperspherical coordinate.

$$\hat{d} = \left(d\alpha \frac{\partial}{\partial \alpha} + d\beta \frac{\partial}{\partial \beta} + d\gamma \frac{\partial}{\partial \gamma} \right) + \left(d\rho \frac{\partial}{\partial \rho} + d\theta \frac{\partial}{\partial \theta} \right) + d\delta \frac{\partial}{\partial \delta} \equiv \hat{d}_1 + \hat{d}_2 + \hat{d}_3. \tag{5.50}$$

By comparing these two expressions, we are able to extract the expressions for the matrix gradient operator, which summarizes what we do in the following.

The derivatives of the Euler angles are related with the orbital angular momentum operator $\hat{\vec{L}}$ in the body-fixed frame by

$$\begin{pmatrix} \frac{\partial}{\partial \alpha} \\ \frac{\partial}{\partial \beta} \\ \frac{\partial}{\partial \gamma} \end{pmatrix} = \frac{i}{\hbar} \begin{pmatrix} -\sin\beta\cos\gamma & \sin\beta\sin\gamma & \cos\beta \\ \sin\gamma & \cos\gamma & 0 \\ 0 & 0 & 1 \end{pmatrix} \begin{pmatrix} \hat{L}_x \\ \hat{L}_y \\ \hat{L}_z \end{pmatrix}. \tag{5.51}$$

So the operator $\hat{d}_1$ is re-expressed as

$$\hat{d}_1 = \frac{i}{\hbar} \big[(-\sin\beta\cos\gamma d\alpha + \sin\gamma d\beta)\hat{L}_x + (\sin\beta\sin\gamma d\alpha + \cos\gamma d\beta)\hat{L}_y + (\cos\beta d\alpha + d\gamma)\hat{L}_z \big]. \tag{5.52}$$

It can be shown easily that the above expression is equivalent to

$$\hat{d}_1 = -\frac{i}{2\hbar} \sum_{i,j=1}^{3} \left[\epsilon_{ij1} (\mathbf{R} d\mathbf{R}^T)_{ij} \hat{L}_x + \epsilon_{ij2} (\mathbf{R} d\mathbf{R}^T)_{ij} \hat{L}_y + \epsilon_{ij3} (\mathbf{R} d\mathbf{R}^T)_{ij} \hat{L}_z \right], \tag{5.53}$$

where ϵ_{ijk} is the Levi-Civita density tensor.

Next we want to express the $\hat{d}_2$ and $\hat{d}_3$ operator in a more useful form. Starting with Eq. (5.40), and take the differential of it, we get

$$d\boldsymbol{\rho}^{\mathrm{sf}} = (d\mathbf{R}^T)\rho\mathbf{N}\mathbf{Q} + \mathbf{R}^T d(\rho\mathbf{N})\mathbf{Q} + \mathbf{R}^T \rho\mathbf{N} d\mathbf{Q}. \tag{5.54}$$

Multiplying the matrix $\mathbf{R}$ from the left and the matrix $\mathbf{Q}^T$ from the right, we get

$$\mathbf{R} d\boldsymbol{\rho}^{\mathrm{sf}} \mathbf{Q}^T = \mathbf{R}(d\mathbf{R}^T)\rho\mathbf{N} + d(\rho\mathbf{N}) + \rho\mathbf{N}(d\mathbf{Q})\mathbf{Q}^T, \tag{5.55}$$

where we have used the orthogonality of the matrix $\mathbf{Q}$ so that $\mathbf{N}(\mathbf{Q}\mathbf{Q}^T) = \mathbf{N}$. Also due to that, we matrix $\mathbf{R}(d\mathbf{R}^T)$ and $(d\mathbf{Q})\mathbf{Q}^T$ are anti-symmetric matrices, and all the diagonal matrix elements are zero. Knowing that the matrix $\mathbf{N}$ and its derivative d$\mathbf{N}$ are both diagonal matrices, a advantageous way to express the relevant matrices of differentials in Eq.(5.55) are to express them in terms of this useful matrix, $\mathbf{R}(d\boldsymbol{\rho}^{\mathrm{sf}})\mathbf{Q}^T$, which is going to appear in several places.

$$d(\rho\mathbf{N}) = \mathbf{N}d\rho + \rho\mathbf{N}'d\theta = \mathrm{diag}[\mathbf{R}(d\boldsymbol{\rho}^{\mathrm{sf}})\mathbf{Q}^T] \tag{5.56}$$

$$\mathbf{R}(d\mathbf{R}^T)\rho\mathbf{N} + \rho\mathbf{N}(d\mathbf{Q})\mathbf{Q}^T = \text{off-diagonal}[\mathbf{R}(d\boldsymbol{\rho}^{\mathrm{sf}})\mathbf{Q}^T], \tag{5.57}$$

where

$$\mathbf{N}' = \begin{pmatrix} -\sin\theta & 0 & 0 \\ 0 & \cos\theta & 0 \\ 0 & 0 & 0 \end{pmatrix}. \tag{5.58}$$

Left multiplying Eq. (5.56) by $\mathbf{N}$ and taking trace of it, we get the expression for $d\rho$,

$$d\rho = \sum_{i=1}^{3} \mathbf{N}_{ii}(\mathbf{R}(d\boldsymbol{\rho}^{\mathrm{sf}})\mathbf{Q}^T)_{ii} = \sum_{i,j=1}^{3} \mathbf{N}_{ij}(\mathbf{R}(d\boldsymbol{\rho}^{\mathrm{sf}})\mathbf{Q}^T)_{ij}. \tag{5.59}$$

Similarly, we can find $d\theta$ by left multiplying Eq.(5.56) by $\mathbf{N}'$ and taking traces of both sides,

$$d\theta = \frac{1}{\rho}\sum_{i,j=1}^{3} \mathbf{N}'_{ij}(\mathbf{R}(d\boldsymbol{\rho}^{\mathrm{sf}})\mathbf{Q}^T)_{ij}. \tag{5.60}$$

Therefore, the operator $\hat{d}_2$ is

$$\hat{d}_2 = \sum_{i,j=1}^{3} (\mathbf{R}(d\boldsymbol{\rho}^{\mathrm{sf}})\mathbf{Q}^T)_{ij}\left(\mathbf{N}_{ij}\frac{\partial}{\partial\rho} + \frac{1}{\rho}\mathbf{N}'_{ij}\frac{\partial}{\partial\theta}\right). \tag{5.61}$$

Now considering the Eq. (5.57), knowing that the third column of $(\mathbf{R}(d\boldsymbol{\rho}^{\mathrm{sf}})\mathbf{Q}^T)$ vanishes, we get

$$(\mathbf{R}(d\mathbf{R}^T))_{ij}\rho\mathbf{N}_{jj} + \rho\mathbf{N}_{ii}[(d\mathbf{Q})\mathbf{Q}^T]_{ij} = [\mathbf{R}(d\boldsymbol{\rho}^{\mathrm{sf}})\mathbf{Q}^T]_{ij} \text{ for } i \neq j \tag{5.62}$$

Interchanging the indices i and j, we get

$$(\mathbf{R}(d\mathbf{R}^T))_{ij}\rho\mathbf{N}_{ii} + \rho\mathbf{N}_{jj}[(d\mathbf{Q})\mathbf{Q}^T]_{ij} = -[\mathbf{R}(d\boldsymbol{\rho}^{\mathrm{sf}})\mathbf{Q}^T]_{ji} \text{ for } i \neq j, \tag{5.63}$$

where the skew-symmetry of $\mathbf{R}(d\mathbf{R}^T)$ and $(d\mathbf{Q})\mathbf{Q}^T$ is applied. From Eq. (5.62) and (5.63), we can show that for $i \neq j$, the matrices $\mathbf{R}(d\mathbf{R}^T)$ and $(d\mathbf{Q})\mathbf{Q}^T$ can be expressed, again, in terms of the useful matrix $\mathbf{R}(d\boldsymbol{\rho}^{\mathrm{sf}})\mathbf{Q}^T$ as

$$\mathbf{R}(d\mathbf{R}^T)_{ij} = \frac{\rho\mathbf{N}_{jj}\left[\mathbf{R}(d\boldsymbol{\rho}^{\mathrm{sf}})\mathbf{Q}^T\right]_{ij} + \rho\mathbf{N}_{ii}\left[\mathbf{R}(d\boldsymbol{\rho}^{\mathrm{sf}})\mathbf{Q}^T\right]_{ji}}{(\rho\mathbf{N}_{jj})^2 - (\rho\mathbf{N}_{ii})^2} \tag{5.64}$$

$$d\mathbf{Q}(\mathbf{Q}^T)_{ij} = -\frac{\rho\mathbf{N}_{ii}\left[\mathbf{R}(d\boldsymbol{\rho}^{\mathrm{sf}})\mathbf{Q}^T\right]_{ij} + \rho\mathbf{N}_{jj}\left[\mathbf{R}(d\boldsymbol{\rho}^{\mathrm{sf}})\mathbf{Q}^T\right]_{ji}}{(\rho\mathbf{N}_{jj})^2 - (\rho\mathbf{N}_{ii})^2}. \tag{5.65}$$

Don't forget that, for $i = j$, their matrix elements are all zero. The first equation is going to help us simplify the operator $\hat{d}_1$, which is written in terms of $\mathbf{R}(d\mathbf{R}^T)$ in Eq. (5.53). The operator $\hat{d}_3$ can be expressed as follows,

$$\hat{d}_3 = -\frac{i}{2\hbar}\sum_{i,j=1}^{3} \epsilon_{i3j}[d\mathbf{Q}\mathbf{Q}^T]_{ij}\hat{L}_\delta, \tag{5.66}$$

where

$$\hat{L}_\delta = \frac{\hbar}{i}\frac{\partial}{\partial\delta}. \tag{5.67}$$

The operator $\hat{d}_3$ can be further simplify with the help of Eq. (5.65).

Now gathering all the pieces for the total differential, $\hat{d}$, we can express it as follows,

$$\hat{d} = \sum_{i,j=1}^{3}[\mathbf{R}(d\boldsymbol{\rho}^{\mathrm{sf}})\mathbf{Q}^T]_{ij}\Bigg[-\frac{i}{\hbar}\frac{\rho\mathbf{N}_{jj}}{(\rho\mathbf{N}_{jj})^2 - (\rho\mathbf{N}_{ii})^2} \times (\epsilon_{ij1}\hat{L}_x + \epsilon_{ij2}\hat{L}_y + \epsilon_{ij3}\hat{L}_z)$$
$$+\mathbf{N}_{ij}\frac{\partial}{\partial\rho} + \frac{1}{\rho}\mathbf{N}'_{ij}\frac{\partial}{\partial\theta} + \frac{i}{\hbar}\frac{\epsilon_{i3j}\rho\mathbf{N}_{ii}}{(\rho\mathbf{N}_{jj})^2 - (\rho\mathbf{N}_{ii})^2}\hat{L}_\delta\Bigg]. \tag{5.68}$$

We have use the equality, $\sum_{ij}\mathbf{N}_{jj}(\mathbf{R}(d\boldsymbol{\rho}^{\mathrm{sf}})\mathbf{Q}^T)_{ij} = \sum_{ij}\mathbf{N}_{ii}(\mathbf{R}(d\boldsymbol{\rho}^{\mathrm{sf}})\mathbf{Q}^T)_{ji}$. The matrix elements of $\mathbf{R}(d\boldsymbol{\rho}^{\mathrm{sf}})\mathbf{Q}^T$ are expressed as

$$[\mathbf{R}(d\boldsymbol{\rho}^{\mathrm{sf}})\mathbf{Q}^T]_{ij} = dx_2\mathbf{R}_{i1}\mathbf{Q}_{j1}+dy_2\mathbf{R}_{i2}\mathbf{Q}_{j1}+dz_2\mathbf{R}_{i3}\mathbf{Q}_{j1}+dx_1\mathbf{R}_{i1}\mathbf{Q}_{j2}+dy_1\mathbf{R}_{i2}\mathbf{Q}_{j2}+dz_1\mathbf{R}_{i3}\mathbf{Q}_{j2}. \tag{5.69}$$

Plugging Eq. (5.69) into Eq. (5.68), and comparing it with Eq. (5.49), we can extract the information about the matrix gradient operator by matching the coefficients in front of the differentials, $\{dx_1, dy_1, dz_1, dx_2, dy_2, dz_2\}$. With a little algebra, we show that

$$\boldsymbol{\nabla} = \mathbf{R}^T(\alpha, \beta, \gamma)\hat{\mathbf{A}}\mathbf{Q}(\delta) + \hat{\mathbf{F}} - \hat{\mathbf{G}}, \tag{5.70}$$

where the matrix operator $\hat{\mathbf{A}}$ is defined by

$$\hat{\mathbf{A}} = \mathbf{N}\frac{\partial}{\partial \rho} + \frac{1}{\rho}\mathbf{N}'\frac{\partial}{\partial \theta}. \tag{5.71}$$

The operator $\hat{\mathbf{F}}$ and $\hat{\mathbf{G}}$ are both 3×2 matrix operators, and are defined as follows,

$$\hat{\mathbf{F}}_{ij} = -\frac{i}{\hbar}\sum_{l,m=1}^{3} \frac{\rho \mathbf{N}_{mm}}{(\rho \mathbf{N}_{mm})^2 - (\rho \mathbf{N}_{ll})^2} \times \mathbf{R}_{li}\mathbf{Q}_{mj}(\epsilon_{ij1}\hat{L}_x + \epsilon_{ij2}\hat{L}_y + \epsilon_{ij3}\hat{L}_z) \tag{5.72}$$

$$\hat{\mathbf{G}}_{ij} = -\frac{i}{\hbar}\left[\sum_{l,m=1}^{3} \epsilon_{l3m}\frac{\rho \mathbf{N}_{ll}}{(\rho \mathbf{N}_{mm})^2 - (\rho \mathbf{N}_{ll})^2} \times \mathbf{R}_{li}\mathbf{Q}_{mj}\right]\hat{L}_\delta. \tag{5.73}$$

5.2.4 Kinetic energy operator

With the expression in Eq. (5.70), we immediately can write down any momentum-dependent operator, such as the spin-orbit interaction, in the hyperspherical coordinates. As a check, we test the formula in Eq. (5.70) with the kinetic energy operator, whose expression is well-known and has been derived with several different methods.

$$\begin{aligned} \hat{T} &= -\frac{\hbar^2}{2\mu}\mathrm{tr}(\boldsymbol{\nabla}\boldsymbol{\nabla}^T) && (5.74) \\ &= -\frac{\hbar^2}{2\mu}\left(\frac{\partial^2}{\partial \rho^2} + \frac{5}{\rho}\frac{\partial}{\partial \rho}\right) + \frac{\hat{\Lambda}^2}{2\mu\rho^2}, && (5.75) \end{aligned}$$

where

$$\begin{aligned} \hat{\Lambda}^2 &= \\ &= -\hbar^2\frac{\partial^2}{\partial \theta^2} - 4\hbar^2 \cot 4\theta \frac{\partial}{\partial \theta} - \frac{\hbar^2}{\cos^2 2\theta}\frac{\partial^2}{\partial \delta^2} - \frac{2\hbar^2 \tan 2\theta}{\cos 2\theta}\frac{\partial^2}{\partial \delta \partial \gamma} + \frac{\hat{L_x}^2}{\sin^2\theta} + \frac{\hat{L_y}^2}{\cos^2\theta} + \frac{\hat{L_z}^2}{\cos^2 2\theta} \\ &= \hat{K}^2 - 4i\hbar \cot 4\theta \hat{K} + \frac{1}{\cos^2 2\theta}\hat{L}_\delta^2 + \frac{2\tan 2\theta}{\cos 2\theta}\hat{L}_\delta \hat{L}_z + \frac{\hat{L_x}^2}{\sin^2\theta} + \frac{\hat{L_y}^2}{\cos^2\theta} + \frac{\hat{L_z}^2}{\cos^2 2\theta}, \end{aligned}$$

$$(5.76)$$

with the notation $\hat{K} = -i\hbar\partial/\partial\theta$. $\hat{\Lambda}$ is named as the grand angular momentum operator. Redefining the hyper spherical angles with

$$\theta \to \theta/2 - \pi/4, \tag{5.77}$$

$$\delta \to \delta/2 + \pi/6, \tag{5.78}$$

we rewrite the kinetic energy operator as

$$\begin{aligned} \hat{T} &= -\frac{\hbar^2}{2\mu}\left\{\frac{\partial^2}{\partial\rho^2} + \frac{5}{\rho}\frac{\partial}{\partial\rho}\right\} + \frac{\Lambda^2}{2\mu\rho^2}, & (5.79) \\ &= -\frac{\hbar^2}{2\mu}\left\{\frac{\partial^2}{\partial\rho^2} + \frac{5}{\rho}\frac{\partial}{\partial\rho}\right\} + T_\theta + T_{\phi C} + T_r, & (5.80) \end{aligned}$$

where

$$T_\theta = -\frac{2\hbar^2}{\mu\rho^2\sin 2\theta}\frac{\partial}{\partial\theta}\sin 2\theta\frac{\partial}{\partial\theta}, \tag{5.81}$$

$$T_{\phi C} = \frac{2\hbar^2}{\mu\rho^2\sin^2\theta}\big(i\frac{\partial}{\partial\delta} + \cos\theta\frac{L_z}{2}\big)^2, \tag{5.82}$$

$$T_r = \frac{1}{\mu\rho^2(1-\sin\theta)}L_x^2 + \frac{1}{\mu\rho^2(1+\sin\theta)}L_y^2 + \frac{1}{2\mu\rho^2}L_z^2. \tag{5.83}$$

We arrive at the familiar expression for the kinetic energy operator of a three-particle system.

So far, there are only two theoretical works [99][100][101] towards the understanding of few-body physics in the presence of spin-orbit coupling. In references [99] and [101], they have studied three-body system (a-a-b̃) with two different species of atoms so that only one spin-1/2 atom (b̃) inside is subjected to an isotropic spin-orbit coupling with total angular momentum $J = 3/2$ and $J = 1/2$ respectively. Another assumption they have made is that the interatomic interactions are s-wave contact potentials and are among different species of atoms only. They find that SOC can induce universal three-body bound states with a negative s-wave scattering length at a smaller mass ratio compared to the usual cases without SOC. In [100], they have applied a similar theoretical tool to calculate the bound states for a Fermi-Fermi mixture (ã-ã-b type), in which two fermions (ã) have Rashba spin-orbit coupling. They claimed to find the symmetry-selective Borromean binding, which is independent of the details of short-range interactions and thus universal. The formalism introduced in this section can deal with a more general case than the previous studies by considering three identical particles with a realistic interaction among all of them. We are excited to pursue the few-body physics in the presence of synthetic spin-orbit coupling with the hyperspherical methods in the future.

5.3 Other future directions

One goal of the cold-atom research is to be able to simulate phenomena in the condensed matter physics with highly-controllable ultracold atomic systems. One interesting direction is to study the effect of SOC by adding a lattice potential. Since the optical lattices strongly enhance the interaction energy of atoms, which are localized in the minimum of the periodic potential, it would be an intriguing direction to explore the interplay of SOC with the strongly correlated phases in the optical lattices.

Besides the big goal of quantum simulation, ultracold atomic systems are places to study unique physics on its own. The fact that atoms can carry (pseudo-) spins higher than 1/2 extends the versatility of ultracold atomic systems to a wider scope which is not covered by electron-based materials. We think studying high spin physics in ultracold quantum gases in the presence of synthetic gauge fields, in particular, spin-orbit couplings, is promising to find new physics. The large spin fluctuation, $\pm 2S$ for an spin-S atom, assures us that we don't simply approach the classical limits by increasing spins [102]. One potential topic is to study bound state structures of high spin atoms. In our previous studies, we have shown that two spin-1/2 atoms under 3D isotropic spin-orbit coupling can form two-body bound states with finite binding energy no matter how weak and negative the s-wave contact interaction is at zero center of mass momentum [54][63]. This new bound state right below the scattering threshold was very different from the usual bound state without gauge fields. In the latter case, the state had zero binding energy and was in spin singlet state. The bound state wave function for spin-1/2 atoms in the presence of gauge fields was found to have a spin nematic structure and contained a spin triplet component [54]. It motivates us to study the spin composition in bound state formations for atoms with higher spins based on the method we have developed [64]. The bound state structures are of value since they provide the information about molecular condensates formed by the tightly bound atoms. An intriguing crossover from a usual Bardeen-Cooper-Schrieffer (BCS) superfluid state to a Bose condensate formed by these predicted high-spin bound states could be found by tuning the strength of the non-abelian fields at even weak scattering lengths [103][104].

The new opportunities opened by synthetic gauge fields are fascinating. In addition to the quantum simulation and the high-spin physics we have discussed above, there are many more to be discovered. I will briefly mention four aspects in the following. First, interplay of trapping potentials with non-abelian gauge fields will create novel Hamiltonians like the quantum Hall Hamiltonian in spherical geometry [105] and produce lattice structures without lattice potentials [106][107]. By going down to lower dimensions, it is intriguing to see physics that needs only small SOC strength with minimal heating problems [108]. For another instance, SOC-induced coupling of center of mass motion with relative motion can also bring new interesting phenomena, like center of mass momentum dependent Feshbach resonances [109] or inhibition of two-body bound state formation [110]. Finally, combining spin-orbit coupled BECs with cavity [28-29] is another interesting topic. The high tunability of ultracold atomic systems is unique among all physical systems and it can lead to many new quantum phenomena with the new development in synthetic gauge fields.

APPENDICES

Appendix A: Derivation of atom-light interaction Hamiltonian

Consider a two-level atomic system with ground state $|g\rangle$ and excited state $|e\rangle$. By suitably defining the zero energy level, the energies of these two states can be chosen to be $-\hbar\omega_A/2$ and $\hbar\omega_A/2$. The energy difference between them is $\hbar\omega_A$. The unperturbed Hamiltonian is

$$H_0 = -\hbar\omega_A/2|g\rangle\langle g| + \hbar\omega_A/2|e\rangle\langle e|. \tag{A.1}$$

To the lowest approximation, we assume the atom behaves like a dipole moment when interacting with the electromagnetic field. Therefore, the interaction Hamiltonian under the dipole approximation is

$$H_1 = -\vec{d}\cdot\vec{E}, \tag{A.2}$$

where the classical electric field $\vec{E}(\vec{r},t) = \vec{E}_0\cos(\phi-\omega_L t) = \frac{1}{2}\vec{E}_0(e^{i\phi-i\omega_L t} + e^{-i\phi+i\omega_L t})$. If the laser field is traveling along x direction, then the phase angle $\phi = kx$. Writing the dipole moment in the basis set, $|g\rangle$ and $|e\rangle$, we get

$$\vec{d} = \vec{d}_{eg}(|e\rangle\langle g| + |g\rangle\langle e|), \tag{A.3}$$

where $\vec{d}_{eg} \equiv \langle e|\vec{d}|g\rangle$. Note that we don't have diagonal terms because the dipole moment in the eigenstate is zero due to parity symmetry. Therefore,

$$\begin{aligned}
H_1 &= -\vec{d}\cdot\vec{E} \\
&= -(\vec{d}_{eg}|e\rangle\langle g| + \vec{d}_{eg}|g\rangle\langle e|)\cdot\frac{\vec{E}_0}{2}(e^{i\phi-i\omega_L t} + e^{-i\phi+i\omega_L t}) \\
&= -\frac{1}{2}(\vec{d}_{eg}\cdot\vec{E}_0 e^{i\phi-i\omega_L t} + \vec{d}_{eg}\cdot\vec{E}_0 e^{-i\phi+i\omega_L t})|e\rangle\langle g| - c.c. \\
&= -\frac{1}{2}(\hbar\Omega_0 e^{i\phi-i\omega_L t} + \hbar\Omega_0 e^{-i\phi+i\omega_L t})|e\rangle\langle g| - c.c.
\end{aligned} \tag{A.4}$$

where $\hbar\Omega_0 \equiv \vec{d}_{eg} \cdot \vec{E}_0$ and *c.c.* stands for the complex conjugate term. Next, we rewrite the interaction Hamiltonian in the interacting picture. The unitary operator we need is

$$\begin{aligned}
\hat{O} &= \exp(iH_0t/\hbar) = 1 + iH_0t/\hbar + \frac{1}{2!}(\frac{iH_0t}{\hbar})^2 + \cdots \\
&= 1 + i(-\hbar\omega_A/2|g\rangle\langle g| + \hbar\omega_A/2|e\rangle\langle e|)t/\hbar - \frac{t^2}{2!\hbar^2}(-\hbar\omega_A/2|g\rangle\langle g| + \hbar\omega_A/2|e\rangle\langle e|)^2 + \cdots \\
&= \left[1 - i\omega_At/2 + \frac{(-i\omega_At)^2}{2!} + \cdots\right]|g\rangle\langle g| + \left[1 + i\omega_A/2 + \frac{(i\omega_At)^2}{2!} + \cdots\right]|e\rangle\langle e| \\
&= e^{-i\omega_At/2}|g\rangle\langle g| + e^{i\omega_At/2}|e\rangle\langle e|. \qquad (A.5)
\end{aligned}$$

After the unitary transformation, the interaction Hamiltonian becomes

$$\begin{aligned}
H_{1,\text{int}} &= e^{iH_0t/\hbar}Ue^{-iH_0t/\hbar} \\
&= -\frac{\hbar}{2}e^{-i\omega_At}(\Omega_0e^{i\phi-i\omega_Lt} + \Omega_0e^{-i\phi+i\omega_Lt})|g\rangle\langle e| - c.c. \\
&= -\frac{\hbar\Omega_0}{2}(e^{i\phi}e^{-i(\omega_L+\omega_A)t} + e^{-i\phi}e^{i(\omega_L-\omega_A)t})|g\rangle\langle e| - c.c. \\
&\approx -\frac{\hbar\Omega_0}{2}e^{-i\phi}e^{i(\omega_L-\omega_A)t}|g\rangle\langle e| - c.c. \qquad (A.6)
\end{aligned}$$

In the last line, we have neglected the fast oscillating terms with frequency $(\omega_L + \omega_A)$. This is the so-called the *rotating-wave approximation.* Now we transform the interaction Hamiltonian back to the Schrödinger picture.

$$H_1 = O^\dagger H_{1,\text{int}}O = -\frac{\hbar\Omega_0}{2}e^{-i\phi}e^{i\omega_Lt}|g\rangle\langle e| - \frac{\hbar\Omega_0}{2}e^{i\phi}e^{-i\omega_Lt}|e\rangle\langle g|. \qquad (A.7)$$

If we are in the reference frame rotating at the frequency ω_L, then the light field becomes time-independent and the atom-field interaction Hamiltonian can be written as

$$H_1 = -\frac{\hbar\Omega_0}{2}e^{-i\phi}|g\rangle\langle e| - \frac{\hbar\Omega_0}{2}e^{i\phi}|e\rangle\langle g|. \qquad (A.8)$$

In the matrix representation,

$$H_1 = \begin{pmatrix} 0 & -\frac{\hbar\Omega_0}{2}e^{-i\phi} \\ -\frac{\hbar\Omega_0}{2}e^{i\phi} & 0 \end{pmatrix}. \qquad (A.9)$$

Combining Eq. (A.1) and (A.9), we get the matrix U,

$$U = \begin{pmatrix} -\hbar(\omega_A - \omega_L)/2 & -\hbar\Omega_0/2e^{-i\phi} \\ -\hbar\Omega_0/2e^{i\phi} & \hbar(\omega_A - \omega_L)/2 \end{pmatrix}. \tag{A.10}$$

Note that the matrix H_0 won't be changed under the same unitary transformation U and the frequency ω_A is shifted by ω_L in the rotating frame.

$$U = \frac{\hbar}{2}\begin{pmatrix} -(\omega_A - \omega_L) & -\Omega_0 e^{-i\phi} \\ -\Omega_0 e^{i\phi} & (\omega_A - \omega_L) \end{pmatrix} = \frac{\hbar\Omega}{2}\begin{pmatrix} \cos\theta & \sin\theta e^{-i\phi} \\ \sin\theta e^{i\phi} & -\cos\theta \end{pmatrix}, \tag{A.11}$$

where $\tan\theta = \Omega_0/(\omega_A - \omega_L)$ and $\Omega = \sqrt{(\omega_A - \omega_L)^2 + \Omega_0^2}$. $\omega_A - \omega_L$ is the detuning of the laser frequency and the natural transition frequency in the atomic system.

Appendix B: Derivation of radial Green's matrix

The reduced radial Green's matrix satisfies the following coupled differential equation:

$$\left(-\frac{\hbar^2}{2\mu}\frac{d^2}{dr^2}\delta_{ij} + iA_{ij}\frac{d}{dr} + B_{ij} \right)\mathscr{G}_{jk}(r,r') = -\delta_{ik}\delta(r-r'), \tag{B.1}$$

where A is a real and symmetric matrix and B is a hermitian matrix without involving any derivative. The index $\{i,j,k\}$ run from 1 to n. Summation over j is implied. Although we study this particular type of coupled equations in Eq. (B.1), the procedures provided below is general and be applied to any type of coupled equations. The Green's matrix is used to emphasize the nature of *coupled* differential equations. If there is only one equation, the Green's matrix has only one component, so returns to the commonly termed Green's function.

The Green's matrix is constructed with the assistance of n regular and n irregular solutions of the homogenous equations,

$$\left(-\frac{\hbar^2}{2\mu}\frac{d^2}{dr^2}\delta_{ij} + iA_{ij}\frac{d}{dr} + B_{ij} \right) f_{j\alpha}(r) = 0 \tag{B.2}$$

$$\left(-\frac{\hbar^2}{2\mu}\frac{d^2}{dr^2}\delta_{ij} + iA_{ij}\frac{d}{dr} + B_{ij} \right) g_{j\alpha}(r) = 0. \tag{B.3}$$

Each column of $\underline{f}$ and $\underline{g}$ correspond to one independent regular/irregular solutions. For convenience, the notation $\underline{f}_\alpha$ and $\underline{g}_\alpha$ ($\alpha = 1, 2, ..., n$) for each independent regular and irregular solution will be used. The regular solution has to satisfy

$$\underline{f}_\alpha(r = 0) = \underline{0}. \tag{B.4}$$

The boundary condition for the irregular function is satisfied by requiring a $\pi/2$ phase lag to the regular solution at very large distance, $r \to \infty$.

Knowing that the regular and irregular solutions of the homogenous differential equation, we make the ansatz for the reduced Green's matrix:

$$\underline{\mathscr{G}}(r, r') = \begin{cases} \underline{f}(r)\underline{S}(r') & \text{for} \quad r < r', \\ \underline{g}(r)\underline{T}(r') & \text{for} \quad r > r'. \end{cases} \tag{B.5}$$

The next step is to match the expressions for the reduced Green's matrices at $r = r'$ and to apply the appropriate derivative discontinuity,

$$\underline{f}(r')\underline{S}(r') = \underline{g}(r')\underline{T}(r') \tag{B.6}$$

$$\lim_{\epsilon \to 0} \frac{d}{dr}\underline{\mathscr{G}}(r, r')|_{r'-\epsilon}^{r'+\epsilon} = \frac{2\mu}{\hbar^2}\underline{I}. \tag{B.7}$$

From Eq. (B.6), the matrix $\underline{S}(r')$ can be rewritten in terms of $\underline{T}(r')$ as

$$\underline{S}(r') = \underline{f}^{-1}(r')\underline{g}(r')\underline{T}(r'). \tag{B.8}$$

Application of Eq. (B.8) to Eq. (B.5) reduces Eq. (B.7) into an algebraic equation for the matrix $\underline{T}(r')$,

$$\left(\frac{d\underline{g}(r')}{dr'} - \frac{d\underline{f}(r')}{dr'}\underline{f}^{-1}(r')\underline{g}(r')\right)\underline{T}(r') = \frac{2\mu}{\hbar^2}\underline{I} \tag{B.9}$$

Therefore,

$$\underline{T}(r') = \frac{2\mu}{\hbar^2}[\underline{g}'(r') - \underline{f}'(r')\underline{f}^{-1}(r')\underline{g}(r')]^{-1}. \tag{B.10}$$

Combining Eq. (B.8) and (B.10), the matrices $\underline{S}$ and $\underline{T}$ are found to be

$$\underline{S} = \frac{2\mu}{\hbar^2} \times \underline{f}^{-1}(\underline{g}'\underline{g}^{-1} - \underline{f}'\underline{f}^{-1})^{-1} \tag{B.11}$$

$$\underline{T} = \frac{2\mu}{\hbar^2} \times \underline{g}^{-1}(\underline{g}'\underline{g}^{-1} - \underline{f}'\underline{f}^{-1})^{-1}. \tag{B.12}$$

It can be shown further that the Green's matrix in Eq. (B.5) with Eq. (B.11) and Eq. (B.12) indeed returns to the familiar form.

$$\underline{\mathscr{G}}(r,r') = \begin{cases} \pi \underline{f}(r)\underline{g}^\dagger(r') & \text{for} \quad r<r', \\ \pi \underline{g}(r)\underline{f}^\dagger(r') & \text{for} \quad r>r'. \end{cases} \tag{B.13}$$

Before we do that, we need first to prove that the analogues of the Wronskian for Eq. (B.1) are

$$\frac{\hbar^2}{2\mu}(\underline{g}'^\dagger \underline{f} - \underline{g}^\dagger \underline{f}') + i\underline{g}^\dagger \underline{A}\,\underline{f} = \underline{C} \tag{B.14}$$

$$\frac{\hbar^2}{2\mu}(\underline{f}'^\dagger \underline{f} - \underline{f}^\dagger \underline{f}') + i\underline{f}^\dagger \underline{A}\,\underline{f} = \underline{0} \tag{B.15}$$

$$\frac{\hbar^2}{2\mu}(\underline{g}'^\dagger \underline{g} - \underline{g}^\dagger \underline{g}') + i\underline{g}^\dagger \underline{A}\,\underline{g} = \underline{0}, \tag{B.16}$$

where $\underline{C}$ is a r-independent constant matrix and will be determined later by the requirement of energy normalization, and $\underline{0}$ is a zero matrix. The above set of Wronskians is shown below. Application of $\underline{g}_\beta^\dagger$ to Eq. (B.2) and $\underline{f}_\alpha^\dagger$ to Eq. (B.3) separately yields

$$-\underline{g}_\beta^\dagger \frac{\hbar^2}{2\mu}\underline{f}_\alpha'' + i\underline{g}_\beta^\dagger \underline{A}\,\underline{f}_\alpha' + \underline{g}_\beta^\dagger \underline{B}\,\underline{f}_\alpha = 0 \tag{B.17}$$

$$-\underline{f}_\alpha^\dagger \frac{\hbar^2}{2\mu}\underline{g}_\beta'' + i\underline{f}_\alpha^\dagger \underline{A}\,\underline{g}_\beta' + \underline{f}_\alpha^\dagger \underline{B}\,\underline{g}_\beta = 0, \tag{B.18}$$

Subtracting the complex conjugate of Eq. (B.18) from Eq. (B.17) gives the following equality,

$$\sum_j \frac{-\hbar^2}{2\mu}(g^*_{j\beta} f''_{j\alpha} - f_{j\alpha} g^{*\prime\prime}_{j\beta}) + i\sum_{j,k}(f'_{j\alpha} g^*_{k\beta} + f_{j\alpha} g^{*\prime}_{k\beta})A_{jk} = 0. \tag{B.19}$$

All the matrices are expressed in terms of their matrix elements. The properties of the matrices $\underline{A}$ and $\underline{B}$ are used to derive the above identity. After integration of both sides of Eq. (B.19) over r from a to b, one has

$$\sum_j \frac{\hbar^2}{2\mu}(f_{j\alpha} g^{*\prime}_{j\beta} - f'_{j\alpha} g^*_{j\beta})\Big|_a^b + i\sum_{j,k} f_{j\alpha} A_{jk} g^*_{k\beta}\Big|_a^b = 0. \tag{B.20}$$

The above formula is of course true for any range $[a, b]$, so we know that in matrix notation the following expression should be a constant, which is position-independent.

$$\frac{\hbar^2}{2\mu}(\underline{g}'^{\dagger}_{\beta}\underline{f}_{\alpha} - \underline{g}^{\dagger}_{\beta}\underline{f}'_{\alpha}) + i\underline{g}^{\dagger}_{\beta}\underline{A}\underline{f}_{\alpha} = c\delta_{\alpha\beta}. \tag{B.21}$$

Combining all the independent regular and irregular solutions, the "modified" Wronskian in Eq. (B.14) is derived. The other two Wronskians in Eq. (B.15) and Eq. (B.16) can be proved in a similar way. Noticing that the matrix $\underline{A}$ is proportional to the spin-orbit coupling strength, removal of the second term on the left hand side of Eq. (B.14)$\sim$(B.16) reduce to the familiar formula. The constant matrix $\underline{C}$ is determined by energy normalization. Application of energy normalization is important to guarantee unitarity of the scattering $\underline{S}$ matrix, which reflects flux conservation. The proper energy normalization gives $\underline{C} = \frac{1}{\pi}\underline{I}$.

The missing piece connecting Eq. (B.11) and Eq. (B.12) to Eq. (B.13) can be put together now. Taking the conjugate transpose of Eq. (B.14), we find

$$\frac{\hbar^2}{2\mu}(\underline{f}^{\dagger}\underline{g}' - \underline{f}'^{\dagger}\underline{g}) - i\underline{f}^{\dagger}\underline{A}\underline{g} = \frac{1}{\pi}\underline{I} \tag{B.22}$$

Applying $(\underline{f}^{\dagger})^{-1}$ to the left-hand side of Eq. (B.22) and $\underline{g}^{-1}$ to the right-hand side reduces the above equation into the following

$$\frac{\hbar^2}{2\mu}\underline{g}'\underline{g}^{-1} - (\frac{\hbar^2}{2\mu}\underline{f}'\underline{f}^{-1} - i\underline{A})^{\dagger} = \frac{1}{\pi}(\underline{f}^{\dagger})^{-1}\underline{g}^{-1}. \tag{B.23}$$

Also from Eq. (B.15) the relation can be derived,

$$\frac{\hbar^2}{2\mu}\underline{f}'\underline{f}^{-1} = (\frac{\hbar^2}{2\mu}\underline{f}'\underline{f}^{-1} - i\underline{A})^{\dagger}. \tag{B.24}$$

Therefore, Eq. (B.23) is further simplified to be

$$\underline{g}'\underline{g}^{-1} - \underline{f}'\underline{f}^{-1} = \frac{2\mu}{\hbar^2\pi}(\underline{f}^{\dagger})^{-1}\underline{g}^{-1}. \tag{B.25}$$

Plugging Eq. (B.25) into Eq. (B.12), it is straightforward to see that $\underline{T} = \pi f^{\dagger}$. Similarly, the matrix $\underline{S}$ is proved to be $\underline{S} = \pi\underline{g}^{\dagger}$.

BIBLIOGRAPHY

Bibliography

[1] M. H. Anderson, J. R. Ensher, M. R. Matthews, C. E. Wieman, and E. A. Cornell. Observation of bose-einstein condensation in a dilute atomic vapor. *Science*, 269(5221):198–201, 1995.

[2] M. R. Andrews, M.-O. Mewes, N. J. van Druten, D. S. Durfee, D. M. Kurn, and W. Ketterle. Direct, nondestructive observation of a bose condensate. *Science*, 273(5271):84–87, 1996.

[3] B. DeMarco and D. S. Jin. Onset of fermi degeneracy in a trapped atomic gas. *Science*, 285(5434):1703–1706, 1999.

[4] R. P. Feynman. Simulating Physics with Computers. *International Journal of Theoretical Physics*, 21:467–488, June 1982.

[5] Toshiya Kinoshita, Trevor Wenger, and David S. Weiss. Observation of a one-dimensional tonks-girardeau gas. *Science*, 305(5687):1125–1128, 2004.

[6] Z. Hadzibabic, P. Krüger, M. Cheneau, B. Battelier, and J. Dalibard. Berezinskii-Kosterlitz-Thouless crossover in a trapped atomic gas. *Nature*, 441:1118–1121, June 2006.

[7] Cheng Chin, Rudolf Grimm, Paul Julienne, and Eite Tiesinga. Feshbach resonances in ultracold gases. *Rev. Mod. Phys.*, 82:1225–1286, Apr 2010.

[8] Qijin Chen, Jelena Stajic, Shina Tan, and K. Levin. Bcsbec crossover: From high temperature superconductors to ultracold superfluids. *Physics Reports*, 412(1):1 – 88, 2005.

[9] X.L. Qi and S.C. Zhang. The quantum spin hall effect and topological insulators. *Physics Today*, 63(1):33, 2010.

[10] M. Hasan and C. Kane. *Colloquium* : Topological insulators. *Rev. Mod. Phys.*, 82:3045–3067, Nov 2010.

[11] N.R. Cooper. Rapidly rotating atomic gases. *Advances in Physics*, 57(6):539–616, 2008.

[12] K. W. Madison, F. Chevy, W. Wohlleben, and J. Dalibard. Vortex formation in a stirred bose-einstein condensate. *Phys. Rev. Lett.*, 84:806–809, Jan 2000.

[13] J. R. Abo-Shaeer, C. Raman, J. M. Vogels, and W. Ketterle. Observation of vortex lattices in bose-einstein condensates. *Science*, 292(5516):476–479, 2001.

[14] Jean Dalibard, Fabrice Gerbier, Gediminas Juzeliūnas, and Patrik Öhberg. *Colloquium* : Artificial gauge potentials for neutral atoms. *Rev. Mod. Phys.*, 83:1523–1543, Nov 2011.

[15] Zhi-Fang Xu, Li You, and Masahito Ueda. Atomic spin-orbit coupling synthesized with magnetic-field-gradient pulses. *Phys. Rev. A*, 87:063634, Jun 2013.

[16] Brandon M. Anderson, I. B. Spielman, and Gediminas Juzeliūnas. Magnetically generated spin-orbit coupling for ultracold atoms. *Phys. Rev. Lett.*, 111:125301, Sep 2013.

[17] J. Struck, C. Ölschläger, M. Weinberg, P. Hauke, J. Simonet, A. Eckardt, M. Lewenstein, K. Sengstock, and P. Windpassinger. Tunable gauge potential for neutral and spinless particles in driven optical lattices. *Phys. Rev. Lett.*, 108:225304, May 2012.

[18] K. Jiménez-García, L. J. LeBlanc, R. A. Williams, M. C. Beeler, A. R. Perry, and I. B. Spielman. Peierls substitution in an engineered lattice potential. *Phys. Rev. Lett.*, 108:225303, May 2012.

[19] J. Struck, J. Simonet, and K. Sengstock. Spin-orbit coupling in periodically driven optical lattices. *Phys. Rev. A*, 90:031601, Sep 2014.

[20] C. Hamner, Yongping Zhang, M. A. Khamehchi, Matthew J. Davis, and P. Engels. Spin-orbit-coupled bose-einstein condensates in a one-dimensional optical lattice. *Phys. Rev. Lett.*, 114:070401, Feb 2015.

[21] G. Juzeliūnas and P. Öhberg. Slow light in degenerate fermi gases. *Phys. Rev. Lett.*, 93:033602, Jul 2004.

[22] G. Juzeliūnas, J. Ruseckas, P. Öhberg, and M. Fleischhauer. Light-induced effective magnetic fields for ultracold atoms in planar geometries. *Phys. Rev. A*, 73:025602, Feb 2006.

[23] John R. Taylor. Scattering theory: The quantum theory of nonrelativistic collisions. 1972.

[24] H. A. Bethe. Theory of the effective range in nuclear scattering. *Phys. Rev.*, 76:38–50, Jul 1949.

[25] M. R. Andrews, C. G. Townsend, H.-J. Miesner, D. S. Durfee, D. M. Kurn, and W. Ketterle. Observation of interference between two bose condensates. *Science*, 275(5300):637–641, 1997.

[26] M.-O. Mewes, M. R. Andrews, N. J. van Druten, D. M. Kurn, D. S. Durfee, C. G. Townsend, and W. Ketterle. Collective excitations of a bose-einstein condensate in a magnetic trap. *Phys. Rev. Lett.*, 77:988–991, Aug 1996.

[27] Y.-J. Lin, K. Jiménez-García, and I. B. Spielman. Spin-orbit-coupled Bose-Einstein condensates. *Nature*, 471:83–86, mar 2011.

[28] Abraham J. Olson, Su-Ju Wang, Robert J. Niffenegger, Chuan-Hsun Li, Chris H. Greene, and Yong P. Chen. Tunable landau-zener transitions in a spin-orbit-coupled bose-einstein condensate. *Phys. Rev. A*, 90:013616, Jul 2014.

[29] B. Xiong, J.-h. Zheng, and D.-w. Wang. Nonadiabatic multichannel dynamics of a spin-orbit coupled condensate. *ArXiv e-prints*, October 2014.

[30] Y.-J. Lin, R. L. Compton, A. R. Perry, W. D. Phillips, J. V. Porto, and I. B. Spielman. Bose-einstein condensate in a uniform light-induced vector potential. *Phys. Rev. Lett.*, 102:130401, Mar 2009.

[31] Y.-J. Lin, R. L. Compton, K. Jiménez-García, J. V. Porto, and I. B. Spielman. Synthetic magnetic fields for ultracold neutral atoms. *Nature*, 462:628–632, December 2009.

[32] Y.-J. Lin, R. L. Compton, K. Jiménez-García, W. D. Phillips, J. V. Porto, and I. B. Spielman. A synthetic electric force acting on neutral atoms. *Nature Physics*, 7:531–534, July 2011.

[33] Pengjun Wang, Zeng-Qiang Yu, Zhengkun Fu, Jiao Miao, Lianghui Huang, Shijie Chai, Hui Zhai, and Jing Zhang. Spin-orbit coupled degenerate fermi gases. *Phys. Rev. Lett.*, 109:095301, Aug 2012.

[34] Lawrence W. Cheuk, Ariel T. Sommer, Zoran Hadzibabic, Tarik Yefsah, Waseem S. Bakr, and Martin W. Zwierlein. Spin-injection spectroscopy of a spin-orbit coupled fermi gas. *Phys. Rev. Lett.*, 109:095302, Aug 2012.

[35] Tin-Lun Ho and Shizhong Zhang. Bose-einstein condensates with spin-orbit interaction. *Phys. Rev. Lett.*, 107:150403, Oct 2011.

[36] Yun Li, Lev P. Pitaevskii, and Sandro Stringari. Quantum tricriticality and phase transitions in spin-orbit coupled bose-einstein condensates. *Phys. Rev. Lett.*, 108:225301, May 2012.

[37] W. Zheng, Z.-Q. Yu, X. Cui, and H. Zhai. Properties of Bose gases with the Raman-induced spin-orbit coupling. *Journal of Physics B Atomic Molecular Physics*, 46(13):134007, July 2013.

[38] S.-C. Ji, J.-Y. Zhang, L. Zhang, Z.-D. Du, W. Zheng, Y.-J. Deng, H. Zhai, S. Chen, and J.-W. Pan. Experimental determination of the finite-temperature phase diagram of a spin-orbit coupled Bose gas. *Nature Physics*, 10:314–320, April 2014.

[39] Jin-Yi Zhang, Si-Cong Ji, Zhu Chen, Long Zhang, Zhi-Dong Du, Bo Yan, Ge-Sheng Pan, Bo Zhao, You-Jin Deng, Hui Zhai, Shuai Chen, and Jian-Wei Pan. Collective dipole oscillations of a spin-orbit coupled bose-einstein condensate. *Phys. Rev. Lett.*, 109:115301, Sep 2012.

[40] Chunlei Qu, Chris Hamner, Ming Gong, Chuanwei Zhang, and Peter Engels. Observation of *Zitterbewegung* in a spin-orbit-coupled bose-einstein condensate. *Phys. Rev. A*, 88:021604, Aug 2013.

[41] L J LeBlanc, M C Beeler, K Jimnez-Garca, A R Perry, S Sugawa, R A Williams, and I B Spielman. Direct observation of zitterbewegung in a boseeinstein condensate. *New Journal of Physics*, 15(7):073011, 2013.

[42] Lev Landau. ”zur theorie der energieubertragung. ii”. *Physikalische Zeitschrift der Sowjetunion*, 2:46, 1932.

[43] Clarence Zener. Non-adiabatic crossing of energy levels. *Proceedings of the Royal Society of London A: Mathematical, Physical and Engineering Sciences*, 137(833):696, 1932.

[44] E. C. G. Stueckelberg. Theorie der unelastischen stsse zwischen atomen. *Helvetica Physica Acta*, 5:369, 1932.

[45] Ettore Majorana. Atomi orientati in campo magnetico variabile. *Il Nuovo Cimento*, 9(2):43, 1932.

[46] Yu. N. DEMKOV and V.I. OSHEROV. Stationary and nonstationary problems in quantum mechanics that can be solved by means of contour integration. *SOVIET PHYSICS JETP*, 26(5):916, 1968.

[47] Valentine N Ostrovsky and Hiroki Nakamura. Exact analytical solution of the n -level landau - zener-type bow-tie model. *Journal of Physics A: Mathematical and General*, 30(19):6939, 1997.

[48] Yu N Demkov and V N Ostrovsky. The exact solution of the multistate landau-zener type model: the generalized bow-tie model. *Journal of Physics B: Atomic, Molecular and Optical Physics*, 34(12):2419, 2001.

[49] Charles W. Clark. The calculation of non-adiabatic transition probabilities. *Physics Letters A*, 70(4):295 – 296, 1979.

[50] H. Tal-Ezer and R. Kosloff. An accurate and efficient scheme for propagating the time dependent schrodinger equation. *The Journal of Chemical Physics*, 81(9):3967–3971, 1984.

[51] Daniel T. Colbert and William H. Miller. A novel discrete variable representation for quantum mechanical reactive scattering via the smatrix kohn method. *The Journal of Chemical Physics*, 96(3):1982–1991, 1992.

[52] J. Higbie and D. M. Stamper-Kurn. Generating macroscopic-quantum-superposition states in momentum and internal-state space from bose-einstein condensates with repulsive interactions. *Phys. Rev. A*, 69:053605, May 2004.

[53] Xiaoling Cui. Mixed-partial-wave scattering with spin-orbit coupling and validity of pseudopotentials. *Phys. Rev. A*, 85:022705, Feb 2012.

[54] Jayantha P. Vyasanakere and Vijay B. Shenoy. Bound states of two spin-$\frac{1}{2}$ fermions in a synthetic non-abelian gauge field. *Phys. Rev. B*, 83:094515, Mar 2011.

[55] Long Zhang, Youjin Deng, and Peng Zhang. Scattering and effective interactions of ultracold atoms with spin-orbit coupling. *Phys. Rev. A*, 87:053626, May 2013.

[56] Hao Duan, Li You, and Bo Gao. Ultracold collisions in the presence of synthetic spin-orbit coupling. *Phys. Rev. A*, 87:052708, May 2013.

[57] Xiangang Wan, Ari Turner, Ashvin Vishwanath, and Sergey Savrasov. Topological semimetal and fermi-arc surface states in the electronic structure of pyrochlore iridates. *Phys. Rev. B*, 83:205101, May 2011.

[58] A. Burkov and Leon Balents. Weyl semimetal in a topological insulator multilayer. *Phys. Rev. Lett.*, 107:127205, Sep 2011.

[59] Congjun Wu, Jiang-Ping Hu, and Shou-Cheng Zhang. Exact so(5) symmetry in the spin-3/2 fermionic system. *Phys. Rev. Lett.*, 91:186402, Oct 2003.

[60] Xiaoling Cui and Wei Yi. Universal borromean binding in spin-orbit-coupled ultracold fermi gases. *Phys. Rev. X*, 4:031026, Aug 2014.

[61] Zhe-Yu Shi, Xiaoling Cui, and Hui Zhai. Universal trimers induced by spin-orbit coupling in ultracold fermi gases. *Phys. Rev. Lett.*, 112:013201, Jan 2014.

[62] Z.-Y. Shi, H. Zhai, and X. Cui. Efimov physics and universal trimer in spin-orbit coupled ultracold atomic mixtures. *ArXiv e-prints*, November 2014.

[63] Brandon M. Anderson, Gediminas Juzeliūnas, Victor M. Galitski, and I. B. Spielman. Synthetic 3d spin-orbit coupling. *Phys. Rev. Lett.*, 108:235301, Jun 2012.

[64] Su-Ju Wang and Chris H. Greene. General formalism for ultracold scattering with isotropic spin-orbit coupling. *Phys. Rev. A*, 91:022706, Feb 2015.

[65] D. A. Varshalovich, A. N. Moskalev, and V. K. Khersonskii. *Quantum Theory of Angular Momentum.* World Scientific, Singapore, 1988.

[66] Eugene P. Wigner. On the behavior of cross sections near thresholds. *Phys. Rev.*, 73:1002–1009, May 1948.

[67] C. H. L. Quay, T. L. Hughes, J. A. Sulpizio, L. N. Pfeiffer, K. W. Baldwin, K. W. West, D. Goldhaber-Gordon, and R. de Picciotto. Observation of a one-dimensional spin-orbit gap in a quantum wire. *Nature Physics*, 6:336–339, May 2010.

[68] Yi-Cai Zhang, Shu-Wei Song, and Wu-Ming Liu. The confinement induced resonance in spin-orbit coupled cold atoms with raman coupling. *Scientific Reports*, 4:4992, May 2014.

[69] M. Olshanii. Atomic scattering in the presence of an external confinement and a gas of impenetrable bosons. *Phys. Rev. Lett.*, 81:938–941, Aug 1998.

[70] T. Bergeman, M. G. Moore, and M. Olshanii. Atom-atom scattering under cylindrical harmonic confinement: Numerical and analytic studies of the confinement induced resonance. *Phys. Rev. Lett.*, 91:163201, Oct 2003.

[71] Toshiya Kinoshita, Trevor Wenger, and David S. Weiss. Observation of a one-dimensional tonks-girardeau gas. *Science*, 305(5687):1125–1128, 2004.

[72] G. E. Astrakharchik, J. Boronat, J. Casulleras, and S. Giorgini. Beyond the tonks-girardeau gas: Strongly correlated regime in quasi-one-dimensional bose gases. *Phys. Rev. Lett.*, 95:190407, Nov 2005.

[73] Elmar Haller, Mattias Gustavsson, Manfred J. Mark, Johann G. Danzl, Russell Hart, Guido Pupillo, and Hanns-Christoph Nägerl. Realization of an excited, strongly correlated quantum gas phase. *Science*, 325(5945):1224–1227, 2009.

[74] R. A. Williams, L. J. LeBlanc, K. Jiménez-García, M. C. Beeler, A. R. Perry, W. D. Phillips, and I. B. Spielman. Synthetic partial waves in ultracold atomic collisions. *Science*, 335(6066):314–317, 2012.

[75] Erich J. Mueller. Viewpoint: Spin-orbit coupling comes in from the cold. *Physics*, 5:96, 2012.

[76] Zhengkun Fu, Pengjun Wang, Shijie Chai, Lianghui Huang, and Jing Zhang. Bose-einstein condensate in a light-induced vector gauge potential using 1064-nm optical-dipole-trap lasers. *Phys. Rev. A*, 84:043609, Oct 2011.

[77] H. Zhai. Degenerate Quantum Gases with Spin-Orbit Coupling. *ArXiv e-prints*, March 2014.

[78] J. Reichel and J.H. Thywissen. Using magnetic chip traps to study tonks-girardeau quantum gases. *J. Phys. IV France*, 116:265–274, 2004.

[79] David A. Harmin. Theory of the nonhydrogenic stark effect. *Phys. Rev. Lett.*, 49:128–131, Jul 1982.

[80] David A. Harmin. Theory of the stark effect. *Phys. Rev. A*, 26:2656–2681, Nov 1982.

[81] David A. Harmin. Comment. *At. Mol. Phys.*, 15:281, 1985.

[82] U. Fano. Stark effect of nonhydrogenic rydberg spectra. *Phys. Rev. A*, 24:619–622, Jul 1981.

[83] NIST Digital Library of Mathematical Functions. http://dlmf.nist.gov/, Release 1.0.10 of 2015-08-07.

[84] Bo Gao. Analytic description of atomic interaction at ultracold temperatures: The case of a single channel. *Phys. Rev. A*, 80:012702, Jul 2009.

[85] B. Juliá-Díaz, T. Graß, O. Dutta, D. E. Chang, and M. Lewenstein. Engineering p-wave interactions in ultracold atoms using nanoplasmonic traps. *Nature Communications*, 4:2046, July 2013.

[86] R. B. Laughlin. Anomalous quantum hall effect: An incompressible quantum fluid with fractionally charged excitations. *Phys. Rev. Lett.*, 50:1395–1398, May 1983.

[87] N. Regnault and Th. Jolicoeur. Quantum hall fractions in ultracold fermionic vapors. *Phys. Rev. B*, 70:241307, Dec 2004.

[88] D. D. Osheroff, R. C. Richardson, and D. M. Lee. Evidence for a new phase of solid he^3. *Phys. Rev. Lett.*, 28:885–888, Apr 1972.

[89] A. J. Leggett. Interpretation of recent results on he^3 below 3 mk: A new liquid phase? *Phys. Rev. Lett.*, 29:1227–1230, Oct 1972.

[90] V. Efimov. Energy levels arising from resonant two-body forces in a three-body system. *Physics Letters B*, 33(8):563 – 564, 1970.

[91] Efimov V. *Sov. J. Nucl. Phys.*, 12:589, 1971.

[92] S. Jonsell. Efimov states for systems with negative scattering lengths. *EPL (Europhysics Letters)*, 76:8–14, October 2006.

[93] C.S. Adams and E. Riis. Laser cooling and trapping of neutral atoms. *Progress in Quantum Electronics*, 21(1):1 – 79, 1997.

[94] Eric Braaten and H.-W. Hammer. Universality in few-body systems with large scattering length. *Physics Reports*, 428(56):259 – 390, 2006.

[95] B. D. Esry, Chris H. Greene, and James P. Burke. Recombination of three atoms in the ultracold limit. *Phys. Rev. Lett.*, 83:1751–1754, Aug 1999.

[96] Aron Kuppermann. Reactive scattering with row-orthonormal hyperspherical coordinates. 1. transformation properties and hamiltonian for triatomic systems. *The Journal of Physical Chemistry*, 100(7):2621–2636, 1996.

[97] Aron Kuppermann. Reactive scattering with row-orthonormal hyperspherical coordinates. 2. transformation properties and hamiltonian for tetraatomic systems. *The Journal of Physical Chemistry A*, 101(36):6368–6383, 1997.

[98] Aron Kuppermann. Reactive scattering with row-orthonormal hyperspherical coordinates. 3. hamiltonian and transformation properties for pentaatomic systems. *The Journal of Physical Chemistry A*, 113(16):4518–4533, 2009.

[99] Zhe-Yu Shi, Xiaoling Cui, and Hui Zhai. Universal trimers induced by spin-orbit coupling in ultracold fermi gases. *Phys. Rev. Lett.*, 112:013201, Jan 2014.

[100] Xiaoling Cui and Wei Yi. Universal borromean binding in spin-orbit-coupled ultracold fermi gases. *Phys. Rev. X*, 4:031026, Aug 2014.

[101] Zhe-Yu Shi, Hui Zhai, and Xiaoling Cui. Efimov physics and universal trimers in spin-orbit-coupled ultracold atomic mixtures. *Phys. Rev. A*, 91:023618, Feb 2015.

[102] Congjun Wu. Viewpoint: Exotic many-body physics with large-spin fermi gases. *Physics*, 3:92, 2010.

[103] Lianyi He and Xu-Guang Huang. Bcs-bec crossover in 2d fermi gases with rashba spin-orbit coupling. *Phys. Rev. Lett.*, 108:145302, Apr 2012.

[104] Jayantha P. Vyasanakere, Shizhong Zhang, and Vijay B. Shenoy. Bcs-bec crossover induced by a synthetic non-abelian gauge field. *Phys. Rev. B*, 84:014512, Jul 2011.

[105] Vijay B Shenoy and Jayantha P Vyasanakere. Fermions in synthetic non-abelian gauge potentials: rashbon condensates to novel hamiltonians. *Journal of Physics B: Atomic, Molecular and Optical Physics*, 46(13):134009, 2013.

[106] Subhasis Sinha, Rejish Nath, and Luis Santos. Trapped two-dimensional condensates with synthetic spin-orbit coupling. *Phys. Rev. Lett.*, 107:270401, Dec 2011.

[107] Z. F. Xu, R. Lü, and L. You. Emergent patterns in a spin-orbit-coupled spin-2 bose-einstein condensate. *Phys. Rev. A*, 83:053602, May 2011.

[108] Xiaoling Cui and Tin-Lun Ho. Spin-orbit-coupled one-dimensional fermi gases with infinite repulsion. *Phys. Rev. A*, 89:013629, Jan 2014.

[109] Vijay B. Shenoy. Feshbach resonance in a synthetic non-abelian gauge field. *Phys. Rev. A*, 89:043618, Apr 2014.

[110] Jayantha P Vyasanakere and Vijay B Shenoy. Rashbons: properties and their significance. *New Journal of Physics*, 14(4):043041, 2012.

VITA

VITA

Before Su-Ju Wang joined Purdue University, she has finished her bachelor degree in the Department of Physics and Astronomy at National Tsing Hua University in Taiwan in 2007 and then her master degree in the field of biological physics at the same institution in 2009. She entered the department of Physics and Astronomy at Purdue University in the same year, and received a Doctorate of Philosophy in the field of theoretical Physics in 2016. After her Ph.D. degree, she will continue her work in theoretical atomic physics as a postdoctoral scholar in Department of physics and Astronomy at Washington state University.